ENERGY CONSUMPTION AND CHARGING DYNAMICS OF

FLOW-THROUGH CAPACITIVE DEIONIZATION SYSTEMS

A DISSERTATION

SUBMITTED TO THE DEPARTMENT OF MECHANICAL ENGINEERING

AND THE COMMITTEE ON GRADUATE STUDIES

OF STANFORD UNIVERSITY

IN PARTIAL FULFILLMENT OF THE REQUIREMENTS

FOR THE DEGREE OF

DOCTOR OF PHILOSOPHY

Yatian Qu

December 2016

This dissertation is online at: http://purl.stanford.edu/gc752yf8907

I certify that I have read this dissertation and that, in my opinion, it is fully adequate in scope and quality as a dissertation for the degree of Doctor of Philosophy.

Juan Santiago, Primary Adviser

I certify that I have read this dissertation and that, in my opinion, it is fully adequate in scope and quality as a dissertation for the degree of Doctor of Philosophy.

Xiaolin Zheng

I certify that I have read this dissertation and that, in my opinion, it is fully adequate in scope and quality as a dissertation for the degree of Doctor of Philosophy.

Michael Stadermann

Approved for the Stanford University Committee on Graduate Studies.

Patricia J. Gumport, Vice Provost for Graduate Education

This signature page was generated electronically upon submission of this dissertation in electronic format. An original signed hard copy of the signature page is on file in University Archives.

Abstract

Water scarcity is an emerging global issue. For the last few decades, fresh water shortage is becoming a threat to sustainable development of human society. Currently, four billion people, two-thirds of the world population, experience severe water scarcity during at least 1 month of the year. Desalination of seawater or brackish water can potentially help address this water shortage crisis, by increasing fresh water supplies. Particularly, the desalination of brackish water is more appealing and feasible to inland regions where seawater resources are not accessible.

Capacitive deionization (CDI) is a promising desalination technology, which operates at low pressure, ambient temperature, requires little infrastructure, and has the potential to consume less energy than the state-of-the-art technique reverse osmosis (RO) for brackish water desalination. Recently developed flow-through CDI (ftCDI) devices demonstrate effective salt removal with a desalination rate 4 to 10 times faster than traditional CDI cells. However, ftCDI faces operational challenges such as low water recovery and non-uniform effluent concentration. In addition, CDI devices consume significantly more energy than the theoretical thermodynamic minimum.

To tackle challenges of high energy consumption, we present our efforts to characterize electric resistances in a CDI system, with a focus on the resistance associated with the contact between current collectors and porous electrodes. We present an equivalent circuit model to describe resistive components in a CDI cell. We propose measurable figures of merit to characterize cell resistance. We also show that contact pressure between porous electrodes and current collectors can significantly reduce contact resistance. In addition, we propose and test an alternative electrical contact configuration which uses a pore-filling conductive adhesive (silver epoxy) and achieves significant reductions in contact resistance.

To further optimize energy consumption, we also present our studies to compare energy consumption of a CDI cell in constant voltage (CV) and constant current (CC) operations, with a focus on understanding the underlying physics of consumption patterns. The comparison is conducted under conditions that the CV and CC operations result in the same amounts of input charge and within identical charging phase durations. We present two electrical circuit models to simulate energy consumption in charging phase: one is a simple RC circuit model, and the other a transmission line circuit model. We built and tested a CDI cell to validate the transmission line model, and performed a series of experiments to compare CV versus CC operation under the condition of equal applied charge and charging duration. The experiments show that CC mode consumes energy at 33.8 kJ per mole of ions removed, which is only 28% of CV mode energy consumption (120.6 kJ/mole), but achieves similar level of salt removals. Together, the models and experiment support our major conclusion that CC is more energy efficient than CV for equal charge and charging duration. The models also suggest that the lower energy consumption of CC in charging is due to its lower resistive dissipation.

Finally, to address water recovery and non-uniform effluent concentration problems, we present a study of the interplay among electric charging rate, capacitance, salt removal, and fluid flow in ftCDI systems. We develop two models describing coupled transport and electro- adsorption/desorption which capture salt removal dynamics. The first model is a simplified, zero-dimensional lumped-parameter model which identifies dimensionless parameters and figures of merits associated with cell performance in advection-limited transport regime. The second model is a high-fidelity numerical model which captures spatial and temporal responses of charging for both advection-limited and dispersion-limited transport regimes. We further conducted an experimental study of these charging dynamics. We use these experimental data to validate models. The study shows that, in the advection-limited regime, differential charge efficiency determines the salt adsorption at the early stage of deionization process. Charging subsequently transitions to a quasi-steady state where salt removal rate is proportional to applied current scaled by the inlet flow rate. In the diffusion-dominated regime, differential efficiency, cell volume, and diffusion rates govern adsorption dynamics while flow rate has little effect. In both regimes, the interplay among mass transport rate, differential charge efficiency, cell capacitance, and (electric) charging current governs salt removal in ftCDI.

Acknowledgments

In 2009, when I first visited Stanford, I was stunned by the beautiful campus, magnificent buildings, legendary history and its world-wide reputation. Stanford was my dream school, a school that perhaps I could only imagine that I could attend in my dreams. My application to the department of Mechanical Engineering of Stanford was more like a moon shot which I could never expect it might land well. When I received the admission letter from Stanford with a fellowship, I felt I was one of the luckiest girls in the world. I was thrilled, nervous and excited for the years to come in my dream school.

The past six years that I spent on "The Farm" has been the most amazing and valuable experience in my entire life. I grew from a student who was just good at taking exams but had no critical thinking to a researcher that understands how to explore the unknowns in scientific ways, and how to calmly faces and handles uncertainties, hurdles and failures. This journey towards a doctoral degree at Stanford was not easy at all. I experienced a darkest period of time in my life when I struggled almost everyday for if I could have money for another quarter in school. I experienced doubts from others and most frequently from myself, and unstopped frustration from seeing no process in my research despite the continuous long hours of hard work. Many times during the past six years I wondered if I could ever reach the end, I doubted if I made the right decision to stay for a Ph.D., and I thought about quitting halfway. Looking back, I could not possibly get to this point without tremendous help, support and love from advisors, colleagues, friends and family members.

I would like to first thank my advisor, Prof. Juan G. Santiago. Juan accepted me to his group in April 2012. He took a bet on me when I had the toughest time in my life. I had a very unpleasant rotation experience in another research lab before I joined Juan's group. That rotation experience

led to self-doubt in almost every aspect of myself, but Juan trusted me. For the past few years, Juan influenced me in many different ways. His guidance, advice and support have greatly shaped me professionally and personally. His attitude towards work and enthusiasm towards scientific research taught me how to be a top-notch scientist and researcher. He deeply wants and generously supports any of his students to be successful. I benefit tremendously from the advisor-advisee relationship with him.

I am very lucky that I have another close advisor for my thesis research work. I would like to thank Dr. Michael Stadermann in Lawrence Livermore National Laboratory (LLNL) for supporting my research, career development and personal growth for the three and a half years I spent in LLNL. Michael is the most passionate person that I know of to capacitive deionization technology. He patiently taught me electrochemistry basics and guided me through my research. He is always willing to spend time to brainstorm with me for research ideas, work with me for setting up experiments and have long discussions with me on research problems. His strong faith and enthusiasm in capacitive deionization have brought large amounts of research funding and attracted a team of top scientists.

I would like to thank several professors who are not my academic advisors but helped me and had great influence on me during my graduate studies. I would like to thank Prof. CJ Kim in UCLA for opening the door of scientific research to me in my junior year in college. He also generously supported me for graduate school and fellowship applications. I would like to thank Prof. Beth Pruitt who nominated me for Ginzton research fellowship which enabled me to come to Stanford to pursue my dream. Also thank Prof. Thomas Kenny for taking me as a rotation student in his group during my first year and generously supported my fellowship applications. I would also like to thank my reading committee and oral examination committee: Prof. Xiaolin Zheng, Prof. Ali Mani and Prof. Juan Rivas for fruitful discussion and genuine feedback to my work.

There are several Santiago's group alumni who I would like to thank for setting the perfect role models for me in my early years of Ph.D. Dr. Anita Rogacs closely mentored me for a summer and taught me how to think critically and work independently for research projects. I learned resilience, persistence and proactiveness from her. She was the reason that I could join Juan's group and she strongly support me for many other career decisions. Besides being a role model, she is also a life-long mentor and friend to me. Dr. Lewis Marshall mentored me during my third year in Ph.D.,

Contents

List of Tables

List of Figures

Chapter 1

Introduction

1.1   Background and motivations

Water scarcity is an emerging global issue. For the last few decades, fresh water shortage is becoming a threat to sustainable development of human society. Increasing world population, improving living standards and expansion of irrigated agriculture drive the rising global demand for water. However, the accessible fresh water resources remain unchanged [1]. Currently, four billion people, two-thirds of the world population, experience severe water scarcity during at least 1 month of the year. Most of these populations live in developing countries, such as India (1.0 billion), China (0.9 billion), Bangladesh (130 million) and etc. In United States, 130 million people face severe water scarcity during at least part of the year, mostly in western states such as California and southern states such as Texas and Florida [1]. Water scarcity may cause hunger, health and sanitation issues, and it may also pose a threat to economic development. Therefore, meeting humanity's increasing demand for fresh water in a sustainable manner will be one of the most difficult and important challenges of this century [2].

Fresh water is severely limited resource on earth. Although the total volume of water on Earth is about 1.4×10^9 km^3, the volume of fresh water resources is only about 35×10^6 km^3, or 2.5% of the total volume. As shown schematically in Figure 1.1, about 24×10^6 km^3 or 68.9 % of these fresh water resources is in the form of ice and permanent snow in mountainous regions, or in the

<div align="center">1</div>

Antarctic and Arctic regions. The total accessible fresh water supply for ecosystems and human, including freshwater lakes, rivers and groundwater, is around 200,000 km^3. This fresh water supply is less than 1% of all fresh water resources, and only 0.01% of all the water on earth [3].

Total water volume: 1.4 billion km³

97.5% Sea water
2.5% Fresh water

68.9% Ice or snow

<1% surface freshwater
90, 000 km³
~30.1% ground water
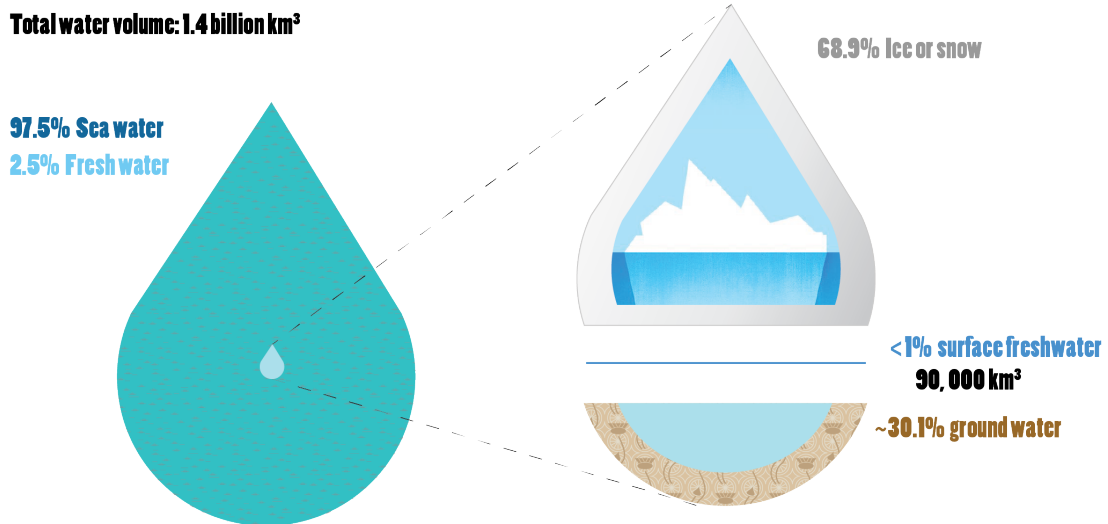
Figure 1.1: Schematic of global water resources distribution (The area of fresh water representation on the left is exaggerated and it is not reflecting the actual volume ratio of fresh water to seawater).

Fresh water is essential for ecosystems and all life forms, especially for human beings. Human cannot survive without water. The basic water requirements for human activities vary by water usages and living conditions. Based on the estimates with individuals who engage in moderate physical activity in above-average temperatures, a minimum of 7.5 liters per capita per day will meet the basic living requirements under most conditions [4]. In an emergency situation, a minimum of 15 liters is required [4]. A higher quantity of about 20 liters per capita per day should be assured to take care of basic hygiene needs and basic food hygiene. Considering water uses from different sectors of society, such as drinking, removing or diluting wastes, producing manufactured goods, growing food, producing and using energy and so on, the recommended basic consumption requirement is 50 liters per person per day [5]. This number may seem small comparing to about 400 liters United States domestic water consumption per capita per day [6]. However, vast regions of the world lack

the water resources required to meet this basic human needs standard [5].

In addition to basic human water requirements, there are several other matrices or indicators to evaluate water scarcity situations. The Falkenmark indicator is perhaps the most widely used measure of water stress. It is defined as the total annual water resources available to the population of a region. It measures scarcity as the amount of renewable freshwater that is available for each person each year. The index thresholds 1,700 m^3 and 1000 m^3 per capita per year are used as the thresholds between water stressed and scarce areas, respectively [7]. This index is typically used in assessments on a country scale where the data is readily available and provides results that are intuitive and easy to understand. However, the use of national annual averages tends to obscure important scarcity information at smaller scales. Another popular indicator is Water Scarcity Indicator (WS). WS is defined as the volume of fresh surface water and groundwater that is withdrawn and not returned divided by the total fresh water available in a region. WS classified as low if the water footprint does not exceed water availability (WS < 1.0). Water scarcity is said to be moderate if it is in the range 1.0 < WS < 1.5, significant if it is in the range 1.5 < WS < 2.0, and severe if WS > 2.0 [1]. Using this standard, Mekonnen et al. found that 4.3 billion people living in areas with WS >1 at least 1 month in a year [1]. No matter which measure is used, a significant portion of global population is estimated to be living in water scarcity situations. Moreover, the problem of water scarcity is expected to grow significantly in the coming decades, and environmental issues such as climate change may further exacerbate the situation [8].

Desalination of seawater or brackish water can potentially help address water shortage crisis, by increasing fresh water supplies. Particularly, the desalination of brackish water is more appealing and feasible to inland regions where seawater is not accessible. Brackish water is surface water or groundwater that contains dissolved solids in the concentration range between 1 and 10 grams per liter (g/L) [9]. Brackish water has a greater dissolved-solids content than that occurs in fresh water (less than 1 g/L), but not as much as in seawater. Brackish water is not directly consumable, but it is potentially abundant water resource as mineralized groundwater and slightly and moderate surface water is largely available in many countries and areas. For example, in United States, mineralized groundwater underlies most of the country [9]. More than 95% of desalination facilities (1.5×10^6 m^3 per day in 2010) in the United States are inland [10], and most facilities are designed to treat

groundwater with dissolved-solids concentration in the brackish range [11].

The global desalination capacity is growing rapidly in the past decade. The global capacity was around 66.4×10^6 m^3 per day in 2010 [12]. In 2015, there are more than 18,000 desalination plants worldwide and produce more than 86.8×10^6 m^3 per day [13]. About 150 countries practice desalination to provide fresh water [13]. More than 300 million of people around the world rely on desalinated water for at least part of or all their daily needs [13]. The growth rate for global desalination capacity is currently about 55% per year, a truly stunning figure [12]. The expanding development and practice of water desalination is promising for helping address global water shortage crisis. Among the potential water resources enabled by desalination, the desalination of brackish water is especially attractive for semi-arid regions and inland areas where the groundwater and surface water serve as reliable water resources.

1.2 State-of-the-art brackish water desalination techniques

Brackish groundwater is directly used for purposes such as cooling water for power generation, aquaculture, and for a variety of uses in the oil and gas industry such as drilling, enhancing recovery, and hydraulic fracturing [9]. For purposes requiring lower dissolved-solids content, especially drinking water, brackish water is treated through desalination process.

Desalination is a water treatment process that removes salts or other dissolved minerals and contaminants such as dissolved metals, radionuclides, bacterial and organic matter from high salinity water to produce fresh water [14]. As goes through the desalination process, feed water (hard water, brackish water or seawater) is separated into two products: low-salinity water (fresh water) and very saline concentrate (brine water).

The most widely used technologies for brackish water desalination are membrane process (reverse osmosis) or thermal process (multi-stage flash distillation, multi-effect evaporation and etc.). In addition to these two traditional processes, emerging new and novel technologies include electrodialysis, forward osmosis and capacitive deionization.

1.2.1   Reverse osmosis

Reverse osmosis (RO) is a membrane separation process that recovers water from a saline solution. Osmosis refers to the net movement of water from lower concentration to higher concentration across a partially permeable membrane. If excess pressure is applied on the higher concentration, we could reverse the process. This process is known as reverse osmosis (RO). As shown in Figure 1.2a, feed water is pumped into a closed vessel where it is pressurized against the membrane. The water molecules pass through the membrane, increase the concentration of the reject water and produce purified water on the other side. The major components of an RO system include pretreatment units, membrane modules, high-pressure pumps, power plant, and energy-recovery devices as needed. The semi-permeable membrane is the most important component in RO. RO membranes are sensitive to pH, oxidizers, a wide range of organics, algae, bacteria and other foulants [15]. Therefore, pretreatment of the feed water is an essential step in RO process.

RO is a fairly mature technology and it is the benchmark for comparison for any new desalination technology [16]. Globally, about 60% of total desalination capacity is installed with RO (as of the first quarter of 2012) [12]. Since the osmotic pressure, and hence the pressure required to perform the separation is directly related to the salt concentration, RO is often the method of choice for brackish water, where only low to intermediate pressures are required. The operating pressure for brackish water systems ranges from 15 to 25 bar [17] and for seawater systems from 54 to 80 bar [18]. Since the pressure required to recover additional water increases as the brine stream is concentrated, the water recovery rate of RO systems tends to be low. A typical recovery value for a seawater RO system is about 50% [16]. In recent years, low-pressure reverse-osmosis (RO) membrane desalination has been explored as a viable technology for desalination of brackish water for potable usage [19].

Currently, RO is the most energy-efficient technology for seawater desalination [16]. The energy consumption for seawater RO (SWRO) treatment is 3-4 kWh/m^3 [12, 15, 20]. Potentially, this number can reduce to 1.8 kWh/m^3 for SWRO with 50% recovery using new, high-permeability membranes [16]. The energy consumption for brackish water RO (BWRO) is lower, within 0.5 - 2.5 kWh/m^3 [12, 15]. Since most of energy losses for RO result from releasing the pressure of the concentrated brine, large scale RO systems are now equipped with devices to recover the mechanical compression energy from the discharged brine stream with efficiencies up to 98%.

1.2.2 Thermal process technologies

Thermal desalination process includes multi-stage flash distillation (MSF), multi-effect distillation (MED) and vapor compression (VC). MSF (shown in Figure 1.2) has been widely used for sea water desalination, constituting about 26% of the global desalination capacity [12]. However, thermal process usually consumes much higher energy than RO. For example, MSF reports an energy consumption within 10 - 16 kWh/m^3. MED is more energy efficient compared to MSF, but it still requires energy consumption of 5.5 - 9 kWh/m^3. These reported energy costs are orders of magnitude higher than BWRO. Therefore, the thermal process is usually unfavored for brackish water desalination. Only in energy abundant areas such as geothermal-rich areas, thermal process could be a viable method for brackish water desalination.

1.2.3 Electrodialysis, Forward osmosis and etc.

Electrodialysis (ED) is another widely used technology for brackish water desalination [15]. Currently, approximately 3.5% of worldwide installed desalination capacity is ED, and almost all of facilities are used for brackish water desalination [12].

An ED system consists of large number of cells alternately contained within anion-exchange and cation-exchange membranes and arranged between a positive and a negative electrode. The cation membranes allow only positively charged ions migrate through, and the anion membranes only pass the negative ions. Therefore, upon the application of a direct current source, ions migrate through selective membranes to achieve the separation of water and dissolved salts. The water cells between the membranes are alternately depleted and enriched with salt ions.

ED is generally limited to slightly or moderate saline brackish waters. Similar to semi-permeable membranes in RO, the selective membrane used in ED are subject to fouling, and thus some pre-treatment of the feed water is also needed. However, since there is no direct water flowing through the ion exchange membranes, ED can treat water with a higher level of suspended solids than RO. In ED process, the precipitation of some salt ions (such as Ca^{2+} and Mg^{2+}) can be facilitated by changes on pH that occur near the membranes as a result of the transport of H^+ and OH$^-$ ions. The energy consumption of ED is reported as around 2 kWh/m^3 [21].
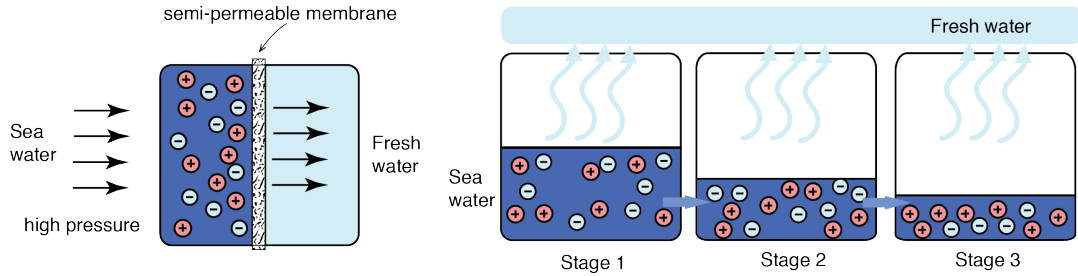
Figure 1.2: Schematic of the reverse osmosis (RO) process and multi-stage flash distillation process

1.3 Capacitive deionization cell architectures

1.3.1 Introduction of capacitive deionization (CDI)

Capacitive deionization (CDI) is an alternative desalination technique that uses charged, porous electrodes to electrostatically remove ions from the feed water. CDI is especially promising for brackish water desalination. Its main advantages are its wide scalability (investment cost is low and approximately directly proportional to capacity); great potential to offer drastically reduced cost of infrastructure (and operational plant costs); and potential to decrease the energy cost per volume of treated water [22, 23].

The key component of a CDI cell is a pair of porous carbon electrodes, as shown in Figure 1.3. Salt ions are removed from water and held electrostatically at pore surfaces. CDI cells operate in charge and discharge cycles. Upon application of a charging voltage or current, salt ions are transported and trapped within electrical double layers (EDLs) inside pores through electroadsorption. The cell is then regenerated by discharging at zero voltage (or reversed bias) or at a constant current to release adsorbed ions. A CDI operational unit can consist of a pump, a pre-treatment filter, cell stack (a number of cell pairs), valve for controlling flow and diverting potable and non-potable streams, and energy recovery elements.
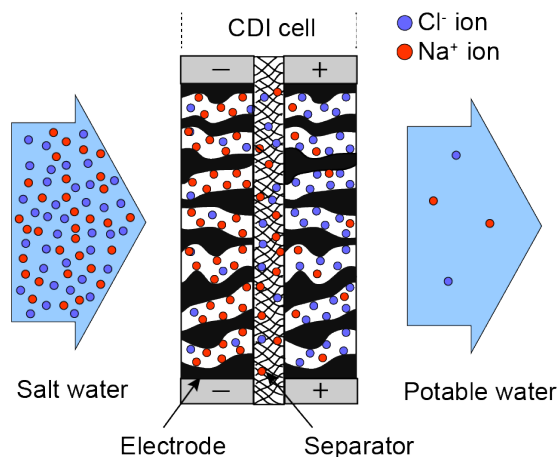
Figure 1.3: Schematic of the structure and operation of a capacitive deionization (CDI) cell. The cell consists of a pair of porous carbon electrodes which are separated by a dielectric porous membrane to prevent electrical contact. Salt water is fed through the cell by pumping. Upon application of a low voltage ($<$1.2 V) across the electrode pair, ions are electrostatically held to the surfaces of the porous carbon and form electric double layers (EDLs). The generated desalted stream is then pumped out.

In addition to aforementioned brackish water desalination, CDI also has the great potential for removing ionic impurities from water. CDI extracts ions of all types from feed water, including sodium, calcium, magnesium, chloride and toxic ions such as arsenate and fluoride. Several studies have suggested that CDI is selective (relative to sodium chloride) toward many other impurities due to the greater magnitude of their charge [24–26].

CDI is readily integratable with other water purification systems such as electrochlorination. It is also compatible with various renewable energy sources such as small grid and photovoltaic panels. The electrical supply requirements of CDI are extremely loose. Supply from grid sources would consist of a simple AC/DC converter (i.e. small transformer and rectifier bridge). Alternatively, the system can be powered directly from solar panels or battery sources. Its low cost, simplicity, robustness, and compatibility with renewable energy sources enable CDI a wide range of potential applications, such as portable fresh water devices, mobile desalination stations for disaster response, and municipal desalination plants. Particularly, CDI is ideally suited for small scale, distributed, off-grid applications, like water purification and energy storage in rural areas.

1.3.2 Recent development of CDI cell architectures

Cell architecture is important for CDI cell design and operation. The relatively traditional "flow-between" cell structure are widely used in CDI studies. In recent years, several novel cell architectures have been developed to introduce unique features.

The "flow-between" architecture is perhaps the most commonly used architecture in CDI. As shown in Figure 1.4 (a), in this architecture, the porous electrode pair is separated by a gap or spacer and the salt solution flows through the space in between. The flow-between structure has been applied in CDI since 1960 [22]. This structure is easy to assemble and to seal, and it can accommodate with a wide variety of electrode materials. Therefore, flow-between architecture has been used in a broad range of research work and commercialization efforts. One disadvantage of this architecture is that the gap between electrodes hinders the transport of ions from spacer channel to porous electrodes. As a result, the cell is unable to utilize the full adsorption capability of porous electrodes. In addition, the desalination rate is significantly limited by the spacer-to-electrode diffusion times, thus the cell desalinates inefficiently in longer time scales.

"Flow-through" is an alternative CDI architecture. As shown in Figure 1.4 (b), "flow-through" are configured to drive feed water directly through the electrodes and minimize the gap between them. This structure was deployed as early as in the 1970's by Johnson et al. However, because of the poor performance caused by high hydraulic resistance, this structure was abandoned for almost 40 years [22]. Recently, with new advancement in carbon material development, Suss et. al developed a "flow-through" CDI cell made of hierarchical carbon aerogel monoliths (HCAMs) and achieve 4-10 times faster charging times than "flow-between" cells and up to 70 mM reduction in salt concentration. This structure utilizes the full desalination capacity of electrodes. In addition, this architecture eliminates the need for a separator layer, thus allowing for more compact cells with lower cell ionic resistance, and therefore achieving faster desalination by reducing the diffusion timescale governing salt removal from between the electrodes. However, flow-through structure requires the use of hierarchical pore structure electrodes to enable flow through the electrodes at minimal hydraulic pressures. Moreover, assembly and sealing are two significant challenges for flow-through cell fabrication.
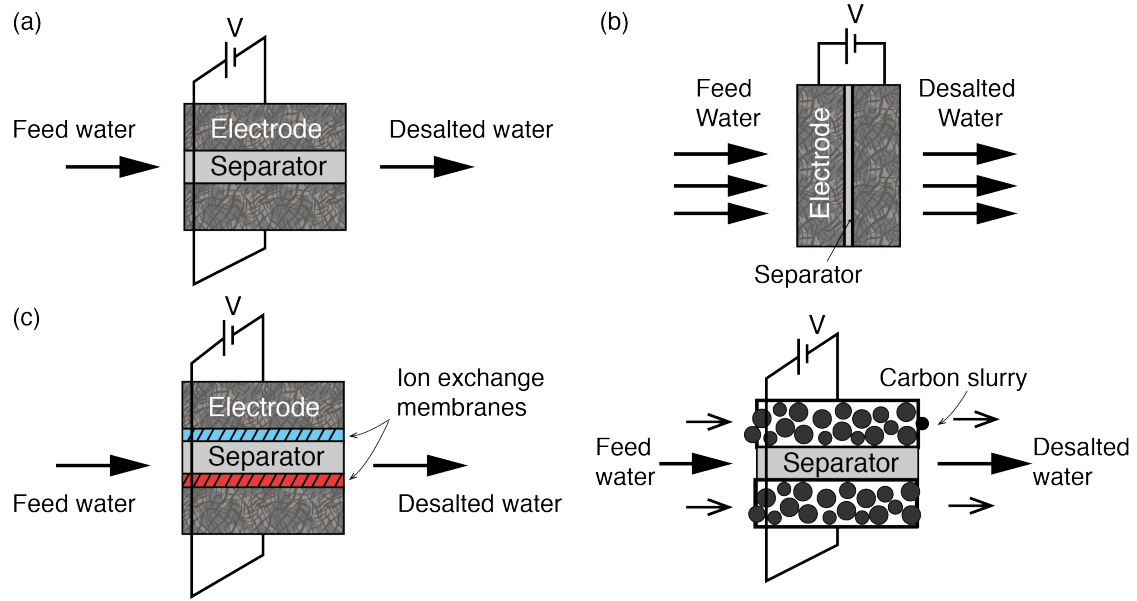
Figure 1.4: Schematic of major CDI cell architectures: (1) flow-between electrodes, (2) flow-through electrodes, (3) membrane CDI, (4) flow electrodes CDI.

Membrane CDI (MCDI) is major variation of "flow-between" CDI architecture. In MCDI, ion exchange membranes are placed between porous electrodes, as shown in Figure 1.4 (c). The main functionality of ion exchange membrane is to constrain co-ion migration into the adjoining porous electrode, thus improving charge efficiency. The most common implementation is to place a free-standing anion exchange membrane at the positive electrode and a free-standing cation exchange membrane at negative electrode. Ion exchange resins can also be coated onto the electrode surface to directly form a thin membrane. The ion exchange membranes can be modified to selectively pass certain types of ions, therefore providing an additional level of tunability for complex multi-species systems [27].

1.4 CDI cell operations

CDI cells can be operated in several different schemes in terms of charging methods. Perhaps the most commonly applied CDI operations are constant voltage and constant current. Recently, several novel operation schemes have been reported, such as inverted CDI (i-CDI). This new operation

enhances the salt removal capability of CDI cells by performing surface treatment of anode and working with potentials of zero charge of cathode and anode.

1.4.1   Constant current and constant voltage

In constant voltage (CV) operation, a constant voltage is applied between cathode and anode during charging, as shown in Figure 1.5 (a). To discharge, anode and cathode are electrically grounded or applied reverse bias to release ions. An alternative operation scheme is charging with a constant current (CC) and discharging with reverse currents, as shown in Figure 1.5 (b).
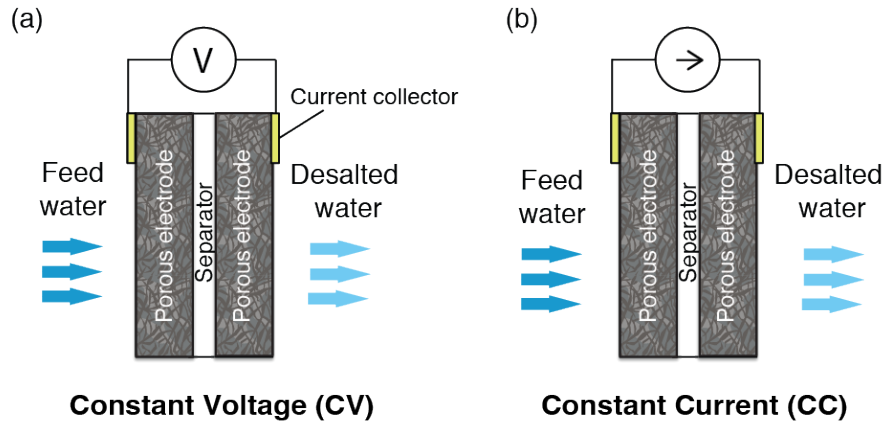
Figure 1.5: Schematic of (a) constant voltage and (b) constant current charging/discharging schemes with a CDI cell.

CV and CC operations demonstrate distinct electrical responses. As shown in Figure 1.6(a), in CC mode, voltage response has a voltage jump at the beginning of charging. This voltage jump is due to Ohmic resistance of the cell. The cell voltage then increases almost linearly versus time as charging to capacitive components. In CV mode, cell current shows a strong spike in the beginning and then decay with RC time constant, as shown in Figure 1.6(b). The effluent concentration profiles of CC and CV modes also demonstrate distinct features. Figure 1.7 shows the typical effluent concentration profiles of CV and CC operations. In CV mode, a rapid reduction of concentration occurs in the beginning due to the current spike in electrical response. The effluent concentration then gradually increases to feed concentration level. In CC operation, effluent concentration gradually decreases and levels off to a quasi-steady state concentration.
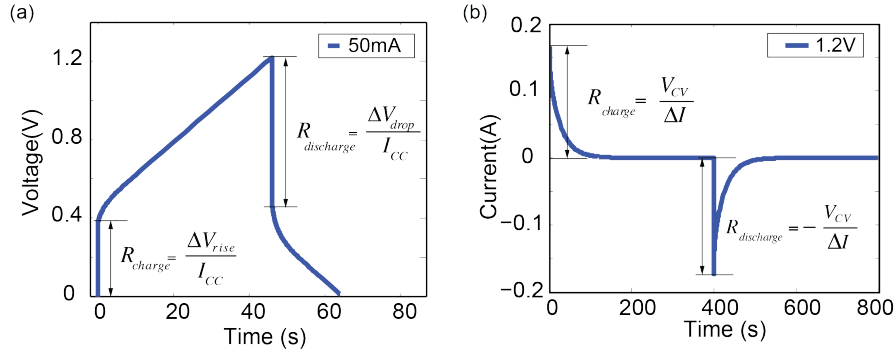
Figure 1.6: Electrical responses of CC and CV operations. (a) Typical current responses of CC mode; (b) Typical constant voltage responses of CV mode.

We have reviewed nearly 50 CDI publications which have experimental setup and were published since 2012. We estimated about 70% of those CDI studies were operated with CV mode and 30% were with operated with CC. As we later discussed with details in Chapter 3, CV operation has advantage of easier circuits implementation but has higher energy cost. In contrast, CC operation consumes lower energy and produces controllable effluent concentration streams but requires more work to implement circuitry.
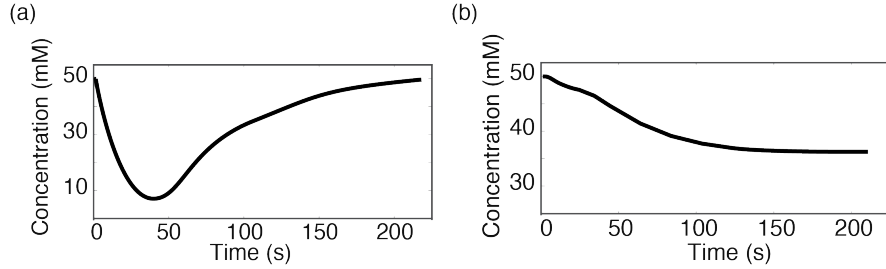
Figure 1.7: Typical effluent concentration profiles of (a) CV mode; (b) CC mode.

1.4.2   Inverted CDI

Inverted CDI (i-CDI) is a novel operation scheme which requires surface modification of electrodes. Gao et al. first reported an i-CDI cell [28]. They introduced negative surface groups to a carbon xeroggel anode by surface oxidation, and then built a CDI cell using the modified anode together with a pristine carbon xerogel as the cathode. Their CDI cell demonstrates inverted behavior, whereby cell charging resulted in desorption of ions and cell discharging resulted in ion electrosorption. One

advantage of i-CDI cell is its long-term stability. An i-CDI cell can undergo several hundreds of charging/discharging cycles without significant decay of salt adsorption performance. In contrast, a traditional CDI cell made with solely pristine carbon electrodes demonstrates relatively fast performance degradation, and this degradation is due to surface oxidation of anode [28].

1.5 CDI cell performance matrices

There are several widely used figure of merits to evaluate the performance of a CDI cell. As the schematics shown in Figure 1.8, commonly used figures of merits include salt removal capacity and rate, water recovery, water throughput and energy consumption.

The first important figure of merit is salt removal capacity and salt removal rate. Salt removal capacity is usually reported in terms of maximum total salt adsorption, which is also known as equilibrium salt adsorption capacity. This number is reported by dividing the mass of salt removed from the feed water by a representative electrode mass, resulting in a unit of mg/g. A representative electrode mass is usually the dry weight of both electrodes including all components such as active carbon, binder and etc. [22]. Average salt adsorption rate (ASAR) is another commonly used figure of merit associated with salt adsorption. ASAR has been reported in units of mg/g/min [29, 30], which evaluates the weight of salt removed per weight of electrode per unit of time. ASAR gives information on the rate of salt adsorption in a CDI cycle.

The second commonly used merit in desalination techniques is water recovery, as shown in Figure 1.8(b). Water recovery evaluates the volume ratio of fresh water produced from feed water. RO plants report typical water recovery around 50%. For desalination, we would like to maximize water recovery as to maximize fresh water production and minimize brine generation. This is not only because we want to extract fresh water as much as possible, but also because brine disposal is a significant challenge for all desalination techniques, especially for inland desalination needs.

Water throughput is another important merit for desalination technology. Water throughput is defined as the volume of fresh water produced per day per unit of device. Water throughput directly determines the desalination capacity of a plant. A typical RO plant can produce fresh water more than 100,000 m^3/day. As a comparison, CDI plants are scalable and more suitable for distributed applications. A CDI plant for municipal waste water reuse can have a capacity ranges from 5000

m^3/day to 60,000 m^3/day [22]

Finally, perhaps the most important figure of merit for CDI application is energy consumption. Traditional desalination techniques reports energy consumption in a unit of kWh/m^3. RO reports energy consumption of 3-4 kWh/m^3 for sea water desalination and 0.5 - 2.5 kWh/m^3 for brackish water desalination [12]. Thermal process, such as multi-stage flash distillation, is more energy intensive and consumes 10-16 kWh/m^3 for seawater desalination [12]. Energy consumption numbers (in units of kWh/m^3) are not largely available for CDI devices since most studies focus on early-stage research of the systems and the water production is not optimized. Instead, several CDI research studies report energy consumption in terms of salt removal, commonly in a unit of kT/ion [22, 31]. Several commercially deployed CDI plants report energy consumption less than 1.5 kWh/m^3 for waste water treatment [22].
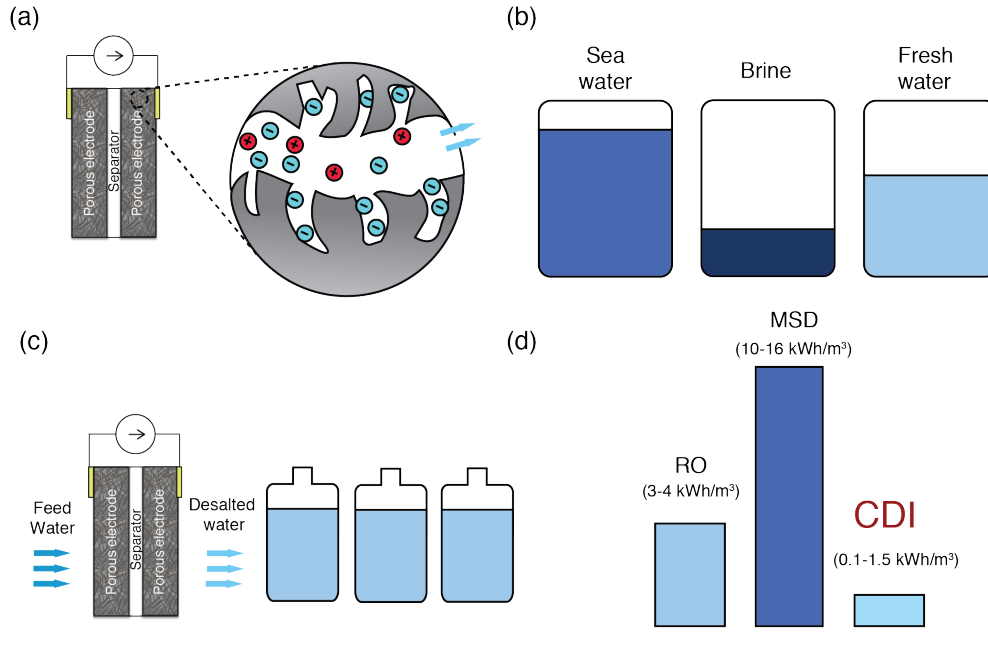
Figure 1.8: CDI performance figures of merits (a) salt removal capacity and salt removal rate; (b) water recovery; (c) water throughput; (d) energy consumption.

1.6 CDI commercialization

There have been several efforts on commercialization of CDI techniques since 1990s [22]. Lawrence Livermore National Laboratory in US spun off a CDI company named CDT in the 1990s [32]. However, the company ceased to exist after almost a decade of operation. Since then, CDI technologies have made significant improvements on material fabrication, cell design and system optimization. Several recent CDI commercialization efforts include membrane CDI units produced by Voltea B.V.(The Netherlands) and large-scale CDI pilot plants produced by EST Water & Technologies (People's republic of China). These commercial CDI systems focus on desalinating water in the low salinity range around 2000 ppm and have reported low energy consumption between 0.1 and 0.2 kWh/m^3 [22]. As an application example, up to now more than 30 industrial systems are installed in China, and most of the facilities are used for industrial/municipal waste water reuse and recycle and produces water 2,000 to 60,000 m^3/day [22].

We here summarize a list of CDI companies which we believe are active as of the time of this writing.

- Voltea, The Netherlands. http://www.voltea.com/

- Enpar Technologies, Ontario Canada. http://www.enpar-tech.com/

- Aqua EWP, LLC, San Antonio, TX. http://aquaewp.com/

- Atlantis Technologies, Beach, CA. http://www.atlantisllc.com/products.htm

- Aquas, Cupertino, CA.

- Puritech, Belgium. http://puritech.be/

1.7 Scope of dissertation

In Chapter 2: we present our efforts to characterize electric resistances in a CDI system, with a focus on the resistance associated with the contact between current collectors and porous electrodes. We present an equivalent circuit model to describe resistive components in a CDI cell. We propose measurable figures of merit to characterize cell resistance. We also show that contact pressure

between porous electrodes and current collectors can significantly reduce contact resistance. Lastly, we propose and test an alternative electrical contact configuration which uses a pore-filling conductive adhesive (silver epoxy) and achieves significant reductions in contact resistance.

In Chapter 3: we present our studies to compare energy consumption of a CDI cell in constant voltage (CV) and constant current (CC) operations, with a focus on understanding the underlying physics of consumption patterns. The comparison is conducted under conditions that the CV and CC operations result in the same amounts of input charge and within identical charging phase durations. We present two electrical circuit models to simulate energy consumption in charging phase: one is a simple RC circuit model, and the other a transmission line circuit model. We built and tested a CDI cell to validate the transmission line model, and performed a series of experiments to compare CV versus CC operation under the condition of equal applied charge and charging duration. We demonstrate that CC is more energy efficient than CV for equal charge and charging duration. The models also suggest that the lower energy consumption of CC in charging is due to its lower resistive dissipation.

In Chapter 4: we present our studies on understanding and characterizing the figures of merits associated in the interplay among charging time scales, fluid flow, and cell capacity, particularly in ftCDI. We present two models to describe the desalination performance of an ftCDI system with a focus on understanding and characterizing the coupling effects of charging and fluid flow for a given cell capacity. We first present a simple model which captures essential dynamics: a zero-dimensional, unsteady lumped parameter model. We then present a numerical model based on area-averaged one-dimensional unsteady transport equations. We validate modeling results by performing experiments with an ftCDI cell fabricated in house. We use both models to identify two important salt transport regimes, and pose non-dimensional parameters applicable to describe and quantify these regimes. We also briefly discuss differences between flow-through CDI, flow-between CDI and membrane CDI in terms of charging and flow interplay.

In Chapter 5: we present our attempt to develop a multi-stage ftCDI system with novel phased-charging operation scheme. We extend the numerical model described in Chapter 4 to a multi-stage configuration and demonstrate preliminary simulation results. We present development and fabrication iterations of two-stage and three-stage ftCDI cells. We demonstrate a novel operation

scheme for multi-stage CDI systems, where we subsequently charge and discharge each electrode pair in a phased manner. We compare preliminary experimental data to simulation results and discuss current challenges associated with phased charging operation. We also propose future studies to optimize the performance of multi-stage CDI systems.

Finally, in Chapter 6 we recap the important contributions of our work, and discuss potential future research directions.

Chapter 2

Characterization of internal resistance of a CDI system

2.1 Introduction

Energy consumption is a key figure of merit when comparing CDI to existing desalination technologies. Currently, most CDI research focuses on improving salt adsorption capabilities. There are several reported efforts on investigating the actual energy cost of a system [23, 31, 33], and comparing the thermodynamic efficiency and energy recovery of various operation strategies or modes [34–36]. However, none of these efforts identify and investigate internal resistance as a major contributor of energy loss.

Energy dissipation in a CDI system is proportional to its resistance, which can be characterized simply by the relation 2.1:

$$P = I^2 R \tag{2.1}$$

where P is the power dissipation, I is the electrical current of the system, and R is the effective resistance.

The electrical current response of a CDI cell depends on its operation modes. Various operation

modes, such as constant voltage (CV) and constant current (CC), have been examined to control energy consumption [31, 37–39]. For any mode, the Joule dissipation of energy is controlled by CDI cell resistance which is intrinsically determined by materials, cell design, and the conductivity and degree of desalination of feed water. As we review briefly later in the paper, substantial internal resistance losses are typical of CDI systems.

Challenges associated with internal resistive losses find similarities across a wide range of electrochemical systems including supercapacitors and batteries. In supercapacitors, methods to reduce internal resistance include chemically tuning the pore structure of carbon porous electrodes [40], using high concentration electrolytes [41], adding conductive additives such as carbon black [40], applying pressure at the interface between porous electrodes and current collector [42], increasing pressure and elevating temperature during electrode fabrication [43] and applying surface treatments to current collectors [44–48]. For batteries, commonly used methods for minimizing resistance include thinner electrodes, adjusting active material composition, and improving welding structures [49]. Although CDI systems are similar to supercapacitors, CDIs internal resistance has several unique features. In supercapacitors, the electrolyte type and concentration can be chosen to minimize resistance, while in CDI the ionic composition is given by the feed water. Further, CDI has the goal of reducing ion concentration, and so ionic resistance is nearly always important. Surprisingly, there is currently very limited literature on investigating resistance issues in CDI. Nugrahenny et al. coated ion-selective polymer to the surface of porous electrode to reduce contact resistance [50]. Bart van Limpt studied the relationship between electrochemical resistance and electrolyte temperature and concentration in a CDI cell [51]. To our knowledge, there is no other published work on resistance characterization of CDI systems. We here focus on a system-wide understanding of resistances in a CDI cell. We present an overview of CDI cell resistance, figures of merit for resistance evaluation, various experimental results on contact resistance, and a proposed new electrical contact configuration. Our study provides methods to both evaluate and address resistance losses in CDI systems.

In this chapter, we use various experimental methods to characterize major resistive contributors, including four-point measurements, and electrochemical impedance spectroscopy (EIS). As a test case, we characterize and focus on hierarchical carbon aerogel monoliths (HCAMs) electrodes. This material provides large surface area (~ 1500 m^2/g), high specific capacitance, and low hydraulic

resistance [52, 53]. It has been successfully applied to flow-through CDI cell architectures and demonstrated high salt removal and fast responses [30]. Although we here use HCAMs as our model system, our results, recommendations, and figures of merit are applicable to a wide range of CDI designs and electrode types.

2.2 Overview of CDI cell resistance and definitions of resistance standards

Overview of CDI cell resistance

Figure 2.1 shows our proposed simple model to characterize the impedance of a CDI cell. This model has three major components: setup resistance, contact resistance, and the impedance of the porous electrodes (a network of distributed ionic resistance of solution inside electrode, electrical double layer capacitance and electrode bulk material resistance). The total resistance of a CDI cell is then the real component of the total impedance. We here define setup resistance as the ionic resistance of the solution in the separator(s), ionic exclusion membrane (if any) resistance(s), the electrical resistance of current collectors, and resistance of any wires. Contact resistance refers to the interfacial resistance between current collector and porous electrodes. For simplicity, we here treat the porous electrode/ion solution impedance using a classical transmission line. Transmission line (TL) impedance models are commonly applied to simulate electrolyte ionic resistance and capacitance inside the pores of the electrode [30, 54, 55]. We use a TL model for porous electrodes with bimodal pore structures (with micropores integrated into a macropore network) [30]. Figure 2.1(b) shows the equivalent circuit of a CDI system: R_s, R_{ct}, and Z_{tl} are the setup resistance, contact resistance, and transmission line impedance, respectively. The transmission line impedance includes distributed solution ionic resistances (R_i), electrical double layer (EDL) capacitances (C_i), and the bulk electrical resistances of electrode solid phase (R_e). We assume that macropores determine ionic resistance and micropores dominate EDL capacitance [30]. We use a constant phase element Q_{ct} to model the interfacial capacitance of current collectors [51, 56]. This nonideal capacitor is in parallel with R_{ct}. We also extract an approximate interfacial capacitance estimate C_{ct} from the best-fit estimate of the constant phase element parameter Q_{ct} [57]. Figure 2.1(c) shows the schematic of a

typical Nyquist plot of electrochemical impedance spectroscopy (EIS) response of a CDI cell. The semiellipse is a typical response of an assembled CDI cell, and this feature is due to the parallel connection of contact resistance and interfacial capacitance of the current collector [42, 43, 56, 58]
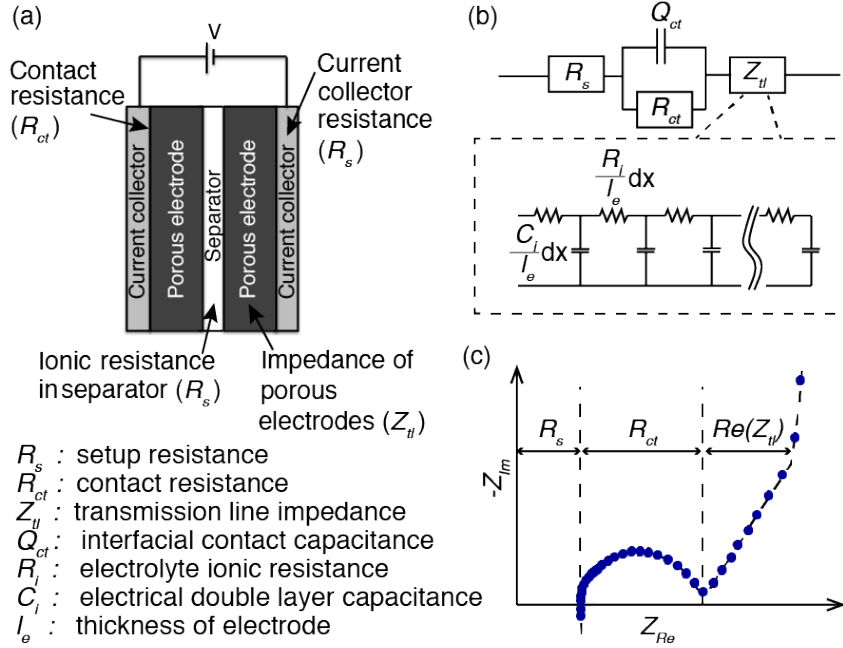
Figure 2.1: (a) Schematic of total resistance in a CDI cell. We characterize resistive components into three groups: setup resistance Rs, contact resistance R_{ct}, and transmission line impedance Z_{tl}. (b) Corresponding equivalent circuit of a CDI cell. (c) Schematic of a typical Nyquist plot of EIS response of a CDI system. The semiellipse feature is associated with contact resistance and a constant phase element of contact capacitance.

Area normalization of resistance, area-normalized equivalent series resistance and area-normalized operational nominal resistance

Perhaps the most direct way of obtaining contact resistance is from EIS. As indicated in Figure 2.1(c), setup resistance, contact resistance, and interfacial capacitance can be extracted from the semiellipse feature at high frequencies. The setup resistance is the value of the left-most intersection of semiellipse feature with axis Z_{Re}. The contact resistance R_{ct}, and constant phase element Q_{ct} are in parallel, and so the major diameter of the semiellipse feature quantifies the contact resistance value R_{ct}, and the frequency associated with the apex of the semiellipse quantifies the constant

Table 2.1: Definition of our proposed cell resistance figures of merit

Area-normalized equivalent series resistance[a] $[\Omega - cm^2]$ $(R_s + R_{ct})AN$				Area-normalized operational nominal resistance[b] (ANONR) $[\Omega - cm^2]$
constant current		constant voltage		
charging	discharging	charging	discharging	
$(\Delta V_{meas}/I_{CC})AN$	$(\Delta V_{meas}/I_{CC})AN$	$(V_{CV}/\Delta I_{meas})AN$	$-(V_{CV}/\Delta I_{meas})AN$	$(R_s + R_{ct} + 1/2R_i)AN$

[a]ANESR is a measured quantity. Subscripts CC and CV in expressions indicate the controlled/fixed parameter. Subscript meas indicates the measured values. A is the geometric area (projected in the primary direction of electrical current) for each electrode, and N is the number of cells electrically in parallel in a cell stack. [b]ANONR is a predicted parameter obtained from estimates of R_s, R_{ct}, and R_i, See Appendix A. A is the geometric area of the electrode, and N is the number of cell electrically in parallel in a cell stack.

phase element Q_{ct}, thereby providing an estimate for the interfacial contact capacitance C_{ct}. Since EIS data are not always available, we here propose two area-normalized resistance metrics that can be measured by simpler means and also extracted from published data: area- normalized equivalent series resistance (ANESR) and area- normalized operational nominal resistance (ANONR). We advocate the use of area-normalized resistances, as it allows the comparison of resistance across device designs. We use ANESR to estimate the importance of contact resistance, and ANONR as a figure of merit to evaluate the cell performance. The ANESR can be estimated from CV or CC charging/discharging profiles and cell geometries. The ANONR is approximately the upper limit of the cells effective resistance during an entire charging/discharging cycle. We summarize the evaluation equations of these two standards in Table 2.1 and provide detailed descriptions below.

Area normalization of resistance

To compare performance between CDI cell devices and designs, we propose the use of area normalization as a general standard to evaluate each resistance merit:

$$R_{abs}AN \qquad (2.2)$$

Here, R_{abs} is the absolute value of the measured or estimated resistance of interest for the CDI cell. As shown in Table 2.1, R_{abs} equals $R_s + R_{ct}$ for ANESR and $(R_s + R_{ct} + 1/2R_i)$ for ANONR. We provide example methods to measure or estimate these resistances in the Appendix A. N is the number of (electrically parallel) cells in the stack, and A is the area of each electrode. CDI devices in literature vary widely in length scales (and number of cells in parallel), ranging from a single unit with electrode areas of a few square centimeters to a full stack cell with hundreds of pairs of electrodes with each electrode area as large as a hundred square centimeters. Hence, absolute resistance (in Ohms) is not an appropriate figure of merit. We advocate the use of this area normalization as a standard to describe and compare CDI devices.

Area-normalized equivalent series resistance

In Table 2.1, we summarize the equations to obtain ANESR in each of the CC and CV modes. Within each mode, we also describe the equations of ANESR in charging and discharging states. For CC mode, we first determine absolute charging (discharging) equivalent series resistance (ESR) as the instant voltage rise (drop) very shortly after the time when constant current is applied (reversed) divided by the current, as shown in A.2a. For CV operational mode, we obtain the abso- lute charging (discharging) ESR as the constant voltage divided by the instant charging (discharging) current very shortly after the voltage is applied (removed), as shown in A.2b. As per our model, this ESR is approximately the sum of setup resistance and contact resistance: $R_s + R_{ct}$. We then normalize ESR by electrode geometric area A and cell number in a stack N to obtain ANESR, $(R_s + R_{ct})AN$. See Appendix A for more details.

Area-Normalized Operational Nominal Resistance (ANONR)

Our proposed ANONR is based on simulations of our equivalent circuit model which we performed using LTSpice (Linear Technology Corporation, Milpitas, CA). We used these to investigate current or voltage responses of a CDI cell in both CC and CV operation modes. These simulations suggest that the input current of a CDI cell in operation is approximately evenly distributed between bulk electrode resistance, R_e, and the solution ionic resistance R_i in the porous electrode (within the TL network, see Appendix B). Therefore, we can estimate the effective resistance of the TL network

of electrodes as $(R_i + R_e)/2$ during operation. Further, since R_e is everywhere in parallel with the resistance of the ionic solution, and Re is negligible compared to R_i, the TL network resistance $(R_i + R_e)/2$ can be approximated as $R_i/2$. We then estimate the absolute resistance of a cell in operation as the sum of setup resistance, contact resistance and half of the solution ionic resistance in porous electrodes: $R_s + R_c t + R_i/2$. We then normalize this absolute operational nominal resistance by electrode geometric area A and cell number in a stack N to obtain ANONR, $(R_s + R_{ct} + R_i/2)AN$. The value of ANONR is important as it sets the approximate upper limit of the cells resistance during a complete operation cycle. However, in both CV and CC mode, this resistance is difficult to measure experimentally, due to the challenge of accurately estimating the solution ionic resistance inside electrodes R_i from charging/discharging profiles. We also note that the ionic resistance R_i of a CDI cell is in fact time dependent and, of course, a function of the distributed network structure of resistances and capacitances of the electrode. We here use a nominal value of R_i to approximate the ionic resistance inside porous electrodes. R_i is estimated by modeling the porous electrodes as a large number of idealized and tortuous microchannels in parallel [59] (see Appendix A). Our proposed R_i can be interpreted as the net value of ionic resistance of the solution inside the entire electrodes in the absence of charging or discharging of its capacitance elements.

2.3   Experimental methods

Ex Situ Measurement of Contact Resistance Using a Custom Four-Point Probe

We designed a custom resistance measurement platform to characterize the ex situ contact resistance between a single porous electrode and a single metal current collector (Figure 2.2a). This measurement is a modification of standard four-point test. A 2.5 x 2.5 x 0.24 cm^3 copper plate was in facial contact with a 2 x 2 x 0.22 cm^3 HCAM piece. The actual contact area was 2 x 1.7 cm^2. Two wires were connected to the largest face of copper plate via silver epoxy with one connection in the middle, a second near the edge. The distance between the two wires was 10 mm. The HCAM piece was in contact with a custom-designed printed circuit board (PCB) (Sunstone Circuits, Mulino, OR). This PCB was designed to create two electrical contact points with the HCAM material for four-point

probe tests. The PCB included two round silver-coated contact pads 1.5 mm in diameter and with an intervening gap of 10 mm. The copper plate, HCAM piece, and PCB board were assembled and placed into an acrylic housing to accurately control the overlap area between copper plate and HCAM piece. As shown in Figure 2.2a, the assembled experiment used a copper plate and a PCB on each side of the porous electrode layer to achieve a four-point probe measurement. Current was forced through node A on copper plate, driven through the interface between copper plate and HCAM piece, then exited at node D from PCB board. A voltage difference resulting from this known current was measured between the inner two nodes B and C with a DAQ card (NI USB-6009, National Instruments, Austin, TX). This voltage difference was nearly perfectly dominated by the contact resistance at the interface. A force sensor was mounted onto the surface of upper housing piece in the middle. We used a C clamp to apply force to the device and the force is monitored through the force sensor. Figure 2.2b shows an image of the assembled experiment set up. We performed these experiments with dry HCAM samples to exclude the influence of ionic resistance and interfacial capacitance.
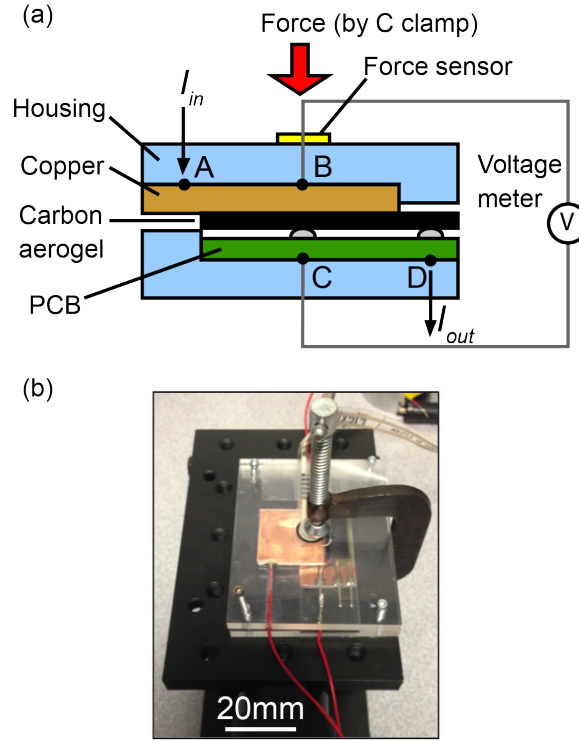
Figure 2.2: (a) Experimental setup and (b) image of custom four-point (points AD) measurement platform for ex situ characterization of contact resistance. We used a PCB board to facilitate the four-probe measurement. The PCB board, a copper plate, and a HCAM sample were aligned and held by acrylic housing and a C-clamp. The C-clamp applied external force perpendicular to the platform to compress HCAM sample against current collector. The force was monitored through a force sensor interfaced with a DAQ card.

CDI cell assembly with standard current collectors for in-situ resistance measurement

We fabricated a flow-through CDI cell design using two blocks of HCAM material with dimensions of 2 x 2 x 0.1 cm^3 for in situ resistance characterization. We used titanium plates as current collectors in the cell and a porous polypropylene separator (Celgard 3501, Charlotte, NC) to insulate between the two electrodes. The porous electrodes, separator, and current collectors were held together as an assembly using heat shrink tubing. The housing parts were fabricated from polycarbonate by CNC machining. The cell was designed to apply a known com- pression stress to the assembly by tightening two 540 screw fitted on each side of its frame.

Electrochemical impedance measurements of an assembled CDI cell

The resistance of the entire CDI cell was characterized by EIS using BioLogic SP-300 potentiostat (Bio Logic Science Claix, France). EIS was performed in a two-terminal configuration without a reference electrode since the electrodes of the cell were symmetric. We applied a 10 mV amplitude sinusoidal potential perturbation and scanned over a frequency range from 2 MHz to 10 mHz at 0 V bias. During electrochemical tests, the cell was filled with either 2 M NaCl or 100 mM NaCl. We waited 30 min before performing EIS measurements to allow the cell to equilibrate with the sodium chloride solution.

2.4 Results and discussion

2.4.1 Diagnosis of CDI cell resistances

We used our introduced figures of merit to evaluate the resistance components of our flow-through CDI cell. We obtained a typical charging profile of our flow-through CDI cell in CV mode at 1 V (see Appendix A). We divide the voltage by instant charging current to obtain an ESR as 60.9 Ω. This resistance is much larger than the setup resistance (0.5 Ω) as we estimated from solution and separator properties. This significant resistance difference was also observed by Piotr Dlugolecki et al. in their CDI system [34]. According to our CDI resistance model, we hypothesize that this significant difference is largely due to the contact resistance between current collectors and porous electrodes. To test our hypothesis, we performed EIS to the whole cell (shown in Appendix A). The major diameter of the semiellipse in Nyqist plot indicates the contact resistance between the current collector and the porous electrode. The extracted value of this contact resistance is 57.2 Ω, which constitutes 94% of the ESR in our cell. This observation draws attention to investigate the poor electrical contact between the current collector and the porous electrode and supports the hypothesis that contact resistance is the major contributor to effective resistance in CDI cells.

2.4.2 Contact resistance vs. pressure

We quantified contact resistance between a single interface of HCAM material and a copper plate using our custom four-point measurement platform. Figure 2.3a shows the results of three repeatable

runs on the same sample. The upper three curves represent the contact resistance during application of compressive stress to the HCAM against copper current collector. The lower three curves represent the reverse process as pressure was decreased and the HCAM sample recovered from compression. At the start of the compressions, with minimal pressure between the HCAM sample and copper current collector, the contact resistance was as high as 66 Ω (Figure 2.3a inset). As pressure increased, contact resistance reduces dramatically, then saturated at approximately 1.5 Ω. These trends suggest that applying a compression pressure to porous electrode and current collector can efficaciously reduce the interfacial contact resistance. We present a qualitative hypothesis for this phenomenon in Figure 2.3b. The compression force deforms the surface of porous electrode and creates additional microscopic contact regions leading to increased area between electrode and current collector. As pressure increases, the contact area saturates to a certain level. To further characterize the contact between the HCAM and our copper plate, we also performed compression tests to HCAM materials to characterize its elasticity (c.f. Appendix D). These elasticity tests suggest that, for the pressure range we selected for our compression tests of Figure 2.3a, our experiments are within the elastic response region for the HCAM. Another indicator that the HCAM was deformed elastically was the resistance values measured during release. The contact resistance half-cycles clearly show hysteresis, but the entire cycle is quite repeatable. That is, the cell repeatedly recovers to its original state, suggesting that the HCAM sample was not crushed or damaged during compression. We also performed EIS measurements on the entire CDI cell as a function of applied pressure. These experiments were conducted with 2 M NaCl solution with 10 mV sinusoidal perturbation voltage. Figure 2.4b shows Nyquist plots of EIS responses at various pressure conditions. As pressure increased from less than 1 to 30 kPa, the dominant semiellipse of the Nyquist plot shrinks.
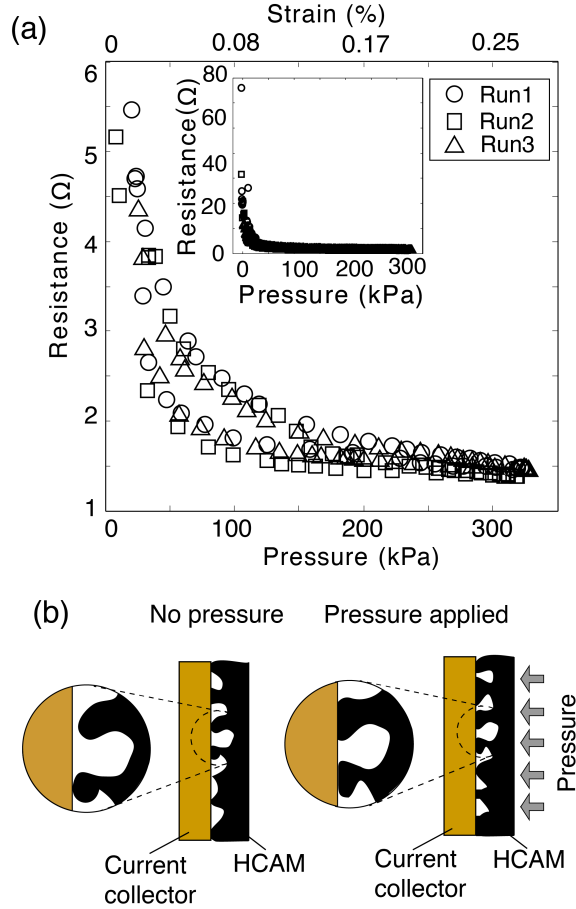
Figure 2.3: (a) Four-point measurement of contact resistance as a function of varying compressive stress/pressure. The main part is cut off at 6 in order to show the trends of contact resistance. The upper three curves are contact resistance during compression; the lower three lines are contact resistance when releasing pressure. The inset shows the full scale of the measured data. (b) Illustration of the hypothesized mechanism of reducing contact resistance by pressure. Compression deforms microscopic structures on the surface of HCAM sample and creates gradually increasing microscopic electrical contact points between electrode and current collector, and hence the contact resistance decreases.

We extracted the numbers of contact resistance and interfacial capacitance from these EIS data using the equivalent circuit of Figure 2.1b. The area-normalized values of the extracted interfacial capacitance in our experiments are close to the reported double-layer capacitance of a metallic substrate interfacing with electrolyte [60]. This is further evidence that the semiellipse in Nyquist plot is associated with contact resistance and the parallel interfacial capacitance associated with

the interface between the porous electrodes and current collectors. From the extracted numbers, the contact resistance, which is associated with the major diameter of the semiellipse, decreased from 8.8 to 5.5 , nearly 40% reduction. At the same time, the interfacial capacitance was reduced by 7.7% from 22.0 F to 20.3 F. The capacitance did not change substantially, but appeared to trend downward with increased pressure. These trends suggest that contact area was created at the expense of reducing the capacitive surface, and that the sum of the microscopic electrical contact area and interfacial capacitance surface area was not constant. Therefore, these data again support the view that applying pressure to press porous electrodes against current collectors is an effective way to reduce contact resistance.
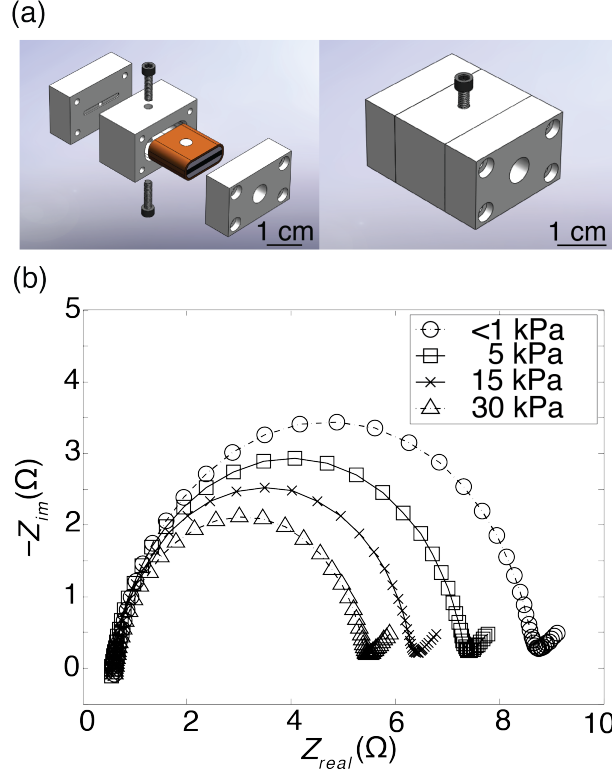
Figure 2.4: (a) Schematic of full, two-electrode flow-through CDI with compression controllable by two screws in the assembly. The electrode assembly consists of two 2 x 2 x 0.1 cm^3 HCAM pieces, a 25 μm thick porous dielectric separator, and two 2 x 2 x 0.25 cm^3 titanium current collectors. Two screws were used to apply pressure to the electrode assembly. (b) Nyquist plot of flow-through CDI cell under four pressure states. These EIS tests were performed with 2 M NaCl electrolyte. The semiellipse shrunk as applied pressure increased. The value of contact resistance extracted from EIS data reduced from 8.8 Ω to 5.5 Ω as pressure increased from <1 to 30 kPa.

We note that the semiellipse of the EIS measurements and our attribution of this feature to contact resistance is consistent with similar phenomena which have been observed in related fields, including lithium-ion batteries [58], supercapacitors [42–44, 47], and electroceramic systems [61]. Lei et al. reported the reduction of contact resistance in porous carbon/Al electrical double layer supercapacitors by putting weights on the body of the devices [42]. Dsoke et al. showed that the contact resistance between current collector and composite carbon electrode in supercapacitors could be improved by properly regulating processing parameters, such as temperature and pressure [43].

Hwang et al. demonstrated that mechanical loading reduced the contact impedance of gold electrodes on nanophase cerium dioxide in electroceramic system [61]. We note these non-CDI studies all reported only qualitative EIS data. Also, their systems of interest were describable by different circuit elements and/or by limiting factors different than our CDI system. As far as we know, our work is the first study to quantitatively investigate contact resistance in CDI systems.

2.4.3 Proposed contact configuration

We investigated and here propose an alternative contact configuration for contact between a porous electrode and a current collector. We used high conductivity silver epoxy (CW2400, CircuitWorks, Waukegan, IL) to create a spot contact between the porous electrode and copper wire along the thin edge of HCAM sample (Figure 2.5a). This thin edge connection (versus connection at the face) is convenient for stacks of electrodes and separators and is also more relevant to flow-through CDI cell architectures (e.g., a silver epoxy contact on the large flat face would block liquid flow normal to the large face of the porous electrodes). By infiltrating silver epoxy into a small region of the porous electrode, we created an intimate electrical contact between the HCAM substrate and current collector. Figure 2.5b qualitatively visualizes the principle behind this reduction of total cell resistance by employing this new contacting configuration. Silver epoxy fills into the microscopic voids between porous electrode and current collector; greatly increase contact area to the HCAM.

In Figure 2.5c, we show an example quantification of the effect of this contact method. The plot shows two comparative EIS experiments of assembled EIS cells performed with 100 mM NaCl solution, to simulate the desalination of brackish water [23]. The semiellipse was completely eliminated from the Nyquist plot, showing the significant reduction of interfacial contact resistance. From the CV/CC charging/discharging cycle data Table 2.2, we extracted that the contact resistance reduced to 7.5 Ω using silver epoxy contact, compared to 63 Ω when using titanium plate contact. In addition, the resistance value of the first intersection point with the real axis, namely the setup resistance, was also reduced from 5.9 to 1.5 Ω (a 4-fold reduction). We hypothesize that we can further reduce series resistance in CDI cells by using multiple-spot silver epoxy contacts on the same edge of the electrode. We note here the difference of measured setup resistances of these two contact configurations was due to different wirings. The measured 5.9 Ω of the plate contact configuration

(shown in Figure 2.4b) included the additional resistance from screws and the contact resistance between screws and current collectors, whereas the silver epoxy contact configuration only included setup resistance and silver epoxy resistance. It is worth noting that a directly exposed silver epoxy connection may dissolve or corrode during CDI operation. However, we did not observe noticeable degradation of performance of silver epoxy con- tact in our system within 4 months of operation. One way to address the corrosion problem is to cover the solver epoxy contact with one or more protection layers, such as epoxy resin (as has been done in other electrochemical systems [62, 63]) or silicone.

We note that, given minimal resistance contacts, the resistivity of HCAM samples may become a limiting factor for resistance minimization. For example, contact at the thin edge of an electrode forces electrical current to flow in-plane through small cross-section of the porous electrode. A recent study on 3D bulk nanographene suggests that the resistivity of graphitic carbon materials varies as a function of applied voltages, due to the electrochemically induced accumulation or depletion of charge carriers in combination with a large variation in the carrier mobility [64]. Since HCAMs have high graphitic content, we expect that HCAM may exhibit similar properties. Future work on resistivity change induced by charge accumulation under operational conditions is needed to further characterize the total resistance in CDI systems. Overall, intimate electrical contact (e.g., using the silver epoxy method described here) between a CDI porous electrode and a current collector demonstrates significant improvement regarding minimization of total series resistance of CDI systems.
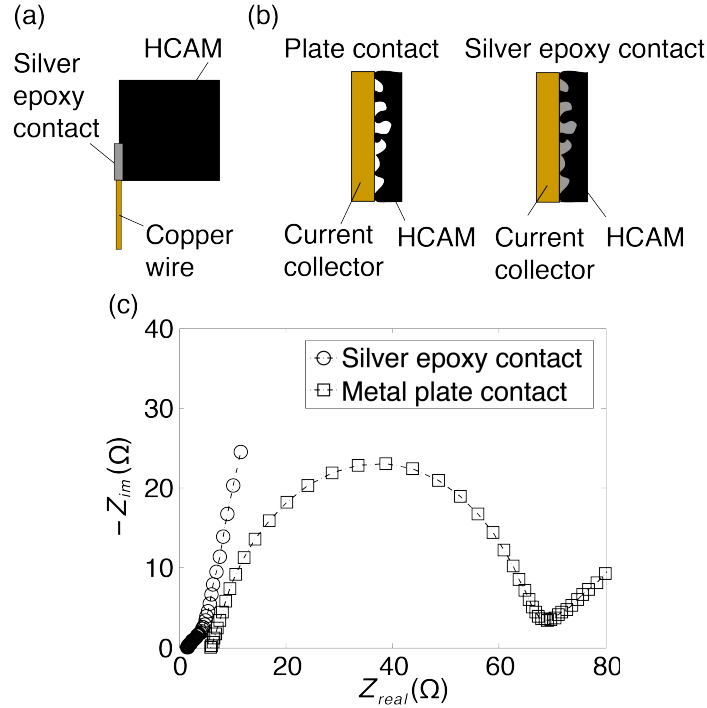
Figure 2.5: (a) Schematic of full, two-electrode flow-through CDI with compression controllable by two screws in the assembly. The electrode assembly consists of two 2 x 2 x 0.1 cm^3 HCAM pieces, a 25 μm thick porous dielectric separator, and two 2 x 2 x 0.25 cm^3 titanium current collectors. Two screws were used to apply pressure to the electrode assembly. (b) Nyquist plot of flow-through CDI cell under four pressure states. These EIS tests were performed with 2 M NaCl electrolyte. The semiellipse shrunk as applied pressure increased. The value of contact resistance extracted from EIS data reduced from 8.8 Ω to 5.5 Ω as pressure increased from <1 to 30 kPa.

2.4.4   Review of reported CDI cell resistances

To extend our observations and conclusions to other CDI systems, we have reviewed published reports of CDI cells, and reported resistance values strongly imply that series resistances is a key issue for CDI systems. From the publications that we reviewed, we can easily extract ESR ($R_s + R_{ct}$) and ANESR ($R_s + R_{ct})NA$ from CV mode or CC mode charging/discharging profiles and cell geometries as we described, and estimate resistance R_s and R_i using reported properties of salt solutions, separators, and electrodes (see Appendix A). Subtracting the calculated R_s value from reported ESR, we obtain an estimate of the missing resistance. In our cell, according to our model and studies on contact resistance, we have demonstrated that this missing resistance is due to the poor electrical contact

between current collector and porous electrodes. For other CDI cells reported in the literature, we hypothesize that this missing resistance is also predominantly contact resistance between the current collector and the porous electrode. We here review several instructive examples. Zhao et al. demonstrated a membrane capacitive deionization (MCDI) cell with CC operational mode [31, 38]. The reported ESR of their prototype cell is 0.7 Ω as a stack of eight individual cells (5.6 Ω per cell) with 20 mM NaCl solution. However, we estimate that the sum of the ionic resistance in separator, wires and membranes is only about 0.08 Ω as a stack (0.6 Ω per cell), constituting only 11% of reported entire cell resistance. In other words, nearly 90% of the resistance may be contact resistance.Garcia-Quismondoetal. demonstrated a method to isolate the effects between charging and discharging cycles with their flow-between CDI reactor [37]. Their cell had an ESR of 0.3 Ω as a stack (2.4 Ω per cell) in CC operation mode, whereas our calculated estimate of their setup resistance is only 0.05 Ω as a stack (0.4 Ω per cell). And so 83% of the ESR was possibly from the electrical contact. We summarized the reported resistance of each published CDI cell that we reviewed, and the associated resistance estimates in Table 2.2. These reported values of cell resistance support strongly the hypothesis that contact resistance nearly always dominates cell resistance for reported devices

Table 2.2: Review of cell resistance figures of merit from published CDI studies.

first author/ publication year	cell stack no.(N)	area of electrode per cell (A) cm²	thickness of electrode [μm]	salt solution condcutivity [mS/cm]	operation mode (CV or CC)	estimated R_s[Ω]	estimated contact resistance R_{ct}^b[Ω]	estimated ionic resistance R_i[Ω]	area-normalized contact resistance $R_{ct}AN$[Ω]	charging ANESR $(R_s + R_{ct})AN$[Ω· cm²]	discharging ANESR $(R_s + R_{ct})AN$[Ω· cm²]	area-normalized operational nominal resistance (ANONR) $(R_s + R_{ct} + 1/2R_i)AN^a$ [Ω· cm²]
Farmer/ 1996[32]	192	47.1	127	1.0	CV	0.007	0.05	0.013	452	515	605	571
Wang/ 2006[65]	1	55.7	250	0.19	CV	9.6	25.4	20.3	1415	1950	4179^c	2517
Kim/2010[66]	1	99.2	330	0.42	CV	0.6	6.9	6.4	687	744	149^c	1059
Porada/ 2012[67]	8	33.8	270	0.55	CV	0.3	4.8	1.5	1290	1370	1201	1569
Zhao/2012[31]	8	33.8	362	2.16	CV,CC	0.1	0.6	0.54	161	189	135	263
Suss/2012[30]	1	4.0	1000	10.7	CV	0.5	29.5	20.4	118	120	NA	160
Garcia-Quismondo[37]	8	318	3000	1.7	CC	0.05	0.3	0.6	638	763	560	1535
our cell	1	4.0	1000	10.7	CC, CV	0.5	7.5	20.4	30	32.0	NA	72.8

^{a}To estimate operational nominal resistance, we used typically reported tortuosity and porosity numbers for activated carbon and carbon aerogel materials: $\tau_e = 3.5$ [68, 69]; $\psi_e = 0.8$. ^{b}Contact resistance is estimated by subtracting estimated R_s from measured charging ESR $(R_s + R_{ct})^c$. ^{c}Charging resistance and discharging resistances show a significance difference, and this may be due to incomplete charging or discharging.

2.5 Conclusions

In this chapter, we report our efforts to characterize resistance components in capacitive deionization (CDI) systems. We propose two area-normalized standards as a merit matrix to evaluate resistances across CDI devices: area-normalized equivalent series resistance and area-normalized operational nominal resistance. We found that the contact resistance between current collector and porous electrode was the major contributor of series resistance in our CDI cell, and we think that it is also the main resistance component in published CDI cells we reviewed. We further propose and demonstrate two methods to minimize contact resistance. The first is application of sufficient pressure to press porous electrodes against current collectors. The second is an alternative and convenient electrical contact configuration: providing intimate contact between the porous electrode and current collector. By implementing our methods, the energy cost of CDI could be reduced by up to 88% and makes CDI the most energy efficient desalination method for low-salinity waters. On the basis of the study by Zhao et al., if the contact resistance could be eliminated, the energy cost of CDI would be lower than RO by as much as a factor of 4 to 20 for the salt concentration ranging from 1.2 g/L to 4 g/L [33].

Lastly, we note that, surprisingly, characteristic cell resistances are rarely reported in published studies of CDI cells. Energy consumption is a key figure of merit for the performance of CDI, and resistance is an important factor. We suggest that reporting device resistance should become a standard metric for CDI publications, just as removal capacity and removal rate have already become, and we recommend use of our proposed two area-normalized resistance metrics.

Chapter 3

Energy consumption analysis of CV and CC operations

3.1 Introduction

Energy consumption is a crucial factor when comparing CDI to state-of-the-art desalination technology, reverse osmosis (RO) [29, 70]. A CDI cell can be operated at various charging modes including constant voltage (CV) [28, 71–73] and constant current (CC) [31, 33, 37, 38, 73–76]. Different modes lead to discrepant energy consumption patterns. Zhao et al [31] and Choi [77] reported lower energy consumption for CC-operation than CV-operation for membrane capacitive deionization (MCDI) cells. Kang et al. demonstrated that CC mode consumed 26% -30% less energy than that consumed in CV mode with the same amount of ions removed [39]. Recently, Han et al. showed that CV mode consumed approximately 50% more energy than CC mode, and only 5.7% of the total energy consumption in charging process in CV mode was recovered in contrast to up to 40% in CC mode [75]. Although these experimental observations have suggested that CC mode is more energy efficient, a thorough understanding of why CC mode consumes less energy than CV mode is missing. Kang et al. attributed lower energy consumption of CC to its overall lower cell voltage [39]. The work we present here will show that the latter argument is ambiguous and strictly inaccurate since the energy saving of CC operation over CV (for equal charge and charging duration) is insensitive to

operational voltages of CC. Further, as with most studies, there is no significant effort to make fair comparison between the two modes (e.g., charging to the same net charge for equal time).

Fundamentally, energy dissipates as currents pass through resistances in the form heat. The underlying reason that CC consumes less energy than CV is that, in CC operation, the cell dissipates less power through resistive components, as CC has better control of charging cur- rents. Another energy consumption advantage of CC is that CC decreases the time the cell operates under conditions where electrode-to-solution potentials result in parasitic (Faraday) reactions. We also note that all of the aforementioned studies report energy consumption as the amount of electrical energy applied to a CDI cell in charging. Instead, we here define this Energy input a value equal to the time integral of charging power (product of charging voltage and current) of the external power source to a CDI cell. Note that it is inaccurate to equate energy input and energy consumption. Only a fraction of the energy input is dissipated/consumed by the cell, a second important fraction is instead stored within the cell as capacitive energy in electrical double layers. This stored energy is recoverable (not part of energy consumed). Experimentally, will quantify recoverable energy using a low current discharge. Under low current discharge, energy dissipated by resistances and parasitic reactions in the cell are small compared to the recoverable electrical capacitance. Such recovered energy can be stored externally (e.g. in supercapacitors or batteries) or used by other devices, including other CDI cells. We advocate to the community that energy consumption of CDI processes should be the unrecoverable, dissipated energy during an operation cycle, and should not include stored capacitive energy.

In this chapter, we present two electrical circuit models to simulate and compare energy consumption of CC and CV operation modes. The first model is a simple RC circuit model, and the second is an experimentally validated circuit model based on classic transmission line theory to simulate a capacitance and resistance network. We validate simulation results by performing experiments with a flow-through CDI (ftCDI) cell made of hierarchical carbon aerogel monoliths (HCAMs) electrodes, as shown in (Fig. 3.1a and 3.1b). We demonstrate that CC consumes less energy than CV with the same amount of charge transferred and within the identical operation timespan. For our comparison, the two modes also achieve similar charge efficiency. We attribute lower consumption of CC mode to less resistive dissipation in the charging process. As far as we know, our work is the

first study centered on the underlying physics of why CC consumes less energy than CV operations for CDI cells. Although we here use ftCDI cell as our model system, our results and conclusions are applicable to flow-between CDI cells and operations. We note that our study might not apply to membrane CDI (MCDI) because other energy loss mechanisms in MCDI, such as energy loss associate with ions overcoming membrane barriers, are not captured by our models and analysis.
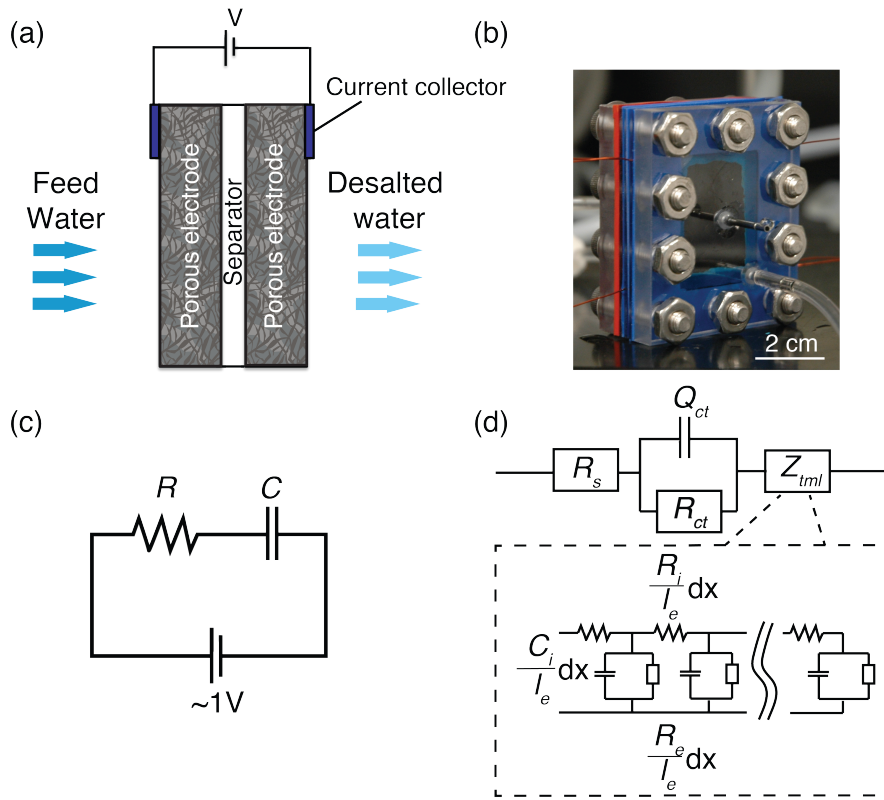
Figure 3.1: (a) Schematic and (b) image of a flow-through CDI cell. The cell consists a pair of 300 μm thick porous carbon electrodes, an 80 μm porous dielectric separator, two metal current collectors and wires. (c) Simple RC circuit model for a CDI cell. (d) Equivalent circuit of a CDI cell based on transmission line impedance model.

3.2   Energy consumption analysis

3.2.1   Simple RC circuit analysis

For first-order analysis of energy dissipation in charging, we model a CDI cell as a simple RC circuit: a capacitor C in series with a resistor R, as shown in Fig. 3.1c. This model is perhaps the simplest but still powerful for understanding energy consumption associated with charging and discharging process in CDI. Here, the capacitor C represents the total electrical double layer capacitance for salt adsorption and the resistor R represents an equivalent total resistance of the cell. To create the simplest model which nevertheless offers valuable insight, we here assume that the capacitance and resistance remain the same during charging or discharging process. We consider comparisons where we charge over the same time and equal amounts of charge.

Fundamentally, energy dissipates through the resistive components of a CDI cell in the form of heat. The dissipation power of a CDI cell is proportional to its resistance and the square of response current: $P = I^2 R$. Here the current response I is determined by electrical operation modes, and CC and CV modes have distinguished energy consumption patterns as we further discuss in the paper.

We analyze energy consumption of CV and CC operations under the conditions of finite charging time and the same amount of input charge. For CV operation, the current response of a CDI cell is

$$I(t) = \frac{V_{CV}}{R} e^{-\frac{t}{RC}}. \tag{3.1}$$

Here V_{CV} is the constant voltage applied to the CDI cell. R is the total equivalent resistance and C is the total double layer capacitance. The instantaneous dissipation power is then

$$P_{CV}(t) = I(t)^2 R = \frac{V_{CV}^2}{R} e^{-2t/RC}. \tag{3.2}$$

If the cell is charged to finite time t, the charge transferred to a CDI cell and the accumulated dissipated energy are

$$q_{CV}(t) = \int_0^t \frac{V_{CV}}{R} e^{-t/RC} dt = V_{CV} C (1 - e^{-(t/RC)}), \tag{3.3}$$

$$E_{CV}(t) = \int_0^t P(t)dt = \int_0^t \frac{V_{CV}^2}{R} e^{-2t/RC} dt = \frac{1}{2} CV_{CV}^2 (1 - e^{-(2t/RC)}). \tag{3.4}$$

As per Eq. 3.4, for finite charging time and fixed C and V_{CV}, CV energy consumption is a strong function of resistance R and charging time t. We note that if a CDI cell is charged to infinite time, the energy consumption is $CV^2/2$. However, in practical applications, we cannot and would not want to charge a CDI cell for very long times as this leads to very slow salt removal rate and poor water recovery. We here use a total resistance R as 7.64 Ω and capacitance C as 3.84 F, based on values characterized for our CDI cell. We plot energy consumption of CV mode as a function of time in Appendix B.

For CC operational mode, the dissipated energy of a RC circuit is simply:

$$E_{CC}(t) = I_{CC}^2 Rt. \tag{3.5}$$

For a fair comparison, we charge a cell at CC mode for a duration of time t such that the charge transferred is the same as that in CV mode within the identical timespan. As we later show that electric charge is a good proxy for salt removal, these comparison conditions imply a similar salt removal rate for both CV and CC.

The unique value of equivalent constant charging current I_{CC} is then

$$I_{CC} = \frac{q_{CV}}{t} = \frac{V_{CV}C(1 - e^{-t/RC})}{t} \tag{3.6}$$

Here q_{CV} is the accumulated charge and V_{CV} is the voltage applied in the counterpart CV mode to which we compared.

The energy consumption for the equivalent CC mode described above is:

$$E_{CC}(t) = \int_0^t I_{CC}^2 Rdt = I_{CC}^2 R \int_0^t dt = \frac{V_{CV}^2 C^2 R}{t} (1 - e^{-t/RC})^2. \tag{3.7}$$

This equivalent energy consumption is again a strong function of resistance R and charging time t. We plot E_{CC} as a function of time in Appendix B.

Combining Eqs. 3.4 and 3.7, the ratio of energy consumption of constant voltage and constant

current is

$$\frac{E_{CC}}{E_{CV}}(t) = \frac{2RC}{t}\frac{1 - e^{-t/RC}}{1 + e^{-t/RC}} \tag{3.8}$$

Perhaps surprisingly, this ratio is always smaller than unity regardless of the values of resistance R and capacitance C (Appendix B). This simple model therefore suggests CC operation always consumes less energy than CV for the same amounts of input charge and for identical timespans. In addition, energy consumption for either CV or CC mode strongly depends on the equivalent total resistance R.

3.2.2 Transmission-line based circuit model and simulations in LTspice

The resistive and capacitive components in a CDI cell are much more complex than a simple RC circuit. The simple RC circuit is unable to capture the non-uniform charging dynamics of a porous electrode, and it does not include charge loss mechanisms, such as parasitic reactions on electrode surface [28, 29, 78–80]. To further understand the energy consumption in charging process in a CDI cell, we use an equivalent circuit model based on classical transmission line (TL) theory. Transmission line impedance models are commonly used to simulate resistance and capacitance network in porous electrodes [53–55, 70, 81]. In our model, we have a setup resistance (ionic resistance of the solution in the separators and electrical resistance of current collectors and wires), a contact resistance to model the contact between current collectors and porous electrodes, and two porous electrodes each modeled as a TL with 20 resistor-capacitor units (Appendix B). Each resistor-capacitor unit consists of an EDL capacitor element, an ionic resistance element, an electrode resistance element, and a leakage resistance element which models parasitic reactions. We use a voltage-dependent non-linear relationship that follows Butler-Volmer equation for leakage resistors. We assume constant EDL capacitance and ionic resistance in our simulations because there is no significant ion depletion during charging at the feed concentrations we use in experiments. Further, constant capacitance and ionic resistance elements generate simulation results which sufficiently well match experimental data (see Results and discussion). We perform simulations with our equivalent circuit model in an integrated circuit simulator LTspice to study dynamic current and voltage responses and evaluate energy dissipations. Simulation conditions are determined by experiments. All the resistive and capacitive values in the LTspice model match those in experiments, as we later describe in Material

and methods. Fig. 3.2 compares simulated cell responses to experimental data in CV and CC modes, which shows that transmission line based LTspice model captures charging dynamics of a CDI cell well. We determine the energy consumption of CC and CV modes in modeling by summing up the dissipation energy of all resistive elements, as shown below:

$$E = \sum_{m=1}^{N_i} \int_{t_0}^{t_1} I_{R_{i(m)}}^2 R_{i(m)} dt + \sum_{k=1}^{N_e} \int_{t_0}^{t_1} I_{R_{e(k)}}^2 R_{e(k)} dt + \sum_{n=1}^{N_{leak}} \int_{t_0}^{t_1} I_{R_{leak(n)}}^2 R_{leak(n)} dt + \int_{t_0}^{t_1} I_{R_s}^2 R_s dt + \int_{t_0}^{t_1} I_{R_{ct}}^2 R_{ct} dt$$

$$(3.9)$$

where t_0 and t_1 represent start and end time points of charging process. $R_{i(m)}$ and $R_{e(k)}$ are transmission line resistor elements representing ionic resistance inside pores and electrical bulk resistance of porous materials. N_i and N_e are the numbers of R_i and R_e elements in LTspice simulation, respectively. In our model, we have $N_i = 38$ and $N_e = 40$ (arbitrarily chosen). $R_{leak(n)}$ simulates parasitic reactions across EDL capacitor. N_{leak} is the number of $R_{leak(n)}$ element in the model and we have $N_{leak} = 40$. R_{ct} is the contact resistance between current collector and porous electrode. R_s is the setup resistance as we defined earlier.
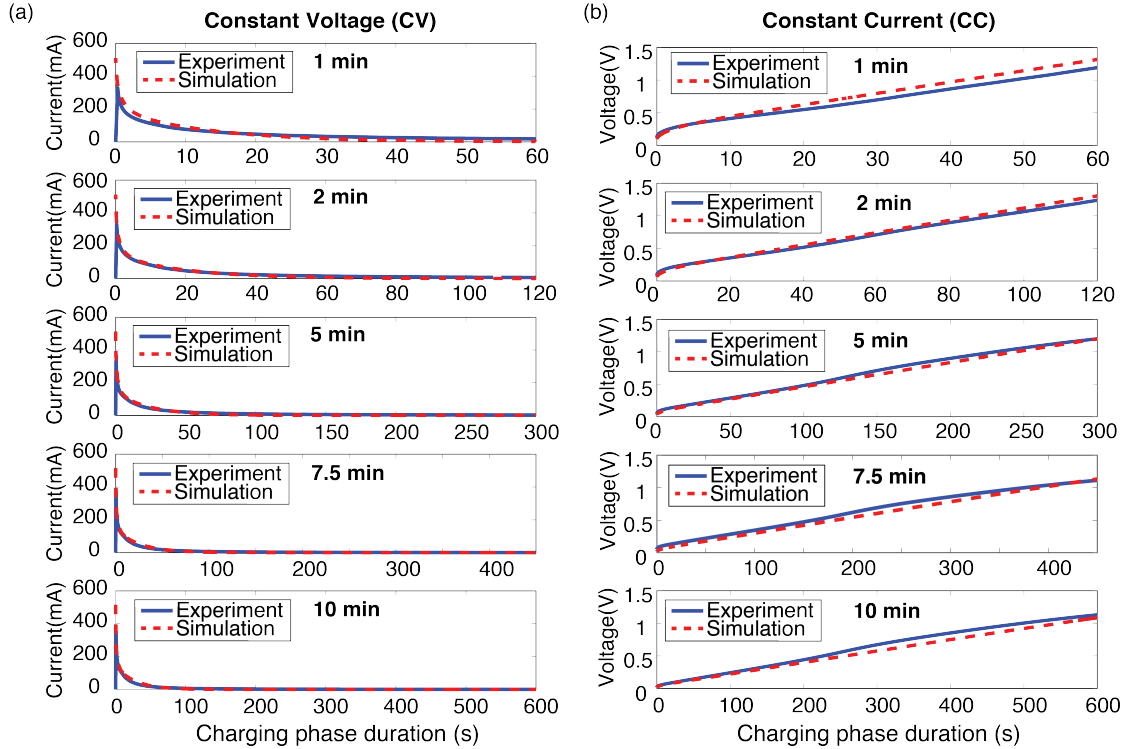
Figure 3.2: (a) Experimental and simulated current responses of a CDI cell under 1 V CV operation with charging phase durations of 1, 2, 5, 7.5 and 10 min. (b) Experimental and simulated voltage responses of a CDI cell under equivalent CC operations with charging phase durations of 1, 2, 5, 7.5 and 10 min. Solid blue lines represent experimental data and red dash lines represent simulation results.

3.3   Materials and methods

Flow-through CDI cell

We fabricated a flow-through CDI cell design using two blocks of hierarchical carbon aerogel monoliths (HCAMs) material [30, 52, 53, 70, 82, 83] with area of 2 x 3 cm and thickness of 300 μm, for CV and CC comparison experiments, as shown in Fig. 3.1a and b. We used an 80 μm thick hydrophilic PTFE membrane filter (JCWP04700, EMD Millipore, Billerica, MA) as a separator to insulate between the two electrodes. We used silver epoxy to create intimate electrical contacts between HCAM electrodes and copper wires [70]. The two porous electrodes and a separator were stacked into an assembly and glued on to a polycarbonate frame using epoxy. This assembly was

then sandwiched between two 4.2 x 5.0 x 0.6 cm polycarbonate endplates with 630 μm silicone rubber sheets as gaskets. Both endplates were milled to accommodate a tubulation as a port to flow water. The cell was assembled using ten bolts. The cell assembly frame and housing parts were fabricated from polycarbonate.

ftCDI cell characterization

We characterized capacitance of our ftCDI cell by performing cyclic voltammetry using BioLogic SP-300 potentiostat (Bio Logic Science Claix, France). Apparent capacitances obtained from cyclic voltammetry are well known to depend on scan rates, and slow scan rates generate capacitance readings closer to equilibrium capacitances [84–86]. To accurately evaluate the equilibrium capacitance in a CDI cell, we performed cyclic voltammetry at a slow scan rate of 1.67 mV/s, as shown in Appendix D. We then extracted capacitance from cyclic voltammetry data and applied it as an input parameter to LTspice model.

The resistances of the entire CDI cell were characterized by electrochemical impedance spectroscopy (EIS) using a potentiostat [70]. EIS was performed in a two-terminal configuration without a reference electrode since the electrodes of the cell were symmetric. We applied a 10 mV amplitude sinusoidal potential perturbation and scanned over a frequency range from 700 kHz to 10 mHz at 0 V bias. During electrochemical tests, the cell was filled with 100 mM NaCl. We waited 30 min before performing EIS measurements to allow the cell to equilibrate with the sodium chloride solution. We extracted setup resistance R_s, contact resistance R_{ct} and ionic resistance inside porous electrodes R_i from Nyquist plot of EIS responses (Appendix D) and then used them as parameters in LTspice simulations. We characterized parasitic reaction currents by performing constant voltage experiments at 0.2, 0.4, 0.6, 0.8, 1.0 and 1.2 V while flowing feed solution through the cell, and recorded leakage currents after 10 min of charging. 10 min is much longer than the CDI cell's RC time constant (about 25 s). Therefore, we assume that the currents we observed at 10 min were due to parasitic reactions, not because of EDL charging. We then fitted leakage currents data to obtain a Bulter-Volmer equation to characterize voltage-dependent parasitic reactions (Appendix D).

Constant voltage and constant current charging experiments

We performed CV and CC experiments using our CDI cell with 100 mM NaCl. With this concentration, there is no significant ion depletion in the cell during charging. We used a Biologic SP-300 potentiostat (Bio Logic Science Claix, France) to supply voltage or current and monitor electrical responses. A flow-through conductivity sensor (Edaq, Denistone East, Australia) was attached to the CDI cell downstream to measure the conductivity of effluent solution. We used a syringe pump (Harvard Apparatus syringe pump, Holliston, MA) to flow feed solution through the cell at 0.24 mL/min. We waited 30 min before starting experiments to allow the cell to equilibrate with sodium chloride solutions.

We first performed CV experiments at 1 V with charging phase durations of 1, 2, 5, 7.5 and 10 min. We obtained the total amounts of charge transferred from potentiostat to the CDI cell by integrating current responses over charging times. To satisfy the conditions of the same input charge and identical timespan, we determined the charging currents for counterpart CC experiments by dividing accumulated charge measured in the CV experiment by total charging time. We then performed counterpart CC experiments for 1, 2, 5, 7.5 and 10 min with the corresponding equivalent currents. For each experiment, we performed two charging and discharging cycles. In both cycles, the charging steps followed preset experiment conditions. For discharging in the first cycle, we drew a very small discharging current (2 mA) from the cell to extract an estimate of stored energy in EDL. In second cycle, we held the cell at open circuit state for 15 min after charging to flush desalted water in order to obtain more accurate estimates of salt removal. We then grounded the cell for 10 min to ensure complete regeneration of electrodes prior to the next charging.

3.4 Results and discussion

3.4.1 Model validation

As discussed above, the parameters of our LTSpice model are determined using independent experiments using cyclic voltammetry, EIS and leakage current experiments. We then use our LTSpice model to make predictions of the CDI cell in operational modes.

To validate the performance of our LTSpice model, we compared simulated voltage and current

responses of the ftCDI cell to experimental data. Fig. 3.2a shows experimental and simulation data of current responses of the cell under 1 V CV operation with 1, 2, 5, 7.5 and 10 min charging phase durations. Fig. 3.2b shows experimental and simulation data of voltage responses of the CDI cell under corresponding CC conditions with the same set of charging phase durations. Simulation results from LTspice model demonstrate fair agreement with experimental data, especially for longer charging times. This agreement validates the use of a transmission line based circuit model to predict electrical charging dynamics and energy consumptions of a CDI cell. Our primary use of this model will be to study the differences between CC and CV energy dissipation.

For our LTspice circuit model, we chose to implement constant capacitor elements. We view this circuit model as the simplest transmission line model which nevertheless sufficiently captures the physics of CDI operation and helps us compare CC versus CV operations. In the Supplementary Information document, we show cyclic voltammetry characterizations (Appendix D) which explore the net capacitances of our cell. The cyclic voltammetry data capture some voltage dependence of differential capacitance. However, we avoided fitting such data to obtain capacitance versus voltage relations since it is difficult to decouple the effects of capacitance changes versus parasitic reactions in the system. We do not know of a straight forward manner to decouple these confounding effects. Future work could include exploring the relative importance of changes in capacitance versus parasitic reaction effects, and including extending our model to include voltage-dependent capacitances. Our experience so far in exploring this issue is that constant capacitance models are likely sufficiently accurate for operation at higher ionic strengths of the inlet (order 100 mM salt concentration or greater).

3.4.2   Energy input and energy consumption comparison

We obtain energy inputs to CDI cell by integrating the product of cell voltage and current over charging times, as described by Eq. 3.10:

$$E_{in} = \int_0^t I_{cell} V_{cell} dt \tag{3.10}$$

This energy input calculation applies to either CV or CC operation. In CV mode, V_{cell} is fixed and I_{cell} is the cell's current in response. In CC mode, V_{cell} is the measured and I_{cell} is fixed. Fig.

3a shows the compari- sons of energy inputs of CV and CC modes in experiments and simula- tions as a function of duration of the charging phase. For each set of data, we first performed CV runs and used measured time-integrated current to calculate electric charge transferred to the cell. We then choose corresponding current values for the CC experiments to source the (unique) applied current to transfer the same charge in the same time as the CV experiment.

Fig. 3.3a presents two sets of simulations results for CC mode. The first set are predictions of the CC circuit model given the applied (experimental) current. These CC current values therefore ensure the corresponding CC and CV experiments have identical electric charge transferred in identical charging phase times. As a reference and comparison, we also show CC circuit model predictions for corresponding current values which are predicted by the transferred charge predicted by the CV model. The latter data therefore ensure that the CV and CC predictions have identical electric charge transferred in identical charging timespans. Note the discrepancy between the latter prediction and experiments for short charging phase durations. We attribute this to the effect of increased ionic resistance in the cell for CV operation. The residence time of flow in the cell (solution volume inside the cell divided by flow rate) is about 56 s. For charging phase duration of this order (or shorter), the rapid initial ionic charge trapping of the CV mode results in a short-term rise in ionic resistance; and such changes are not accounted for in the model (which assumes constant resistances). For longer cycle times, the solution inside the cell is well replenished by the flow and the measured time-average resistance loss are closer to those predicted. We determine energy consumption for both simulations and experiments. In simulations, energy consumption is calculated as the sum of the dissipation energy of all resistive elements in model (i.e., Equation 3.9) and dissipation of the parasitic reaction circuit elements. In the experiments, we follow cell charging by discharging at a low current to evaluate energy consumptions (as we described in Material and methods). This low-current discharge lets us estimate recoverable output energy. For the experiments, we therefore estimate energy consumption during charging by subtracting from input energy the following three energy values: recoverable output energy, resistive dissipation energy in discharging, and parasitic reaction energy in discharging. The latter is estimated using our Bulter-Volmer model for parasitic current (see Appendix C). We can express the estimate for energy consumed during charging in the experiments as follows:

$$E = E_{in} - E_{out} - \int_{t1}^{t2} I_{dis}^2 R_{cell} dt - E_{parasitic,dis} \qquad (3.11)$$

Here, $t1$ and $t2$ represent start and end time points of discharging phase. E is energy consumption in charging process. E_{in} represents input energy as measured by the potentiostat to the CDI cell. E_{out} is the recoverable output energy from EDL and it is obtained by discharging the cell at a very small constant current. $\int_{t1}^{t2} I_{dis}^2 R_{cell} dt$ represent resistive dissipation associated with small current discharging, where R_{cell} is the total equivalent resistance of the CDI cell and I_{dis} is the discharging current (2 mA in our case). $E_{parasitic,dis}$ is the estimate energy consumed by parasitic reactions during discharging. $E_{parasitic,dis}$ is the time integral of the product of parasitic current and cell voltage. Note (potentiostat) voltage is expected to be a good estimate of potential across surface charge layers (and therefore the potential parameter in the Bulter-Volmer equation) for such low currents.

Fig. 3.3b shows simulated and experimental energy consumption of CV and CC operations during charging process. With either fast or slow charging rates, CV consumes significantly higher energy than CC under the condition that the same amounts of charge are transferred to the cell within the identical charging timespans. We note here that the salt removals are comparable in CV and CC experiments, as we dis- cuss further in next section. Our model successfully predicts the same major conclusion that CC is more energy efficient than CV for equal charge and charging phase duration. The model results therefore support the hypothesis that the lower energy consumption of CC in charging is due to its lower resistive dissipation. We note that there is some discrepancy between model and experiments for both the CC and CV cases, particularly for charge phase durations of order 100 s or less. As mentioned above, we attribute this discrepancy to the rapid initial rise of ionic resistance associated with CV operation. Our model does not capture such rapid-changing ionic resistance changes.
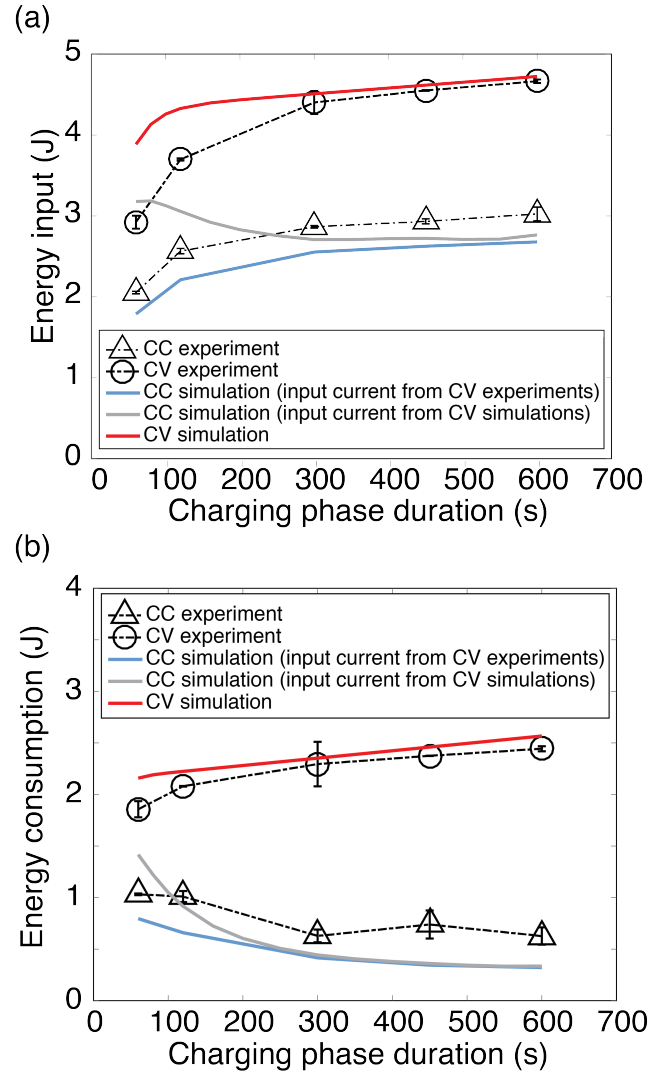
Figure 3.3: Comparison of (a) energy input and (b) energy consumption of a CDI cell in CV or CC mode versus charging phase durations of 1, 2, 5, 7.5 and 10 min. CV and CC modes were operated under the conditions of the same input electric charge and identical charging times. The dotdash line with circle markers represents experimental data for CV operation. The dotdash line with triangular markers represents CC experimental data. The shortdash line is simulation results for CV mode. Black and light gray solid lines are simulation data for CC mode using input current from CV experiments and simulation data for CC mode using input current from corresponding CV simulations.

3.4.3 Salt removal comparison

We compare salt removals of CC and CV experiments to investigate if there is a trade-off between energy consumption and salt adsorption capabilities. We calculate salt removed from real-time conductivity measurement of effluent stream. Fig. 3.4 shows experimentally measured energy consumption normalized by moles of salt removed as a function of charging phase duration. These data clearly demonstrate that CC consumes less energy per moles of salt removed than CV operation. At a charging duration of 10 min, CC mode consumes energy at 33.8 kJ per mole of ions removed, which is only 28% of CV mode energy consumption (120.6 kJ/mol). The inset figure compares the absolute salt adsorptions of CV and CC. Interestingly, CV and CC remove similar amounts of salts for all five charging phase durations (and so electric charge is here a good proxy for salt removal). These observations reinforce the conclusion that CC mode consumes significantly less energy than CV mode, while also achieving a similar level of salt adsorption.
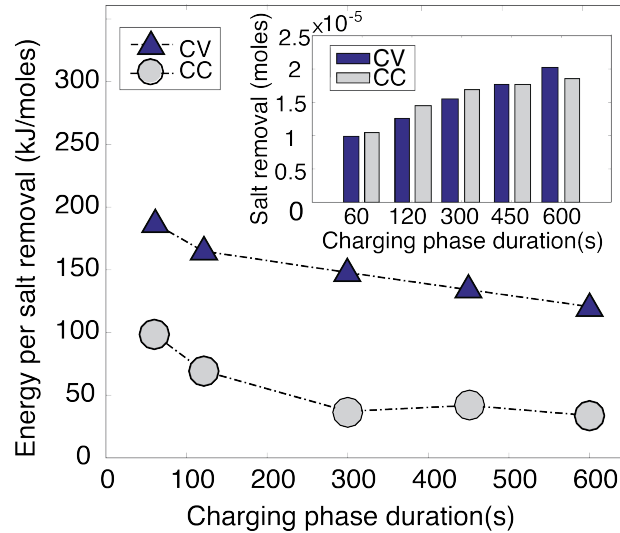
Figure 3.4: Energy consumption per mole of salt removal of CV and CC operations from experiments with charging phase durations of 1, 2, 5, 7.5 and 10 min. In the main figure, the dotdash line with blue triangular markers is energy per salt removal of CV operation, whereas the dotdash line with gray circle marker represents CC mode data. Inset figure compares the absolute amounts of salt adsorbed in CV and CC experiments, which indicates similar desalination performance of these two modes.

3.5   Conclusions

In this chapter, we present our studies on energy consumption of a CDI cell and compare the two most commonly used operation modes: constant voltage (CV) and constant current (CC). The comparison of energy consumption is conducted under the strictly enforced conditions that the CV and CC operations result in the same amounts of input (electric) charge and within identical charging timespans. We have developed a transmission-line based LTspice circuit model to capture electrical dynamics of CDI charging and investigate energy consumption mechanisms. We found that CC mode consumes much less energy than CV mode but achieves similar level of salt removals, and this is due to less resistive dissipation with CC. We focused on energy consumption during the charging process in order to accurately access salt removal and avoid salt contamination of the effluent stream caused by ion desorption at the beginning of a standard discharging step. Isolating charging and discharging steps enables precise evaluation of energy cost per unit of ions removed. We hypothesize that our major conclusion regarding energy consumption (that CC is more energy efficient than CV) applies to the discharging phase and to the entire charge/discharge cycle.

Lastly, we note that the CC operation possesses other advantages over CV apart from lower energy consumption, such as producing constant and adjustable effluent concentrations [38, 74, 87, 88], and limiting charging time spent at substantial oxidizing potentials [28]. Therefore, we advocate the use of CC mode over CV for CDI cell operations to achieve lower energy consumption as well as produce controllable desalted effluent.

Chapter 4

Charging and fluid flow dynamics of a flow-through CDI system

4.1   Introduction

The operations of CDI systems always require flow. Flow can be introduced intermittently between charging and discharging steps to generate desalted water and brine in batches. Most commonly, flow is maintained in the entire operation cycle as a steady water stream. The coupling of charging and fluid flow determines dynamics of deionization process, such as effluent salinity and water recovery ratio. Therefore, it is vital to understand and characterize the interplay of charging and fluid flow in a CDI cell to achieve optimal performance.

The coupling between charging and flow in a CDI cell is largely determined by its configuration. The most common CDI configuration is the flow-between architecture where the salt solution flows through a space between two porous carbon electrodes [28, 29, 31, 39, 71, 89, 90]. There has been a few reported studies of the interplay among charging time scales, fluid flow, and cell capacity for flow-between CDI. Zhao et al. showed that with constant current (CC) charging, the effluent salt concentration of a membrane CDI (MCDI) cell could be tuned to a desired set point by adjusting flow rate and charging current [31]. Biesheuvel et al. presented a dynamic adsorption/desorption process model based on the Gouy-Chapman-Stern EDLs structure to predict time-dependent effluent

concentrations of CDI experiments. Their model includes continuous flow but is limited to constant voltage (CV) charging and discharging [91]. Jande et al. developed a transient adsorption mathematical model to predict effluent concentration minima and charging time in CDI (in CV mode) using charging and flow parameters, such as applied potential, flow rate, and electrode capacity [92]. In subsequent study, Jande et al. presented a dynamic response model to describe the variation of the effluent concentration with time under CC charging [76]. However, none of these efforts have focused on identifying the governing parameters around charging time versus flow rate, and there are no clearly identified figures of merit and non-dimensional parameters governing this interplay.

The flow-between CDI exhibits transport limitations. Although easier to assemble and seal, this traditional architecture is significantly limited by spacer-to-electrode diffusion times and inability to utilize the full adsorption capability of porous electrodes [30]. In the current study, we primarily focus on an alternative flow-through architecture. In contrast to flow-between, flow-through CDI (ftCDI) [30, 70, 93] cells are configured to drive feed water directly through the electrodes (and minimize the gap between them). This enables fast ion transport through pores and full accessibility of the EDL capacitance of cell [30]. The interplay between charging dynamics and feed water flow rate is especially important for ftCDI, since advection plays a major role in ion transport to adsorption sites within the porous electrode volume.

The only study of system dynamics of ftCDI system is to our knowledge that of Suss et al. [91]. Suss et al. analyzed ftCDI operation in batch mode and with intermittent flow applied only during open (external) circuit phase between charging and discharging steps [30]. This batch mode may be easier to rationalize, but limits the throughput and fresh water production rate of the system.

Here, we focus primarily on understanding and characterizing the figures of merits associated in the interplay among charging time scales, fluid flow, and cell capacity, particularly in ftCDI. We present two models to describe the desalination performance of an ftCDI system with a focus on understanding and characterizing the coupling effects of charging and fluid flow for a given cell capacity. We primarily focus our study on CC mode as CC operation is more energy efficient than CV [93]. We first present the perhaps the simplest model which nevertheless captures essential dynamics: a zero-dimensional, unsteady lumped parameter model. We use this simple model to identify non-dimensional parameters and figures of merit associated with ftCDI temporal response.

We then present a numerical model based on area-averaged one-dimensional unsteady transport equations. This numerical model is based on a modified Donnan approach for capacitive ion charge storage [71, 83, 94, 95, 95, 96] and we consider a form applicable to capacitive deionization in porous electrodes including the effect of (immobile) native surface charge [97, 97, 98]. This second model is more comprehensive and captures both temporal fluctuations and variability along the direction of flow in an ftCDI cell. We validate modeling results by performing experiments with an ftCDI cell fabricated using hierarchical carbon aerogel monoliths (HCAMs) electrodes [30, 52, 82, 93], as shown in 4.1a. We use both models to identify two important salt transport regimes, and pose non-dimensional parameters applicable to describe and quantify these regimes. To the best of our knowledge, our work is the first comprehensive study centered on the coupling of charging and fluid flow dynamics in any type of CDI. Although we concentrate on ftCDI, we will briefly discuss differences between ftCDI, fbCDI and MCDI in terms of charging and flow interplay. Moreover, our models and analysis approach are potentially applicable to other electrochemical systems that involve charging and fluid flow dynamics, such as flow batteries and fuel cells.
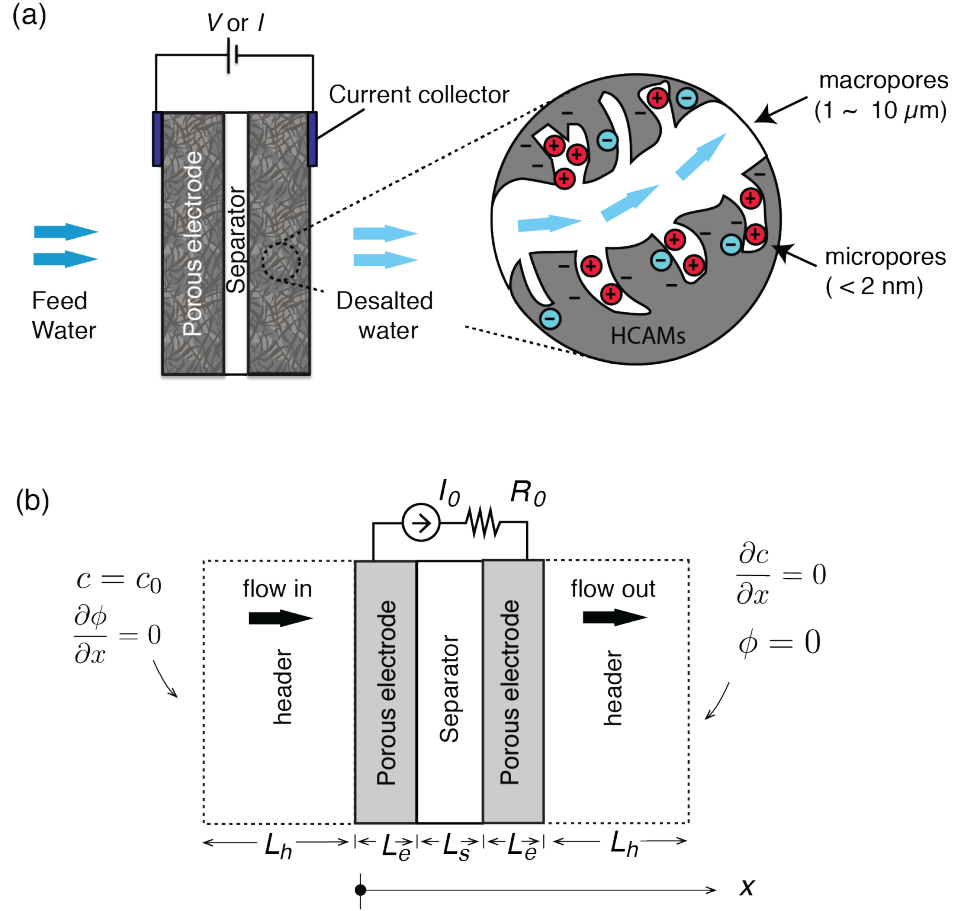
Figure 4.1: (a) Schematic of the flow-through CDI cell used in this study and the charging process inside porous electrode. The cell consists a pair of 300 μm thick hierarchical carbon aerogel monolith (HCAM) electrodes, an 80 μm porous dielectric separator, two metal current collectors and wires. The HCAM electrodes have a bimodal pore structure consisting of macropores (pore diameter 1-10 μm) and micropores (pore diameter <2 nm). During charging process, mobile ions from water (represented in red color) transported through macropores are electrostatically absorbed in micropores to compensate electrical charge (represented by negative sign) in carbon matrix. The carbon electrode surface also has immobile native charge (represented by blue ions) either introduced by surface group modification or electrochemical oxidation during operation. (b) Schematic of modeling domains and boundary conditions in one-dimensional numerical model. The length of separator is exaggerated for illustration (not reflecting the actual length used in simulations). For merely computation purpose, we include two artificial headers. The front header is to accommodate salt flux from upstream tubing and the rear header is needed for simulating concentration effluent properly.

4.2 Theory

4.2.1 Model I: Unsteady zero-dimensional lumped parameter model

In this section, we present a lumped-parameter transport model based on classical macroscopic porous electrode (MPE) theory [99] and a Gouy-Champan-Stern (GCS) treatment of charge layers [100] to predict time-dependent effluent concentration ce and identify performance metrics of an ftCDI cell. We start with the general form of MPE transport equation,

$$\frac{\partial(c_i)}{\partial t} + \nabla \cdot N_i = aj_{in} \tag{4.1}$$

Here, c_i is the volume-average concentration of ion species i in the pores. $\mathbf{N_i}$ is the average molar flux vector in liquid phase, including contributions from advection, diffusion, and electromigration. j_{in} is the molar flux averaged over the interfacial area between the electrode matrix and liquid phase. a is the specific interfacial area, defined as the surface area of the porous electrode per unit volume of the total electrode. We formulate transport equations within the porous electrode assuming bimodal pore structures, and implement the GCS model to describe the EDLs formation. We assume the electrode materials possess larger transport pathways consisting of continuous micron-scale pore networks (which are typically termed macropores which have order >50 nm pore diameters), and smaller nano-scale pores (termed micropores and which have order <2 nm pore diameters) as salt adsorption and desorption sources. We note that for HCAM materials, the primary transport pores have diameters >1 μm [52, 53]. The GCS model assumes two nanoscopic charge layers: the diffuse layer in which the ions are nonspecifically electroadsorbed within the double layer, and a compact layer of specifically absorbed ions which separates the diffuse layer from the electrode surface. We use $\Delta\phi_{diff}$ to represent voltage difference over the diffuse part of the double layer. To develop this model, we will consider an averaging of the transport equations along a cross-sectional area normal to the primary flow direction through electrodes. This area averaging results in a one-dimensional geometry along the superficial flow direction (along direction x in Fig. 4.1a), and introduces the effect of EDL electrostatic adsorption into the equations as a local sink/source term for ions. We assume uniform porosity throughout the electrodes, and a binary, symmetric, univalent and dilute electrolyte. The mass transport of ion species in macropores is thus formulated as

$$p_M \frac{\partial c}{\partial t} + u_{sup} \frac{\partial c}{\partial x} - p_M D_{BF} \frac{\partial^2 c}{\partial x^2} = -p_m \frac{\partial (a\Gamma)}{\partial t} \tag{4.2}$$

Here, c is the salt concentration (anion or cation) in the electroneutral macropores. Note that electroneutrality assumption applied within macropores enforces equal concentration of anions and cations for the transport problem. In the volume averaging of salt concentration c, the characteristic length scale is considerably larger than macropore topological features but small enough to capture spatiotemporal variation. p_M is the porosity associated with macropores (the volume fraction of the pores contributing to mass transport pathways), and p_m is the porosity associated with micropores (the volume fraction of pores contributing to ion adsorption). u_{sup} is the superficial velocity, a hypothetical flow velocity calculated as the actual volume flow rate divided by the macroscopic cross-sectional area. D_{BF} is here the one-dimensional Burnett-Frind hydrodynamic dispersion coefficient which approximates the effects of longitudinal dispersion of ion species due to both mechanical spreading and molecular diffusion in porous media. $D_{BF} = \alpha_L u_{sup} + D_{eff}$, where α_L is longitudinal dispersivity parameter and D_{eff} is effective molecular diffusivity which accounts for tortuosity effects. The right-hand side of equation 4.2 is a sink or source term from MPE theory for ion adsorption or desorption. This term links the local macropore ion transport to adsorption/desorption in micropores. a is the electrode surface area per unit volume of electrode matrix, and we assume a is a uniform number across the electrode. Γ is the salt adsorption in units of moles per electrode surface area. We also define the local charge density on the electrode surface (in unit of moles per area) as σ. A complete list of variables, parameters and constants used in lumped parameter model is presented in Table 4.1.

Next, we here define a local current efficiency λ, the local ratio of salt adsorption/desorption per unit of net electrical charge transferred ($\lambda = (d\Gamma/d\sigma)$). The use of λ links electrical charge in carbon matrix and salt adsorption in the pores. In GCS model, current efficiency relates to diffuse layer potentialas $\Delta\phi_{diff}$ as $\lambda = tanh(|\Delta\phi_{diff}|/(2V_T))$ where V_T is thermal voltage ($V_T = kT/e$, k and T being Boltzmann constant and temperature). We replace salt adsorption/desorption rate $\partial(a\Gamma)/\partial t$ by $\lambda\partial(a\sigma)/\partial t$. The transport equation becomes

Table 4.1: Variables and parameters used in lumped parameter model

variable	Description	units
c_e	effluent salt concentration	mM
Q	flow rate	mL/min
I_o	charging current	mA

parameter	Description	value	units
c_o	feed salt concentration	50	mM
p_M	Macropore porosity	0.57	
A_m	across-section area of electrode and separator	22.4	cm^2
L_e	thickness of electrode	300	μm
L_s	thickness of separator	80	μm
L	cell length, $L = 2L_e + L_s$	680	μm
V_0	entire cell volume, $V_0 = (2L_e + L_s)A_m$	0.67	cm^3
α_L	longitudinal dispersivity	10^{-4}	m
D_{eff}	effective molecular diffusion coefficient	6.65×10^{-10}	m^2/s
D_{BF}	Burnett-Frind hydrodynamic dispersion coefficient in electrodes	2.54×10^{-9}	m^2/s

$$p_M \frac{\partial c}{\partial t} + u_{sup} \frac{\partial c}{\partial x} - p_M D_{BF} \frac{\partial^2 c}{\partial x^2} = -p_m \lambda \frac{\partial (a\sigma)}{\partial t} \tag{4.3}$$

To simply the model to zero-dimensional, we perform volume integration of Equation 4.3 across the entire ftCDI cell. To do this, we assume a uniform current efficiency across the entire electrode and define a cell average concentration as $p_M V_0 \frac{\partial \bar{c}}{\partial t} \approx \int p_M \frac{\partial c}{\partial t}$. We then apply divergence theorem and approximate inlet and outlet boundary conditions as at $x = 0$ and at $x = 2L_e + L_s$. We arrive at a zero-dimensional (in space) ODE for c_e, as shown in Equation 4.4.

$$\frac{\partial c_e}{\partial t} + \frac{2}{p_M V_0}(Q + \frac{p_M A_m D_{BF}}{L_s + 2L_e})(c_e - c_o) = -\frac{\lambda I_o}{F} \tag{4.4}$$

The terms on the left-hand side of this equation correspond to respectively accumulation within the cell and the net transport due to advection and dispersion. The right-hand side is the sink/source term associated with electrostatic adsorption.

4.2.2   Lumped current efficiency formulation

We adopt the classical GSC model to treat electrical double layers to formulate a lumped current efficiency. In the classical GCS model, the concentration of ion i in diffuse layer follows a Boltzman distribution,

$$c_i = c_\infty exp(-\frac{z_i \phi}{V_T}) \tag{4.5}$$

where c_∞ is the ion concentration in bulk solution (or in macropore in our bimodal pore structures), and ϕ is the potential within the diffuse double layer relative to the local solution outside the double layer. z_i is the ion valence. In our simple lumped parameter model, we will assume the macropore concentration is the same as feed concentration c_o. Here we will make a typically Donnan type model assumption [31, 71, 83, 89, 94, 94, 97] where we assume that the potential and ion concentration c_i within micropores is a single uniform value which we will term $\Delta\phi_{diff}$. Hence, the ion concentrations within the micropore are

$$c_+ = c_o exp(-\frac{\Delta\phi_{diff}}{V_T}), c_- = c_o exp(\frac{\Delta\phi_{diff}}{V_T}) \qquad (4.6)$$

Hence, the total ion accumulation of net ionic charge within an electrode of macroscopic volume V_e ((equal to $\pm I_o$ in CC charging) is then,

$$\pm I_o t = \mp p_m V_e F c_o [exp(-\frac{\Delta\phi_{diff}}{V_T}) - exp(\frac{\Delta\phi_{diff}}{V_T})] \qquad (4.7)$$

We can now consider a lumped form of charge efficiency λ to formulate a form of Equation 4.4 applicable to the entire cell. To this end, we identify and explore two regimes for λ: (1) $\lambda <1$; (2) $\lambda = 1$. These regimes are respectively early, low voltage phase and longer-term, significant voltage phase.

We first describe the early phase of charging. In this phase, we assume the argument of the hyperbolic tangent is smaller than unity so we approximate $tanh(|\Delta\phi_{diff}/(2V_T)|)$ as $|\Delta\phi_{diff}/(2V_T)|$. Further, within the range of $0 \leq (\Delta\phi_{diff}/V_T) \leq 2$, we linearize $exp(\Delta\phi_{diff}/V_T)$ in Eq. 4.7 as $1 + 2(\phi_{diff}/V_T)$. We then arrive at an approximation of $\Delta\phi_{diff}$ using c_o, p_m, charging current I_o, and electrode volume V_e as,

$$\Delta\phi_{diff} = \frac{I_o t}{4 p_m V_e c_o F} \qquad (4.8)$$

Substituting Equation 4.8 into the approximate form λ. We obtain the lumped current efficiency λ as:

$$\lambda = \frac{|\Delta\phi_{diff}|}{2V_T} \approx \frac{I_o t}{8 p_m V_e c_o F^2} \qquad (4.9)$$

We plot this estimate lumped current efficiency (which is proportional to time) in the inset in Figure 4.2 (the constant slope shown with a dashed line).

At longer charging times (and potentials $\Delta\phi_{diff}$ greater about about twice the thermal voltage), the current efficiency $tanh(|\Delta\phi_{diff}|/(2V_T))$ approaches unity. Hence, the sink term in Equation (4) reaches a constant value of $-(2I_o/(p_M V_0 F))$, and this reflects a constant rate of salt accumulation directly proportional to applied current.

Hence, we can write two versions of Equation 4.4 for the two regimes of lumped charge efficiency as follows:

$$
\begin{cases}
\dfrac{\partial c_e}{\partial t} + \dfrac{2}{p_M V_0}\left(Q + \dfrac{p_M A_m D_{BF}}{L_s + 2L_e}\right)(c_e - c_o) = -\dfrac{I_o^2}{4 p_M p_m V_0 V_e c_o F^2} \ (\lambda < 1) & \text{(4.10)} \\[4mm]
\dfrac{\partial c_e}{\partial t} + \dfrac{2}{p_M V_0}\left(Q + \dfrac{p_M A_m D_{BF}}{L_s + 2L_e}\right)(c_e - c_o) = -\dfrac{2 I_o}{p_M V_0 F} \ (\lambda = 1) & \text{(4.11)}
\end{cases}
$$

4.2.3 Identification of transport regimes

We now identify salt transport regimes by revisiting original transport equation (Equation 4.3) and performing normalization. In Equation 4.3, concentration c is nondimensionalized by feed concentration c_o as $c^* = c/c_o$, time is normalized by the advection time scale of water flowing through the cell length L as $t^* = t/(L/u_{sup})$, and local charge density $\alpha\sigma$ (in unit of moles per electrode volume) is normalized by feed ion concentrations as $(\alpha\sigma)^* = (\alpha\sigma)/c_o$. The dimensionless form of Equation 4.3 is

$$
\frac{\partial c^*}{\partial t^*} + \frac{1}{p_M}\frac{\partial c^*}{\partial x^*} - \frac{D_{BF}}{u_{sup}}\frac{\partial^2 c^*}{\partial x^{*2}} = -\frac{p_m}{p_M}\lambda\frac{\partial(a\sigma)^*}{\partial t^*}
\tag{4.12}
$$

We define a dimensionless Peclet-type number as $Pe^* = \frac{u_{sup}L}{p_M D_{BF}}$ to compare the competition of advection and dispersion (not just molecular diffusion) in mass transport. Depending on the value of Pe^*, we perform our theoretical analysis and experiments of ftCDI performance in two transport regimes: (1) advection-dominated ($Pe^* \gg 1$) and (2) dispersion-dominated ($Pe^* \ll 1$) regimes. In regime (1), we can safely neglect the dispersion term in Equation (3) as much smaller than advection. In a similar manner, we can neglect the advection term in regime (2).

4.2.4 Solutions to unsteady zero-dimensional lumped parameter model

We present analytical solutions of ODEs in Equation 4.10 for both the advection and dispersion limited regimes respectively. We present predictions based on this model in RESULTS AND DIS-CUSSION. The caution that this lumped-parameter model has only limited applicability to the dispersion dominated regime ($Pe^* < 1$). Dispersion and diffusion limited cells experience a global starvation condition where advective transport is insufficient to replenish ions for electroadsorption,

and the resulting strong ion depletion within the electrode strongly violates the assumption that the macropore concentration is constant and uniform at an approximate value of c_0.

Although simple, this lumped-parameter model clearly identifies a characteristic time scale for charging efficiency as $t_\lambda = 8p_M V_e c_o F/I_o$, which is the characteristic time required for the charging process to approximately achieve a current efficiency of unity, as shown in the inset of Figure 2 (dashed line). We will therefore normalize charging time as $\bar{t} = t/t_\lambda$ in both the lumped parameter and the numerical models. From this model, we also identify a characteristic quasi-steady-state condition wherein advective influx of salt is balanced by a constant electroadsorption rate (with approximate charge efficiency of unit). We can derive this characteristic steady effluent concentration c_e under CC operation by setting $(\partial c_e/\partial t) = 0$ and $\lambda = 1$ in Equation 4.4,

$$(c_e - c_o) = \frac{I_o}{F(Q + \frac{p_M A_m D_{BF}}{L_s + 2L_e})} \tag{4.13}$$

In the advection-dominated regime, this concentration difference $c_e - c_o$ further simplifies to $c_e - c_o = I/(FQ)$. Hence, in both the lumped parameter model and in the numerical model we will normalize the effluent concentration as $\overline{(c_e - c_o)}/(I/(FQ))$.

4.2.5 Model II: Distributed-parameter numerical model using modified Donnan (mD) model with native charge

In this section, we present a more comprehensive numerical model which captures both temporal fluctuations and variability along the flow direction of an ftCDI cell. We adopt mD treatment of EDLs in bimodal pore structure electrodes. We include a formulation for immobile native charge in the micropores to account for non-electrostatic adsorption. We will use this model to both benchmark the simpler model of the previous section, and further study charging dynamics. We will also compare both models with experimental results (see RESULTS AND DISCUSSION in this chapter).

For the numerical model, we again consider a one-dimensional area-averaging approach and the similar assumptions regarding the electrolyte solution (binary, symmetric, univalent, and dilute) as the lumped-parameter model. The complete mass transport of ion species i in macropores is then

$$p_M \frac{\partial(c_{M,i})}{\partial t} + \nabla \cdot [c_{M,i}u_{sup} - p_M D_{BF,i}\nabla c_{M,i} - \frac{p_M}{\tau}\mu_i c_{M,i}\nabla \phi] = -p_m \frac{\partial(c_{m,i})}{\partial t}, \tag{4.14}$$

where τ is tortuosity of electrode material and ϕ is the potential of local macropore liquid phase. Other variables and parameters share the same definitions as those used in lumped-parameter model. We again assume electroneutrality holds within macropores and thus $c = c_{M,i}$ for $i = \pm 1$. Again, we assume the same Burnett-Frind dispersion coefficient and the same mobility for both ion species, so that $D_{BF} = D_{BF,i}$ and $\mu = \pm\mu_i$ for $i = \pm 1$.

By adding and subtracting Equation 4.14 for anions and cations, we derive the governing equations for mass transport and charge balance in macropores

$$p_M \frac{\partial c}{\partial t} + u_{sup}\frac{\partial c}{\partial x} - p_M D_{BF}\frac{\partial^2 c}{\partial x^2} = -p_m \frac{\partial w}{\partial t} \tag{4.15}$$

$$\frac{p_M}{\tau}\mu \frac{\partial}{\partial x}(c\frac{\partial \phi}{\partial x}) = p_m \frac{\partial q}{\partial t} \tag{4.16}$$

Here, w is half of the volumetric salt concentration in micropores, defined as $2w = c_m^+ + c_m^-$ where c_m^+ is cation concentration and c_m^- is anion concentration in micropores. q is the half of net charge density in micropore as q ($2q = c_m^+ - c_m^-$, with unit of moles per volume). We note here that Equation 4.15 is very similar to the transport equation in lumped-parameter model (Equation 4.2) but with a different salt adsorption/desorption term on the right-hand side.

$$2q + q_{native} + q_e = 0 \tag{4.17}$$

Here q_{native} is volumetric charge density of immobile native charge on electrode surface, in unit of moles per volume. For carbon electrodes, the native charge may be introduced, for example, during the material synthesis process or during CDI operation by electrochemical oxidation of carbon. q_e is the electronic charge density in the carbon.

Next, we relate electronic charge q_e to the micropore potential drop $\Delta\phi_m$ (potential difference between electrode surface and the center of micropore) as:

$$\Delta\phi_m = q_e \frac{F}{C_m} \tag{4.18}$$

Here F is the Faraday constant. C_m is defined as the effective volume-specific capacitance of micropores, which we call micropore capacitance [71]. In addition, $\Delta\phi_m$ and Donnan potential $\Delta\phi_D$ are related to the potential difference between the electrode phase ϕ_e and the local macropore liquid phase ϕ as

$$\Delta\phi_m + \Delta\phi_D + \phi = \phi_e \tag{4.19}$$

Lastly, we close the system of equations by introducing a charge conservation relation between external constant current source I_o and accumulative electronic charge q_e.

$$I_{ext} = p_m \int \frac{\partial(q_e F)}{\partial t} dV \tag{4.20}$$

We note here that we have presented a set of equations which model transport and charging dynamics of ftCDI systems under CC operation. These equations can be modified to apply to CV operation.

We performed parameter extraction to obtain the values of key fitting parameters in the model. The extraction process is discussed in RESULTS AND DISCUSSION. A summary of the variables and parameters used in distributed parameter model is listed in Table 1.2. All numerical simulations were performed with a commercially available finite element simulation software (COMSOL Multiphysics, 5.1, Burlington, USA).

4.3   Experimental methods

We performed experiments to study the coupling of charging and fluid flow and to validate our ftCDI models. We also use these experiments to demonstrate the applicability of the dimensionless parameters identified by the lumped-parameter model to scale and rationalize ftCDI dynamics. We particularly focus on the intimate interplay and competition among flow rate, charge accumulation rate, and charge efficiency.

Flow-through CDI cell

We fabricated a flow-through CDI (ftCDI) cell to validate model predictions and study charging dynamics. The ftCDI cell was made of two blocks of hierarchical carbon aerogel monoliths (HCAMs) material [30, 52, 82, 83] with area of 4 x 6 cm and thickness of 300 μm. We used an 80 μm porous paper filter as a separator to insulate between the two electrodes. We used silver epoxy to create intimate electrical contacts between HCAM electrodes and copper wires [70]. The two porous electrodes and a separator were stacked into an assembly and glued on to a polycarbonate frame using epoxy. This assembly was then sandwiched between two 6 x 7.5 cm polycarbonate endplates with 400 μm silicone rubber sheets as gaskets. Both endplates were milled to accommodate two tubulations: one as a port to flow water, and the other one as a port to release trapped air. The cell was assembled using ten bolts. The cell assembly frame and housing parts were fabricated from polycarbonate.

Experiment procedures

We performed continuous flow CDI experiments using our ftCDI cell with 50 mM NaCl. We adopted a CC charging scheme as our previous study shows CC charging mode is much more energy efficient than CV operation (for equal charge and time of charging). We used a Biologic SP-300 potentiostat (Bio Logic Science Claix, France) to supply current and monitor electrical responses. A flow-through conductivity sensor (Edaq, Denistone East, Australia) was attached to the CDI cell downstream to measure the conductivity of effluent solution. A homemade flow-through thermal sensor was used to monitor effluent solution temperature. We used a peristaltic pump (Watson Marlow 120U/DV, Falmouth, Cornwall, UK) to flow feed solution through the cell at various flow rates and with closed-loop circulation (flow from solution container to ftCDI cell and back to container). We continuously purged feed solution with house nitrogen to remove dissolved oxygen. Before experiments, we flowed sodium chloride solutions through the cell without charging for 30 min at 2.4 mL/min to allow the cell to equilibrate with solutions.

We first performed CC charging experiments at 50 mA with flow rates at 2.5, 5.1, 7.7, 10.3 and 12.8 mL/min to demonstrate CDI charging and flow dynamics in advection dominated regime. We calculate the Peclet-type parameter of fluid flow in this regime as 8.8 to 11. To rapidly regenerate

the cell after charging (for convenience and expediency), we discharged the cell in CV mode at zero voltage. To operate CDI cell in the diffusion dominated regime, we charged the cell with 50 mA constant current at flow rates of 0.03, 0.10 and 0.22 mL/min, and followed by CV discharge. In this operational regime, the Peclet-type number is smaller or on the order of unity. For each experiment, we repeated charging and discharging cycles five times and used the data from last three cycles for model validation.

4.4 Results and discussion

4.4.1 Parameter extraction

There is one fitting parameter in lumped-parameter and an additional three fitting parameters used for the numerical model. These four parameters are dynamic microporosity p_m, micropore capacitance C_m, native charge density q_{native} and longitudinal dispersivity α_L. To extract these values, we first fitted the experimentally measured near-equilibrium salt adsorption and charge storage of our cell under CV operations to a CV numerical model. We obtained the fitted values of C_m, q_{native}, and and list these values in Table 4.2. We then fitted the experimental outlet effluent concentrations under CC mode to the CC numerical model (as described in section 4.2) to obtain values of dynamic microporosity p_m and dispersivity , also shown in Table 4.2. We note here that three values of the fitted parameters are similar to those reported in literature for porous carbon materials (see for example Gao et al reported Cm as 135 F/cm^3 and immobile native charge as 200 mM [98]; Suss et al. reported Cm as 130 F/cm^3 [83]; and Hemmatifar et al. have fitting values for Cm and pm as 150 F/cm^3 and 0.3 respectively [101]).

In Figure 2a we show results for the effluent salt concentration for the ftCDI as a function of time for both the lumped-parameter and numerical models. The lumped-parameter model captures many of the qualitative features of the numerical model. This includes an initial rapid drop in effluent concentration, and the subsequent approximate leveling off of the effluent concentration observed in the quasi-steady-state operation described earlier (wherein unity charge efficiency results in an approximately constant adsorption rate). The inlet-to-outlet reduction in effluent salt concentration in this quasi-steady operation is proportional to applied current as suggested by the lumped-parameter

Table 4.2: Variables and parameters used in numerical parameter model

variable	Description	units
c	local salt concentration	mM
q	net charge density in micropore	mM
q_e	electronic charge density in the electrode matrix	mM
w	electronic charge density in the electrode matrix	mM
ϕ	potential of local macropore liquid phase	V
ϕ_e	potential of electrode solid phase	V
$\Delta\phi_D$	Donnan potential	V
$\Delta\phi_m$	micropore potential drop	V

parameter	Description	value	units
p_m	micropore porosity	0.1	
C_m	effective volume-specific capacitance of micropores	120	F/cm^3
q_{native}	immobile native charge density	100	moles/m^3
τ	tortuosity of electrodes	2.4	
R_c	contact resistance	1.1	Ω
$D_{BF,s}$	Burnett-Frind hydrodynamic dispersion coefficient in separator	2.54×10^{-9}	m^3/s

(We list here only the additional parameters which are not already included in lumped-parameter model list of Table 4.1)

model (c.f. Equation 4.13). We see also that the lumped parameter model levels off at a time scale faster than the numerical model, which we attribute to the effect of non-uniform charging of the electrode predicted by the numerical model.

4.4.2 Advection-limited regime

As we mentioned in the THEORY seciton, we divide our ftCDI cell operations and theoretical analysis into two distinct transport regimes, depending on the values of our dimensionless Peclet-type number, Pe^*. In advection-limited regime, we study cell dynamics with flow rates ranging from 2.5 to 12.8 mL/min. The respective values of are between 8.8 and 11. From the lumped-parameter model, we identified two dimensionless parameters associated with this regime. We here propose that the proper characteristic time scale for scaling time in this advection dominated

regime is a charge efficiency timescale, characterized by $t_\lambda = 8p_M V_e c_o F/I_o$. Similarly, the scaling of effluent concentration in advection dominated operation should be in terms of the difference $(c_e - c_o)$ normalized by the quasi-steady (i.e., unity charge efficiency) electroadsorption rate $I/(FQ)$.

In Figure 4.2a, the solid lines represent effluent concentration profiles predicted by the lumped-parameter model. Dotted lines are simulation results from numerical model. Both models predict a gradual reduction of effluent concentration at the early stage of charging, followed by an approximate leveling off at quasi-steady state. The discrepancy between lumped-parameter model and numerical model is caused by nonuniformity of charging across electrodes, and this spatial nonuniformity is only captured by numerical model.

The markers in Figure 4.2a represent experimental data obtained in CC mode with 50 mA charging current. For an ftCDI cell, the concentration of effluent streams evaluates its salt removal performance. As predicted by simulations, in the beginning of deionization process, the salt adsorption is limited by current efficiency irrespective of a steady and strong transport of salt into the cell via advective mass transport. However, as the cell charges the non-linearity of the Boltzmann distribution of trapped salt in the micropores (c.f. Equation 4.7 exponents, nonlinear term) imply that new electrical charge more efficiently traps salt. As charge efficiency approaches unity, then a constant applied current Io implies a constant electroadsorption rate. In this quasi-steady operation, the reduction in salt concentration scales by with the ratio of I_o to flow rate Q. Comparing simulation results to experimental data, both lumped parameter model and numerical model demonstrate fair agreement with experiments, showing that our models at least capture the qualitative dynamics, as well as the approximate time scales and effluent concentration magnitudes of advection dominated ftCDI cell operation. We note that in simulations, models predict that effluent concentration will stay at a constant value in quasi-steady state until the cell voltage reaches operation limit (~ 1.2 V). However, in experiments effluent concentrations stay at quasi-steady state for a short period time and then gradually increase towards inlet concentration. This transition usually occurs around 150 s when the cell voltage reaches 0.7 V. We attribute this discrepancy between simulations and experimental results to charge loss caused by parasitic reactions on electrodes. Parasitic reactions provide current leakage paths, and therefore lower the current efficiency for salt adsorption, and this charge loss mechanism is not captured in simulation models.

These trends and limiting parameters suggest the normalization we show in Figure 4.2b. Here we leverage the scaling suggested by the lumped-parameter model to normalize the predictions of both models as well as the experimental data. Shown therefore are normalized effluent difference $\overline{(c_e - c_o)}$ versus normalized time $\bar{t} = t/t_\lambda$. First, the collapse of $\overline{(c_e - c_o)}$ vs. $\bar{t}$ curves is expected for the lumped-parameter model given the formulation and assumptions. Second, we see that this scaling suggested by the lumped-parameter model very well collapses the curves of the numerical model. We see all curves collapse into a tight group, with the exception perhaps of the numerical prediction for lowest flow rate where we observe in the numerical model the most non-uniform charging distributions. Third, and most importantly, we see that the scaling suggested by the lumped-parameter model well collapses all of the experimental data into a reasonably tight group. Further, we see the experimental data maximizes at about a value of unity, a result of near unity charge efficiencies observed for these data. Fourth, the most important discrepancy is the experimental observations of gradual increase of effluent concentrations in quasi-steady state. We attribute this discrepancy to charge consumption by parasitic reactions.
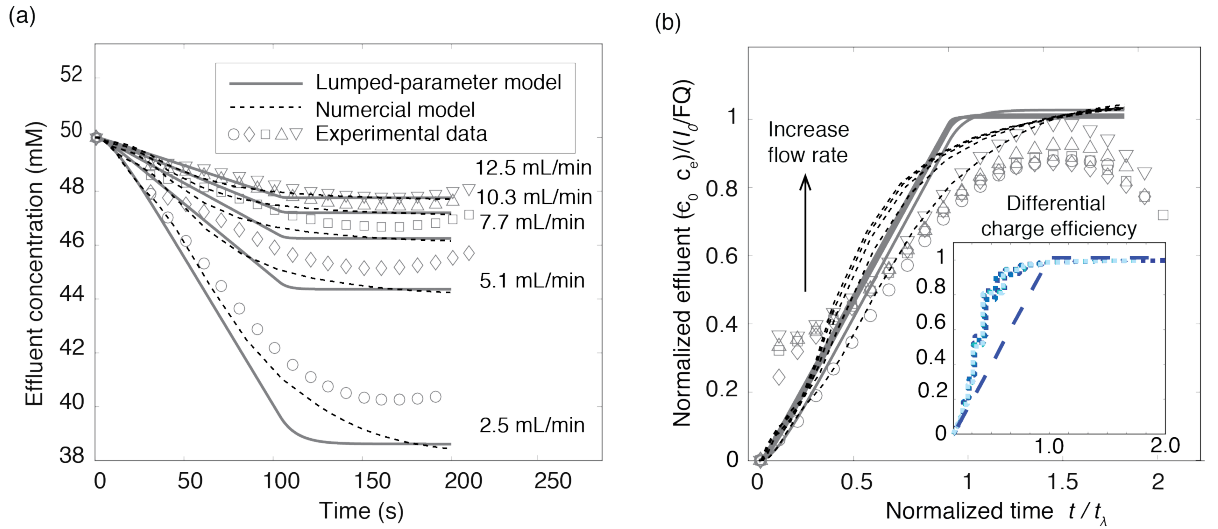
Figure 4.2: (a) Original and (b) normalized effluent concentration profiles from experiments (markers), lumped-parameter model simulations (solid grayscale lines) and distributed-parameter model simulations (short-dotted grayscale lines) in advection-dominated regime, with flow rates at 2.5, 5.1, 7.7, 10.3 and 12.8 mL/min. The ftCDI cell is operated in constant current charging mode at 50 mA.

4.4.3   Dispersion-limited regime

We performed simulations with lumped-parameter model and numerical model in dispersion-limited regime. The flow rates we used in this regime are 0.03, 0.10 and 0.22 mL/min, corresponding to Pe^* of 0.2, 0.7 and 1.3. We also performed deionization experiments to approximate this regime evaluate the performance of the models. The results and comparison are shown in Figure 4.3. We note the lowest flow rate we could explore was limited by the resolution of our peristaltic pump.

In the dispersion-limited regime, flow rates have minimal influence on effluent stream profiles. Instead, the effluent concentration is determined by interplay among the cell volume (and associated initial amount of salt contained within the electrode), the rate at which diffusion and dispersion can supply new salt, and the applied current. In Figure 4.3, we see that data for all three flow rates clustered along a parabolic-exponential shape curve, as predicted by lumped-parameter model. Prior to the cell voltage reaching the maximum threshold value of 1.2 V in charging, the desalination process is limited by both current efficiency and mass transport. The appropriate time scale in this regime is dispersion time scale which is the time that ion species (sodium and chloride) diffuse the distance of an electrode thickness, $t_{diff} = Le^2/D_{eff}$. The appropriate concentration normalization scale is the cell initial concentration c_o. Figure 4.3 shows the normalized simulation results from two models and normalized experimental data in this regime. The numerical model successfully predicts the experimental effluent streams. In contrast, the simulation results from lumped-parameter model deviate strongly from experimental data. Such a deviation is expected and is a result of the breakdown of the models assumptions. Recall that the lumped-parameter charge efficiency assumes that the salt concentrations in the macropore remains close to feed water concentration. However, this assumption is no longer valid in a mass-transport-starved, diffusion-limited regime which results in significant ion depletion within pores.

We note that the dispersion-limited regime is mostly of only academic interest in that it helps to identify a limiting behavior of operational regimes in a CDI system. In realistic operation of a ftCDI cell, dispersion-limited regime with continuous flow would likely imply overly low water throughput. The dispersion-limited regime may also be useful in analyzing limiting behaviors of batch mode operation, wherein charging occurs at stopped flow conditions between intermittent flow operation.

4.4.4 Discussion for performance optimization

Flow-through CDI has unique operation regimes comparing to other CDI architectures. Unlike traditional flow-between CDI whose desalination rate is primarily depending on ions diffusing from separator to electrode pores, ftCDI enables salt adsorption in advection-dominated regime, and has the flexibility to produce salinity controllable effluent streams with CC mode. An ftCDI cell operating in advection regime utilizes the full adsorption capability of porous electrodes, and therefore can achieve faster desalination rates. As we shown in Figure 4.2 and Figure 4.3, the interplay of charge accumulation rate, current efficiency and mass transport determines the desalination performance of an ftCDI cell. The low current efficiency at the early stage of electroadsorption process poses a limitation on salt removal and water recovery (the volume ratio of collected desalted water over feed water). To overcome this challenge, we can charge and discharge the cell within a voltage window where the lowest potential is still above the voltage threshold to achieve unity current efficiency. We also note that, as reported in literature, membrane CDI do not demonstrate the current efficiency limitation at the beginning of charging process, and this is because ion exchange membranes significantly enhance current efficiency and making it independent of EDL structure.
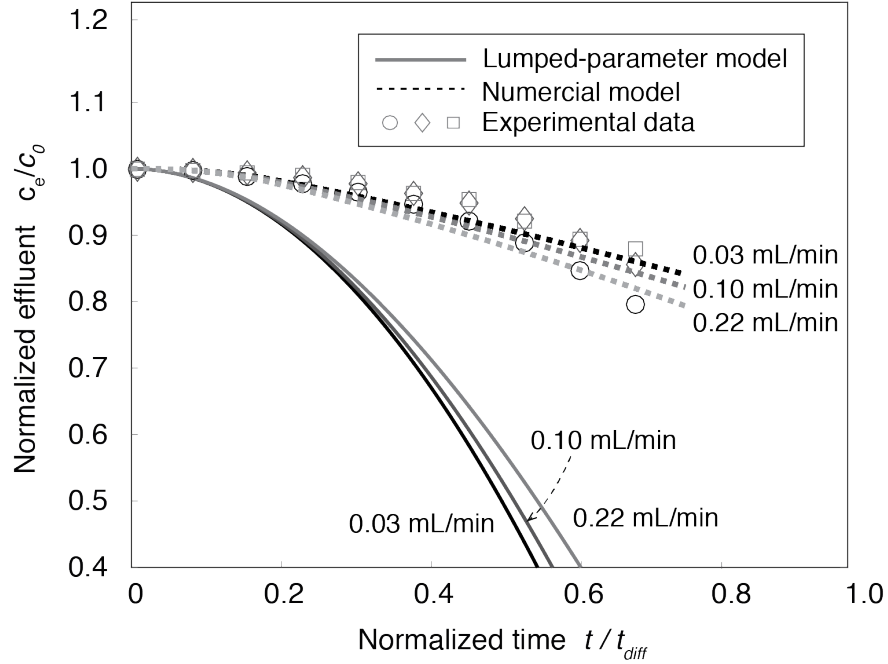
Figure 4.3: Normalized effluent concentration profiles (normalized by feed concentration c_0) from experiments (markers), lumped-parameter model simulations (solid grayscale lines) and distributed-parameter model simulations (short-dotted grayscale lines) in diffusion-dominated regime, with flow rates at 0.03, 0.10 and 0.22 mL/min. The ftCDI cell is operated in constant current charging mode at 50 mA.

4.5   Conclusions

We here report our studies on understanding and characterizing the coupling effects of charging and fluid flow in flow-through capacitive deionization systems. We have developed two transport and electro- adsorption/desorption models based on classical macroscopic electrode theory and electrical double layer models. The first model is a simplified, zero-dimensional lumped-parameter model. We have used this simple model to identify non-dimensional parameters and figures of merits associated with cell performance in two salt transport regimes: 1) advection-dominated regime and 2) dispersion dominated regime. For each transport regime, we have identified a pair of dimensionless parameters to characterize charging and fluid flow dynamics with CC charging mode. Our second model is a numerical model, which is based on a modified Donnan approach and immobile (native) surface

charge theory for electro- adsorption/desorption in porous electrodes. The second model captures both temporal and spatial responses of an ftCDI cell during charging process. We validated modeling results by performing experiments with an ftCDI cell operated with CC charging mode at eight different flowing rates (distributed in two transport regimes). We have shown that, in advection-dominated regime, current efficiency determines the salt adsorption at the early stage of deionization process. When current efficiency stabilizes, the salt removal is then limited by the ratio of charge accumulation rate and mass transport rate. In diffusion-dominated regime, both current efficiency and diffusion are critical for salt adsorption/desorption dynamics, whereas flow has nearly no impact on deionization outcome. In both regimes, the interplay between current efficiency, charging current and mass transport rate governs salt removal in flow-through CDI. Our study provides guidance for designing and optimizing operation procedures to further improve desalination performance and water recovery for ftCDI systems.

Chapter 5

Towards a multi-stage phased charging CDI system

5.1 Introduction

A single-stage CDI cell achieves limited salinity reduction in a single pass operation. Traditional flow-between CDI devices are typically capable to reduce feed water salinity by 5-20 mM (0.3-1.2 g/L). Our ftCDI cells have demonstrated enhanced salt removal of up to 70-100 mM (4.2-5 g/L) in a single pass, due to its more effective utilization of electrode capacity. However, this single-pass salinity reduction is still not sufficient for treating moderate or high salinity brackish water.

A potential method to improve salt removal in a single pass operate is to build a multi-stage system and desalinate feed water stage-by-stage in a subsequently phased charging scheme. As shown in Figure 5.1, in step 1, a volume of feed water is transported in cell 1 and deionized partially. This water volume is subsequently transported to cell 2 and cell 3 to perform second stage and third stage deionization. After three-stage of treatment, the salinity reduction of a single pass is tripled.

In this chapter, we demonstrate our efforts on building and modeling a multi-stage ftCDI system and present our preliminary results on multi-stage deionization operation with phased charging scheme. We extend our high-fidelity one dimensional numerical model to a multi-stage configuration. We present our fabrication efforts of two-stage and three-stage ftCDI cells and show the experimental

and simulation results of multi-stage operation in both phased and in-phase charging schemes.
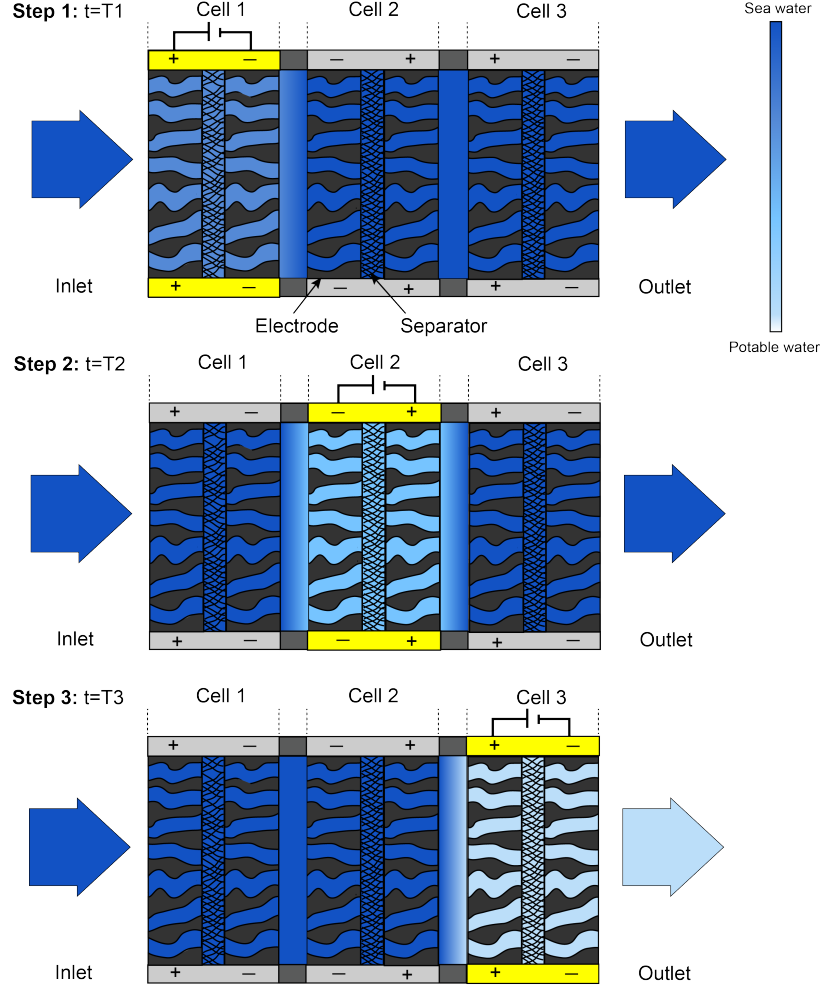
Figure 5.1: Schematic of a three-stage ftCDI system operated in three-step phased-charging scheme to achieve improved salinity reduction.

5.2 Multi-stage CDI model

We utilize the high-fidelity one-dimensional numerical model which we described in Chapter 4 as our base model. We extend this model to a two-stage cell configuration, as shown in Figure 5.2, two ftCDI cells are separated by a gap. The modeling domain in the gap shares the same governing equations as those used in separator domains. The only difference is that porosity is unity in gap region versus a fractional number in separators. We implemented our two-stage ftCDI modeling using a

commercially available finite element simulation software (COMSOL Multiphysics, 5.1, Burlington, USA). Our model has the capability of adjusting cell geometry and gap distance between cells, individually control charging currents of cell1 and cell2 and performing in-phase and phased charging and discharging for several cycles. We note here in-phase operation refers to charging/discharging cell1 and cell2 simultaneously. Our model can be easily further extended to three-stage or even more stages.
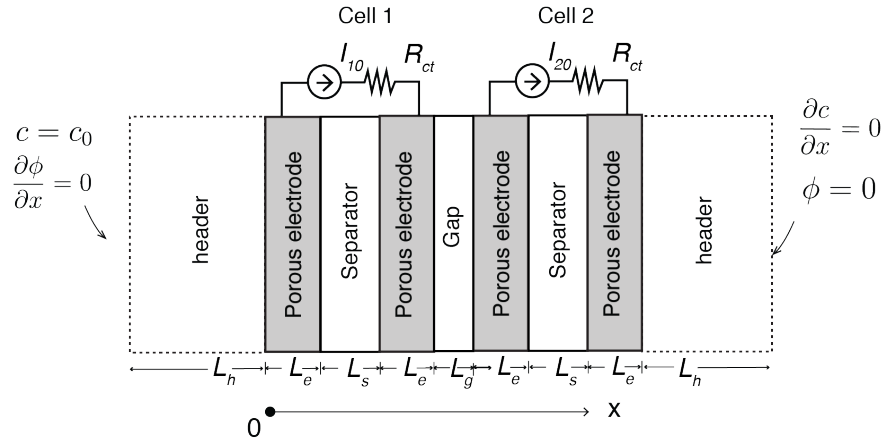
Figure 5.2: Schematic of modeling domains and boundary conditions in two-stage ftCDI numerical model. The length of separator is exaggerated for illustration (not reflecting the actual length used in simulations).

5.3   Cell design and fabrication

We have designed and fabricated two-stage and three-stage ftCDI cells using different sealing and assembly techniques. Figure 5.3 shows a two-pair four-electrode ftCDI cell. The HCAM electrodes used in this cell have a size of 2 cm x 2 cm x 300 μm. Four electrodes sandwich three 80 μm porous dielectric membranes. The electrode-separator assembly was glued to a center piece frame using thermally cured two-component epoxy(Stycast 2850). We iterated gluing process a couple of times and performed leak tests to ensure no potential water leakage path between electrodes and the frame. Finally, the electrode assembly was sealed by o-rings with two acrylic end plates and four bolts. This electrode and separator stacking technique has the advantage of minimizing gap space

between electrode pairs. However, the disadvantage is that the electrodes are difficult to take apart after glued together. Therefore, it is almost impossible to replace a broken or cracked electrode from this assembly.
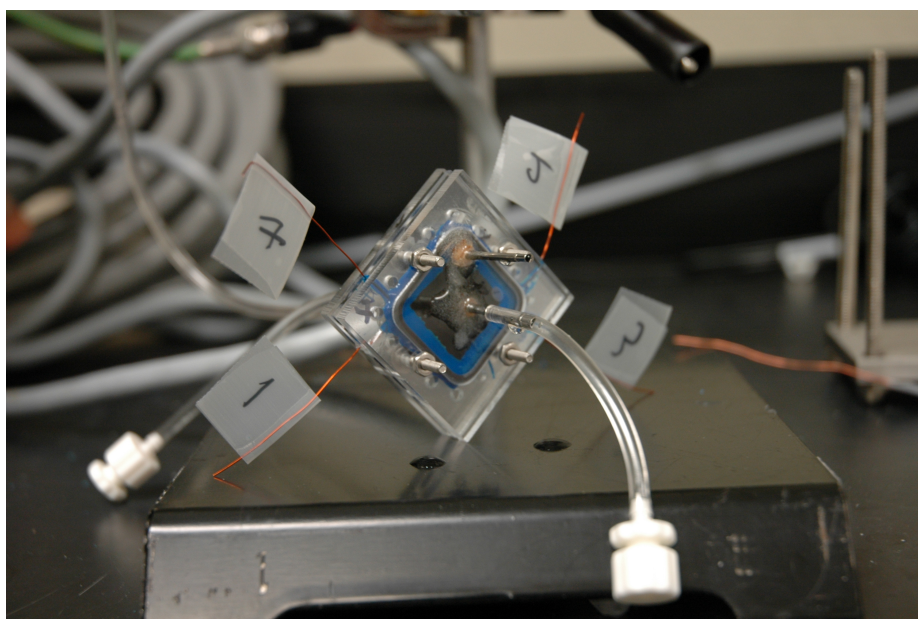
Figure 5.3: Image of a two-stage ftCDI cell made of stacking four HCAM electrodes and three dielectric separators.

Figure 5.4 shows a three-stage ftCDI cell fabricated by an alternative assembly technique. In this three-stage cell, each electrode pair and a separator are glued to a holder frame as a modulus unit. We then assembled three electrode pair units together by using ten bolts and placing rubber gaskets in between for sealing. The advantage of this fabrication technique is that each stage of the cell is a highly modulus unit. Therefore, we can easily replace a broken module and maintain the good performance of the cell. However, its disadvantage is that rubber gaskets are usually much thicker than dielectric porous membranes and can potentially encourage more mixing in "phased" charging scheme.
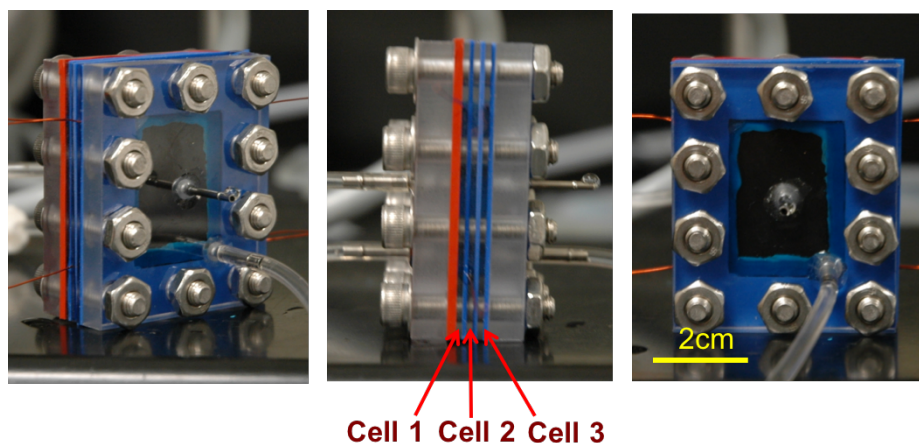
Figure 5.4: Image of a three-stage ftCDI cell made of three electrode-pair-and-separator modulus unit.

5.4   Results and discussion

5.4.1   Novel operation scheme: phased charging

Figure 5.5(a) shows simulation results of a two-stage ftCDI cell operated with "in-phase" mode. Figure 5.5(b) shows simulation results of "phased" charging mode. The cells used in simulation have a cross-section area of 2x3 cm. The electrode thickness is 300 μm. The cells were operated with constant current charging at 15 mA with a threshold voltage of 1.2V for five charging/discharging cycles (only two are shown in Figure 5.5). The flow rate used in simulate was 0.24 mL/min. For "in-phase" charging mode, cell1 and cell2 were charged and discharged simultaneously. Each charging and discharging phase runs about 10 min and there is a 0.5 min equilibrium holding phase between charging to discharging transitions. For "phased" operations, the charging of cell 1 and cell 2 were phased at a 3.5 min shift time, and this shift time is the flushing time to replenish water of one cell volume. Simulation results demonstrate that "phased" charging achieves lower minimum effluent concentration comparing to "in-phase" charging. However, the improvement is not significant. In addition, "phased" mode demonstrates a narrower lower salinity effluent stream window which might lead to lower water recovery.
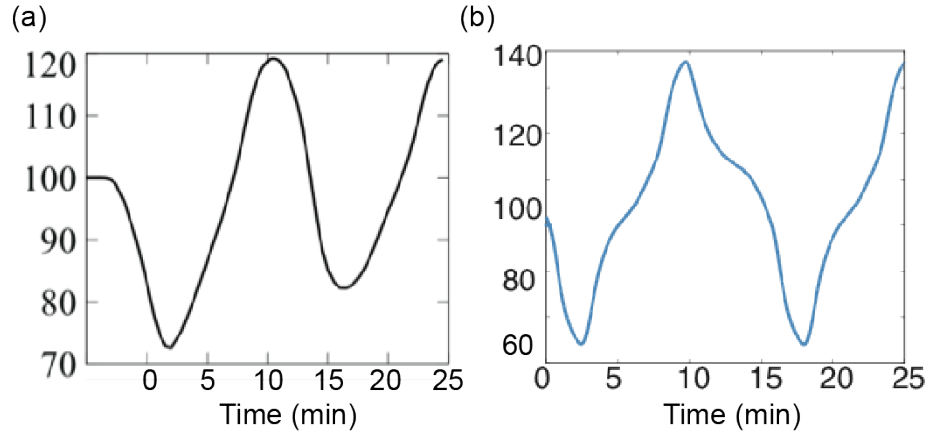
Figure 5.5: Simulation results of a two-stage ftCDI cell operated with (a) "in-phase" and (b) "phased" charging schemes.

5.4.2   Preliminary results of multi-stage operations

Figure 5.6 shows preliminary experimental results of a two-stage ftCDI cell operated with "in-phase" and "phased" charging schemes. The cell is fabricated with electrode-pair-and-separator modulus technique. Each electrode pair was made of two blocks of hierarchical carbon aerogel monoliths (HCAMs) materials with area of 2 x 3 cm and thickness of 300 μm. We used an 80 μm porous paper filter as a separator to insulate between the two electrodes. We used silver epoxy to create intimate electrical contacts between HCAM electrodes and copper wires [70]. The two porous electrodes and a separator were stacked into an assembly and glued on to a polycarbonate frame using epoxy. This assembly was then sandwiched between two 4 x 5 cm polycarbonate endplates with 400 μm silicone rubber sheets as gaskets. Both endplates were milled to accommodate two tubulations: one as a port to flow water, and the other one as a port to release trapped air. The cell was assembled using ten bolts. The cell assembly frame and housing parts were fabricated from polycarbonate.

We performed continuous flow CDI experiments using our two-stage ftCDI cell with 100 mM NaCl. We adopted a CC charging and discharging scheme at 15 mA [93]. We used customized ten-channel charging stations consisting of five Keithley power supplies to provide current and monitor electrical responses. A flow-through conductivity sensor (Edaq, Denistone East, Australia) was attached to the CDI cell downstream to measure the conductivity of effluent solution. A homemade flow-through thermal sensor was used to monitor effluent solution temperature. We used a syringe

pump to flow feed solution through the cell at flow rate 0.24 mL/min. We continuously purged feed solution with house nitrogen to remove dissolved oxygen. Before experiments, we flowed sodium chloride solutions through the cell without charging for 30 min to allow the cell to equilibrate with solutions.

We first performed "in-phase" operations consist of 4 min of charging at 15 mA, 3.5 min of dwell time between charging and discharging, 4 min of discharging and 3.5 min of second dwell time. 3.5 min dwell time is the time that feed water travels about a cell volume in the system. Cell 1 and cell 2 were charged and discharged simultaneously. Figure 5.6 (a) shows effluent concentration profile of five cycles with "in-phase" mode. We then performed "phased" operations with the same cycling steps: 4 min of charging at 15 mA, 3.5 min of dwell time between charging and discharging, 4 min of discharging and 3.5 min of second dwell time. Cell 1 and cell 2 were charged with a phase shift of 3.5 min which means that cell 2 cycles have a 3.5 min delay versus cell 1 cycles.

The experimental results are shown in Figure 5.6 (b). Our preliminary experimental data have decent agreement with simulation predictions (See Figure 5.5). As expected from simulation predictions, the experimental results demonstrate that "Phased" charging operation achieves lower minimum effluent concentration comparing to "in-phase" charging. However, the improvement is not significant. In addition, "phased" mode demonstrates a narrower lower salinity effluent stream window which might lead to lower water recovery. We note that the noisy spikes shown in "in-phased" charging profiles were not shown in simulations. We attribute this discrepancy to non-uniform cell volumes in experiments. Unlike in simulations we can set perfectly matched cell geometries for cell 1 and cell 2, in experiments cell 1 and cell 2 have cell volume deviations due to material synthesis and fabrication uncertainties.
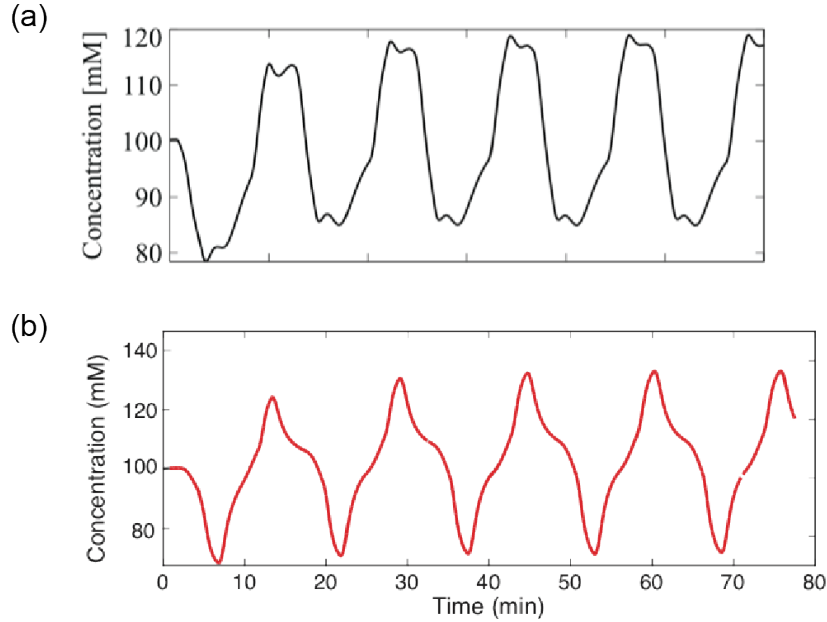
Figure 5.6: Preliminary experimental results of a two-stage ftCDI cell operated with (a) "in-phase" and (b) "phased" charging schemes.

To move forward, much more design and optimization efforts are needed to improve the performance of multi-stage CDI systems. Such studies include optimizing cell design, multi-stage cell assembly and phased-charging steps and timing.

We note that for further experimental and simulation exploration, the deionization and regeneration do not need to have the same flow rates: while deionization is done at a constant flow rate, it is desirable to stop the flow while regenerating the electrode, so that the desorbing salt is accumulated in a volume that is as small as possible. Investigating this issue and determining if and how energy efficiency and water recovery are impacted by phased charging is a crucial part for future work.

5.5 Conclusions

We presented data around efforts to develop a multi-stage ftCDI system with novel phased-charging operation scheme. We extended the numerical model described in Chapter 4 to a multi-stage configuration and demonstrated preliminary simulation. We presented development and fabrication

iterations of two-stage and three-stage ftCDI cells. We demonstrated a novel operation scheme for multi-stage CDI cells, where we subsequently charge and discharge each electrode pair in a multiple electrode pairs cell in a phased manner. From our preliminary experimental data and simulation results, "Phased" charging operation achieves lower minimum effluent concentration comparing to "in-phase" charging. However, the improvement is not significant. Moreover, "phased" mode demonstrates a narrower lower salinity effluent stream window which might lead to lower water recovery. Future studies might include improve the performance of multi-stage CDI systems by optimizing cell design and phased-charging steps and timing.

Chapter 6

Conclusions, contributions and recommendations

This dissertation presented theoretical, experimental and development work on understanding and analyzing energy consumption and charging dynamics for flow-through capacitive systems. In this chapter, we summarize the key contributions and main conclusions of this dissertation. We also present recommendations for future work, including ideas that are significant extensions of this work.

6.1   Summary of major contributions

Characterization of internal resistance of a CDI system

- We developed an equivalent circuit model to characterize internal resistances of CDI systems. This circuit model is based on classical transmission line model which simulates the impedance of porous electrodes as a resistor-capacitor network.

- We characterized resistance components in CDI cells into three groups: 1) setup resistance, 2) contact resistance and interfacial capacitance, 3) transmission line impedance of porous electrodes. We reviewed CDI experimental setups in literature and discovered that contact

resistance is the major resistance contributor in most published CDI cell studies.

- We proposed two simple but effective methods to reduce contact resistance and significantly minimize resistance in the system. The first method is the application of sufficient pressure to press porous electrodes against current collectors. The second is providing intimate contact, such as silver epoxy point contact, between the porous electrode and current collector.

Energy consumption analysis of CV and CC operations

- We developed a simple circuit model and a transmission-line based LTSpice circuit model to elucidate constant current versus constant voltage energy consumption patterns.

- We developed a CDI cell parameter extraction procedure, where we performed ex-situ experiments to characterize resistance, capacitance and leakage currents of a CDI cell. We used these experimentally characterized parameters in circuit models to simulate cell electrical responses, and obtained decent agreement between simulation results and experimental data.

- We demonstrated that constant current operation consumes significantly less energy than constant voltage operation for equal amounts of input charge and identical charging phase duration. In addition, constant current mode demonstrates approximately same salt removal as constant voltage mode.

Charging and fluid flow dynamics of a flow-through CDI system

- We formulated a simple unsteady zero-dimensional lumped parameter model to simulate charging and fluid flow dynamics of ftCDI systems in the advection-limited regime. This formulation suggests dimensionless parameters to characterize cell performance. These parameters include the proper scaling of effluent concentration which is characterized by applied current divided by flow rate, and a characteristic time for charge efficiency scaled by cell capacitance and current.

- We developed a high fidelity one-dimensional numerical model to capture both spatial and temporal responses of a ftCDI cell during charging process. This model is valid for both advection-limited regime and dispersion-limited regime. The numerical model benchmarks the

simulation results from the lumped parameter in advection-limited regime and predicts cell performance in dispersion-limited regime.

- We performed experimental studies to validate simulation results from lumped parameter model and numerical model. We also used dimensionless parameters suggested by lumped parameter model to characterize charging and fluid flow dynamics of CDI cells in two transport regimes: 1) advection-limited regime; 2) dispersion-limited regime.

Towards a multi-stage phased charging CDI systems

- We extended high-fidelity one dimensional numerical model from one-stage cell to multi-stage cell configuration. This extension includes connection domains between cells and individual control of currents for each cell unit.

- We developed a novel multi-stage CDI cell experimental setup. We operated this setup using phased charging scheme, where we subsequently charge and discharge each electrode pair in a multi-stage cell in a phased manner.

- We fabricated two-stage ftCDI cells and three-stage ftCDI cells, and performed preliminary simulations and experiments to compare in-phase and phased charging schemes in terms of salt removals and water recovery.

6.2 Summary of conclusions

Characterization of internal resistance of a CDI system

- Resistance components in a CDI cell can be categorized to three groups: 1) setup resistance, which includes ionic resistance in separator, current collector electrical resistance and resistance of wires; 2) contact resistance between current collectors and porous electrodes; 3) impedance network of resistance and capacitance inside porous electrodes.

- Reviewing CDI cells published in literature, contact resistance is the major contributor to the total cell resistance.

- Contact resistance can be effectively reduced either by applying sufficient pressure to press current collectors against porous electrodes or by infiltrating pores between current collectors and porous electrodes by silver epoxy to create intimate point contact.

Energy consumption analysis of CV and CC operations

- Constant current operation consumes significantly less energy than constant voltage operation for equal amounts of input charge and identical charging phase duration. Higher energy consumption in constant voltage mode is caused by significant resistive dissipation at the beginning of charging and discharging phases.

- Constant current mode has approximately same salt removal as constant voltage and avoids initial high-power resistive dissipation of constant voltage mode.

Charging and fluid flow dynamics of a flow-through CDI system

- In advection-limited transport regime, flow rate, differential charge efficiency and applied current determine the deionization dynamics of a ftCDI cell. Early charging in this regime is characterized by a rise in differential charge efficiency from zero to unity over a time scale determined by charging current and cell capacitance. The charging process later transitions to a quasi-steady state wherein near unity charge efficiency results in an inlet-to-outlet drop in salt concentration that is directly proportional to a ratio of applied current and flow rate.

- In dispersion-limited regime, both differential charge efficiency and dispersion are critical for salt adsorption/desorption dynamics, whereas flow has nearly no impact on deionization outcome.

Towards a multi-stage phased charging CDI systems

- Operating a multi-stage CDI system with phased charging scheme can potentially increase salt removal and water recovery of a single pass operation. However, significant more research work is needed to optimize the system to enhance water throughput, energy consumption and water recovery.

6.3 Recommendations for future work

We here recommend future work including ideas for significant extensions of the current work:

Device-level development

- We recommend scaling up of flow-through electrode capacitive desalination cells for improved performance and throughput. The cells developed in this dissertation have cell volume ranges from 0.2 mL to 3 mL. We estimated that our ftCDI cells are able to produce 10 liters of water per day. However, there remains significant room to further improve water throughput to meet basic water requirements for a household or a small community. Future scale-up efforts include fabricating larger HCAM materials and stacking more cells to build larger units. Ideally, the ftCDI system would demonstrate high-performance desalination and produce at least 200 L of desalted water per day.

- Currently, long-term performance evaluation is not available for ftCDI systems. Long-term operation might introduce performance decay caused by electrodes degradation and components corrosion. We believe that future cell development will benefit significantly from long-term stability studies, and we recommend monitoring surface group composition changes and potential of zero charge shifts of carbon electrodes in long-term operations.

Theory

- We recommend extending our theoretical models to incorporate parasitic Faradaic reactions on porous electrode surfaces. Parasitic reaction is one of the major charge loss and energy dissipation mechanisms in CDI systems. We believe that a more comprehensive and accurate model should capture the kinetics of parasitic reactions.

- In real CDI applications, the system absorbs and desorbs multiple species of ions, not the idealized two symmetric ions system as we presented in our theoretical studies. Multi-species modeling work will enable studies of pH effects and selective adsorption based on ion selectivity.

Operation optimization

- CDI systems have the flexibility of using arbitrary voltage or current sources. Future operations of a CDI cell should not be limited to constant current or constant voltage charging schemes. Design and optimization of novel operation schemes can further improve cell performance.

- We presented preliminary studies of building multi-stage ftCDI cells and operate them with novel phased charging schemes. Significantly more efforts are needed to optimize the systems. Future work could focus on optimizing cell geometry, phased charging steps and timing, operation voltage window and coupling of charging and flow rates.

System-level integration

- CDI cells can be leveraged to integrate with other functional modules or water purification systems. Potential module-level integration includes coupling with energy recovery circuit to achieve reuse of charging energy and integrating with renewable solar energy. System-level integration includes combining with electro-chlorination unit to achieve multi-purpose water treatment. Figure 6.1 provides an integration and application example of ftCDI systems. An ftCDI electrodeionization unit consisting of twelve pairs of electrodes is combined with an electrocholorination unit as a water purifier appliance. The integrated system utilizes renewable energy supplied from solar panels. This water purification unit is capable of producing 0.5 m^3 of water per day for a household or a small community in rural areas.
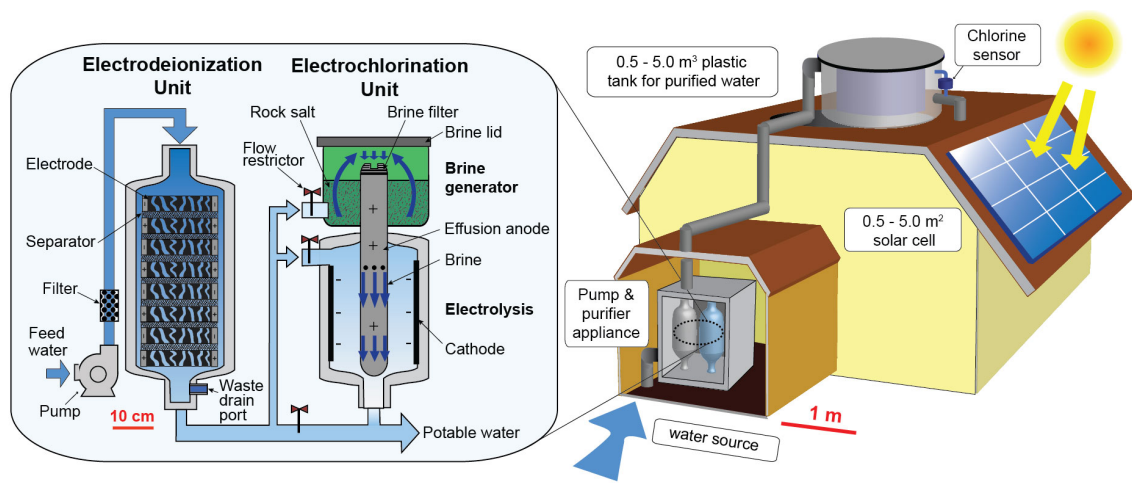
Figure 6.1: A distributed application example of highly integrated ftCDI systems. This system consists of an electrodeionization units made of a mult-stage ftCDI cell, a electrochlorination water purification unit and solar panels as energy sources.

Appendix A

Resistance estimation and characterization in CDI cells

Resistance calculation and estimation in CDI cells

Setup resistance includes ionic resistance in separator, electrical resistance of current collectors and connecting wires, as shown in equation A.1:

$$R_s = R_{separator} + R_{collector} + R_{wire} \tag{A.1}$$

Connecting wire resistances can be approximately measured by a multimeter. They usually account for fractions of 1 ohm. In our resistance estimates of CDI devices reported in literature, we assume wire resistance to be 0.3 Ω in all cases.

To calculate the ionic resistance in separator, we use the model described by equation A.2:

$$R_{separator} = \frac{\tau_s l_s}{\sigma_i \psi_s A_s}, \tag{A.2}$$

Here, l_s is the thickness of separator, A_s is the geometric cross-section area of separator, σ_i is the conductivity of salt solution, ψ_s is the porosity of the separator, and τ_s represents the tortuosity of the separator.

For current collector resistance, we calculate it using equation A.3:

$$R_{collector} = \frac{l_c}{\sigma_c A_c},\tag{A.3}$$

l_c is the thickness of current collector, A_c is the geometric cross-section area of current collector, and σ_c is the electrical conductivity of current collector.

Estimation of ionic resistance across an ion exchange membrane

For a CDI cell with one or more ion exchange membranes, we include the ionic resistance across the membrane when estimating the total characteristic series resistance. This resistance can be calculated using the information reported in the product specification sheets of the membranes, which is usually reported in the form of sheet resistance of the membrane when filled with a specified concentration of test solution. These test solutions are often chosen by membrane manufacturers to minimize the reported resistance. Hence, we typically assume this reported resistance as a minimum expected resistance of the membrane, and independent of feed water concentration.

Estimation of the nominal value of solution ionic resistance (for the solution inside porous electrodes)

For the purpose of resistance estimations, we model porous electrodes simply as a large number of idealized and non-intersecting, tortuous microchannels in parallel1 Figure A.1. This structure can be characterized by the total volume of electrodes, V_e, the void volume, V_v, its macroscopic thickness l_e, and the tortuous characteristic length of the pores L_e. The ratios V_v/V_e and L_e/l_e are defined as the porosity ψ_e and tortuosity τ_e, respectively. Given this, the nominal ionic resistance of salt solution in porous electrode is given by eq. A.4:

$$R_i = \frac{\tau_e l_e}{\sigma_i \psi_e A_e},\tag{A.4}$$
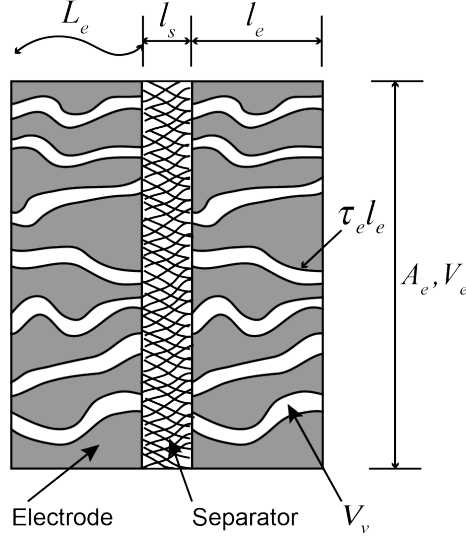
Figure A.1: Schematic of the model of porous electrode and separator of a CDI cell.

Procedures to extract an area-normalized equivalent series resistance (ANESR) from charging or discharging profiles

As described in Chapter 2, we define area-normalized equivalent series resistance (ANESR) in each of two operational modes: constant current (CC) and constant voltage (CV). Within each mode, we also define charging resistances and discharging ANESR. Figure A.2a illustrates charging and discharging absolute equivalent series resistances (ESRs) in a simulated CC cycling profile; and Figure A.3b describes these two ESRs in a simulated CV cycling profile. The associated simulations are described in more detail in Appendix B below. As per our resistance model, this ESR is approximately the sum of setup resistance and contact resistance: $R_s + R_{ct}$. We then normalize ESR by electrode geometric area A and cell number in a stack N to obtain ANESR, $(R_s + R_{ct})AN$.
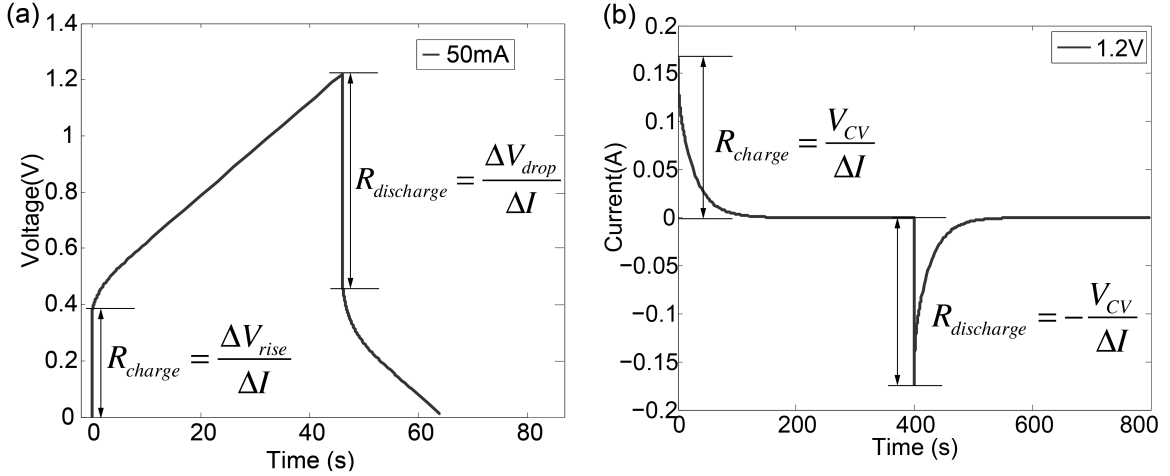
Figure A.2: ESRs in charging and discharging cycling profiles in one of two operational modes: a) CC operation mode; b) CV operation mode. Shown are simulations of a CDI cell using the model discussed in Appendix B

Internal diagnosis of our CDI cell

For the ftCDI cell we used for resistance characterization in Chapter 2, Figure A.3a shows a typical measured charging profile in CV mode at 1 V. We divide the voltage by instant charging current to obtain a charging ESR as 60.9 Ω. This resistance is much larger than the setup resistance (0.5 Ω) as we estimated from solution and separator properties. To diagnose the components of the measured ESR, we performed EIS to the whole cell, as shown in Figure A.3b. The extracted value of this contact resistance is 57.2 Ω, which constitutes 94% of ESR in our cell. This observation supports the hypothesis that contact resistance is the major contributor to internal resistance in CDI cells.
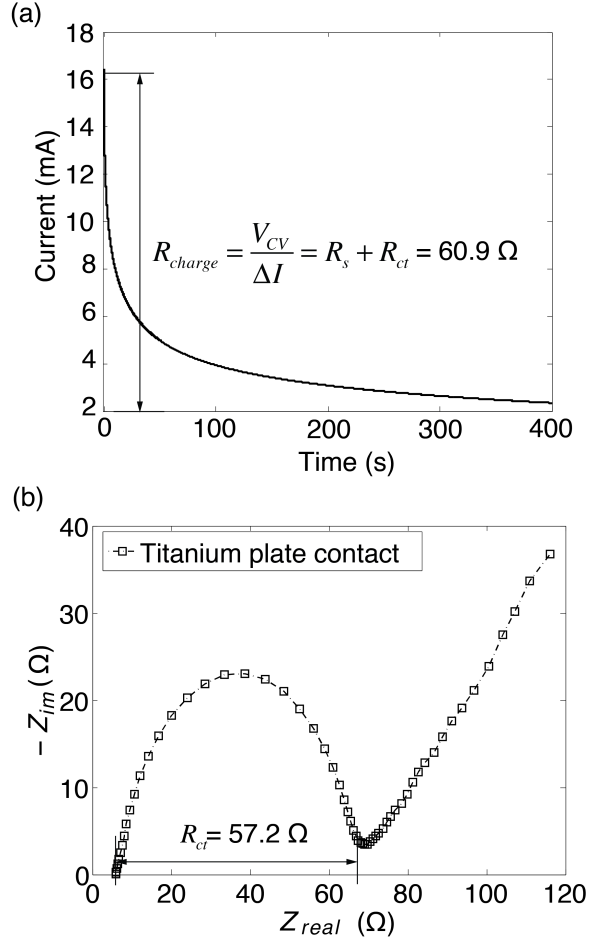
Figure A.3: (a) ESR extraction from CV charging profile of our flow-through CDI cell. The extracted ESR is 60.9 Ω; (b) Nyquist plot of flow-through CDI cell with 100 mM NaCl. The contact resistance extracted from this EIS data is 57.2 Ω, indicating the majority of ESR is contact resistance.

Extracted resistance and interfacial capacitance from EIS data for flow-through CDI cell

We extracted numbers of resistance and interfacial capacitance from the EIS data shown in Figure 2.4 in Chapter 2, using the equivalent circuit proposed in Figure 2.1 in Chapter 2. We converted constant phase element parameter Q_{ct} to interfacial capacitance C_{ct} [57]. Table A.1 summarizes the extracted resistance and interfacial capacitance. As pressure increased from less than 1 to 30

Table A.1: Extracted resistance and interfacial capacitance from EIS data for flow-through CDI cell

Pressure(kPa)	$R_s(\Omega)$	$C_{ct}(\mu F)$	% of C_{ct} reduced	$R_{ct}(\Omega)$	% of R_{ct} reduced
< 1	0.58	22.0	0%	7.5	0%
5	0.56	21.5	2.2%	6.8	9.3%
15	0.58	20.9	5.0%	5.8	23%
30	0.63	20.3	7.7%	4.8	36%

kPa, the dominant semicircle feature of the Nyquist plot shrunk. The contact resistance, which is associated with the diameter of semicircle feature, decreased from 8.8 to 5.5 Ω, nearly 40% reduction. At the same time, the interfacial capacitance was reduced by 7.7% from 22.0 μF to 20.3 μF. The capacitance did not change substantially, but appeared to trend downward with increased pressure. These trends indicate that contact area was created at the expense of reducing the capacitive surface, and that the sum of the microscopic electrical contact area and interfacial capacitance surface area was not constant.

Appendix B

Simple RC model, LTSpice model and simulations of time-dependent responses of CDI

Simulation results from a simple RC circuit

We here further describe the simple RC circuit model of a CDI cell (mentioned in Chapter 3) to compare energy consumption of CV and CC modes, as a first-order of analysis. Our experiments suggest our cell has a total resistance R of 7.64 Ω and electrical double layer capacitance C of 3.84 F. Energy consumption of CV and CC modes using the simple RC circuit are evaluated by Equation 3.4 and 3.7 in Chapter 3, under the conditions of the same amounts of input charge and identical timespans. Figure B.1a presents simulated energy consumption with charging phase durations from 60 to 600 s, and it shows that CV consumes significantly more energy than CC, especially with longer charging times. Figure B.1b shows the simulated consumption ratios of CC to CV.
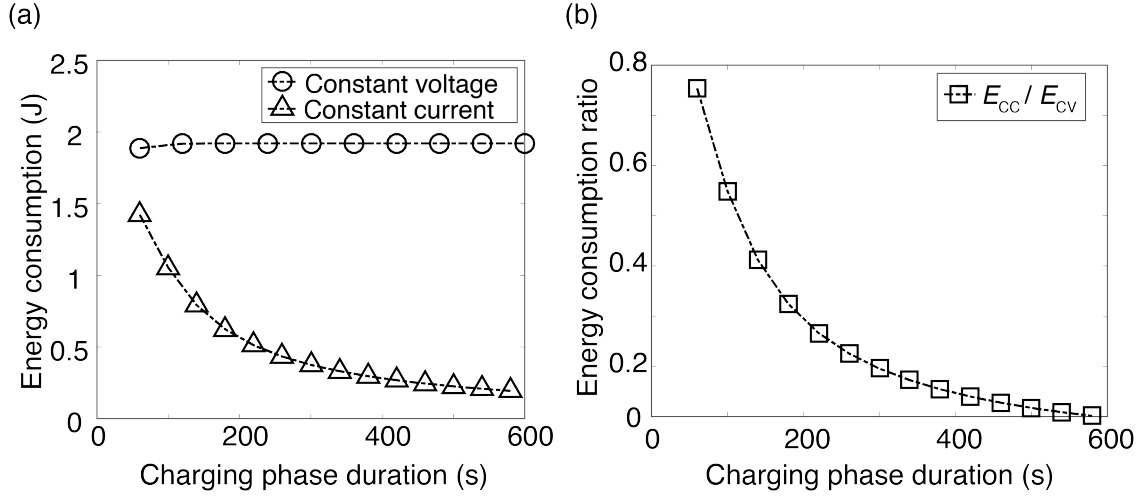
Figure B.1: a) Simulated energy consumption of a CDI cell using simple RC circuit in charging process with CV and CC modes. b) Simulated energy consumption ratio of CC to CV.

LTspice model description

We performed LTspice simulations to investigate the charging dynamics and energy consumption of a CDI cell. In our model, we have a setup resistance, a contact resistance, and two electrodes each modeled via a TL with 20 resistor-capacitor units (Figure B.2). Each resistor-capacitor unit has a value chosen to reflect the actual resistances or capacitances in our ftCDI cell. We characterized R_s, R_{ct}, and R_i from electrochemical impedance spectroscopy (EIS) data as later described Appendix D. The characterized R_i and R_e of each electrode are related to the resistance of each element R_{i1}, R_{i2}, R_{i19} and R_{e1}, R_{e2}, R_{e20} as follows:

$$R_{i(j)} = R_j/N_j, R_{e(k)} = R_e/N_e (j = 1, 2, ..., 19; k = 1, 2, ..., 20) \tag{B.1}$$

where N_i and N_e are the (arbitrarily chosen) number of elements of our discretization. We here chose N_i as 19 and N_e as 20 for each electrode.

The capacitances of each electrode C were measured by cyclic voltammetry of the whole CDI cell, as later described in Appendix D. We assume that capacitance remains constant during charging

process. The capacitance of each electrode C is related to each capacitor in the circuit C_1, C_2, C_{20} as follows:

$$C_{(}m) = C/N_c(m = 1, 2, ..., 20) \tag{B.2}$$

we here chose N_c as 20.

We model parasitic reactions of porous electrodes as non-linear resistances R_1, R_2, R_{20} which follow a Bulter-Volmer equation. In LTspice, a parasitic reaction resistor is in parallel with an EDL capacitor and we used a sub-circuit to model its non-linear behavior. We describe the characterization and modeling of parasitic reactions in Appendix D.
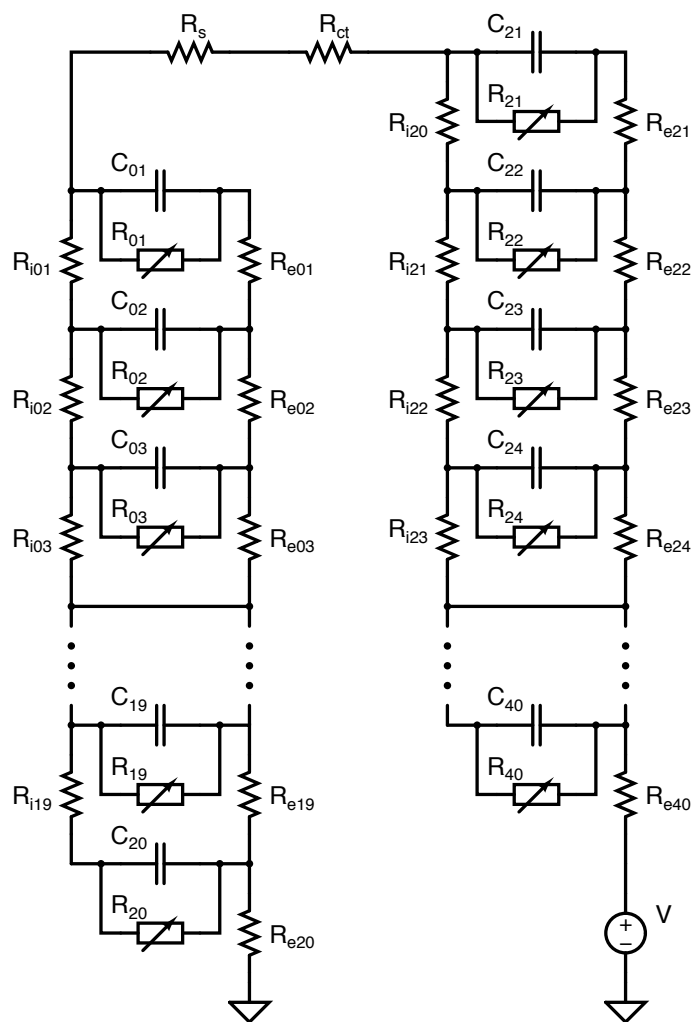
Figure B.2: Schematic of LTspice circuit model used in simulations. We discretized the electrodes using a transmission line modeling approach, and each electrode is represented by 20 resistor-capacitor units. The values of each resistor, capacitor and non-linear parasitic reaction element were determined by independent CDI cell characterization experiments to correctly reflect the properties of our CDI cell.

LTSpice simulations of time-dependent responses of CDI systems

We simulated charging and discharging cycles in both CV and CC operation modes. The current and voltage responses depend on the time regimes of the simulation. Figure B.3a shows the current response in CV mode with 1.2 V charging voltage within 100 μs after the cycle starts. The model exhibits a relatively high and sharp current spike within this time regime due to the rapid charging of the interfacial capacitor C_{ct}, as expected. As mentioned above, we hypothesize that this high current spike is not typically observed in practice due to the common limitations of experimental setups. For example, potentiostats limit the maximum current that can be drawn in the system to protect their circuitry. In addition, data recorded by potentiostats usually has a time delay due to the experiment configuration and instrument limitation. This time delay is usually on the order of several milliseconds. For example, in the experiments presented in this work, this time delay is approximately 10 ms.

Figure B.3b shows the current response from more easily addressable regime of 10 ms to 50 s under the same charging condition. This plot is more representative of current responses observed in CV cycling experiments. Plotted in B.3c is the value of current as a function of resistor number in the abscissa and time in the ordinate. The dark lines are contours separated at an increment of 17 mA. The contour shapes demonstrate the propagation current flow from high to low values of the bulk material electrical resistor number (R_{ek}) and from low to high values of the ionic resistors number (R_{ij}) immediately after applying 1.2 V constant voltage at $t = 0$ s. The applied voltage is reversed at $t = 400$ s, and again we see discharging current propagating from high to low numbers of R_{ek} and from low to high numbers of R_{ij}. These contours show how the system quickly achieves mirror symmetry of the current distribution through ionic resistors vs. the current distribution through bulk material electrical conductive resistors. Since the bulk material conductive resistance R_e is negligible (only 0.0065 Ω per electrode in our model), in the fully developed charging state (where the current is approximately evenly distributed between bulk electrode resistance R_e and the solution ionic resistance in porous electrode R_i), the equivalent resistance of a porous electrode is then approximated as $R_i/2$.

Figure B.3d shows the voltage response in CC mode with 1 mA charging current within 100 μs after the cycle starts. The nearly instantaneous voltage rise at the beginning is only associated with the setup resistance R_s. Figure B.3e shows the voltage response from 10 ms to 50 s under the same charging condition. The time constant associated with the product of R_{ct} and C_{ct} is on the order of a hundred microseconds. Therefore, in this time regime, the interfacial capacitor C_{ct} is saturated and the mainstream current only passes through R_{ct}. The voltage rise at the beginning in Figure B.3e is then associated with the sum of setup resistance R_s and contact resistance R_{ct}, which is the ESR we have defined for charging/discharging cycles. Plotted in B.3f is the value of current as a function of resistor number in abscissa and time in the ordinate. Here, the dark lines are contours separated at an increment of 7.4 mA. The contours demonstrate the propagation current flow from high to low values of the bulk material electrical resistor number (R_{ek}) and from low to high values of the ionic resistors number (R_{ij}) immediately after applying 50 mA constant current at $t = 0$ s. The applied current is reversed at $t = 46$ s, and again we see discharging current propagating from high to low numbers of R_{ek} and from low to high numbers of R_{ij}. Similar to CV mode, these contours also show how the system achieves mirror symmetry of the current distribution between ionic resistors vs. bulk material electrical conductive resistors at fully developed charging state. Therefore, at fully developed charging state (where the current is approximately evenly distributed between bulk electrode resistance R_e and the solution ionic resistance in porous electrode R_i), the equivalent resistance of a porous electrode is also $R_i/2$.
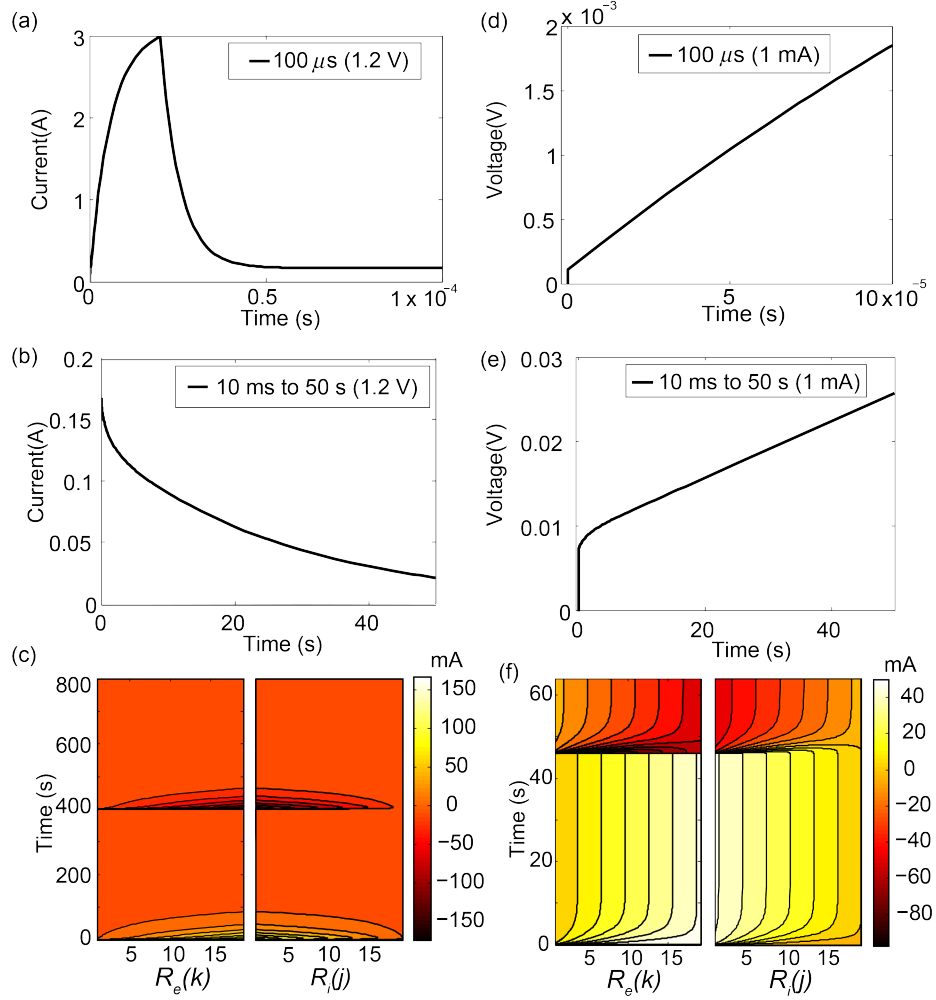
Figure B.3: Current and voltage responses for a CDI cell operated in CV and CC modes. (a) (c) show current responses of a CDI cell in CV mode with 1.2 V in (a) 100 μs and (b) 10 ms to 50 s charging regime, (c) shows the mirror symmetry of current distribution through the bulk material electrical resistors $R_{e(k)}$ and ionic resistors $R_{i(j)}$ at fully developed charging state in a CV cycle with 1.2 V charging voltage. (d) (f) show voltage responses of a CDI cell in CC mode with 1 mA in (d) 100 μs and (e) 10 ms - 50 s charging regimes, (f) shows the mirror symmetry, at fully developed charging state, of current distribution through the bulk material electrical resistors $R_{e(k)}$ and ionic resistors $R_{i(j)}$ in a CC cycle with 50 mA charging/discharging current.

Appendix C

Model and characterize parasitic reactions

We characterized parasitic reaction currents by performing constant voltage experiments at 0.2, 0.4, 0.6, 0.8, 1.0 and 1.2 V while flowing feed solution through the cell, and recorded leakage currents after 10 min of charging. We then fitted these leakage current data to characterize the parasitic reactions. In our LTspice model, there are 20 leakage resistor elements in parallel with EDL capacitors for each electrode. Therefore, we divide the measured leakage currents by 20 to obtain current flowing through each resistor. These leakage currents are measured after 10 min of charging, so we can expect the voltage drops across each capacitor element (and therefore each leakage resistor element) to be approximately uniform. We therefore characterize the leakage current voltage using a single value applicable to the cell under these conditions. The voltage across a leakage resistor is obtained by subtracting an ohmic drop of setup resistance and contact resistance from cell voltage and then dividing this by two, as shown in Equation C.1.

$$V_{leak} = 1/2(V_{cell} - I_{cell}(R_s + R_{ct}))$$
(C.1)

We fit parasitic currents data to characterize its voltage dependence. First, we assume that there is a turn-on voltage for parasitic reactions and we define it as V_0. We also assume that, below

threshold voltage V_0, the leakage resistor behaves as a large constant resistor with a value of 50 $k\Omega$. When the voltage is above threshold, the leakage resistor behaves non-linearly and follows Bulter-Volmer equation. Equation C.2 shows the fit:

$$I_{leak} = \frac{V_0}{50k} e^{\alpha(-V_0+V)} \tag{C.2}$$

We obtained fitting parameters V_0 as 0.145 V and as 7.12 (1/V). In implementing this relation into the model for CDI cell operation, the variable V is then the local, element-specific voltage for each leakage resistor element. Figure C.1a shows a comparison between experimental data and our leakage resistor element model. Here, the current is the parasitic current through each leakage resistor and voltage is the voltage across one electrode (from the leakage current experiments). Figure 2.5b compares simulated total parasitic currents from LTspice model after implementing non-linear leakage resistor to experimental data. The simulation data agree well with experimental data, which validates the fitting procedures.
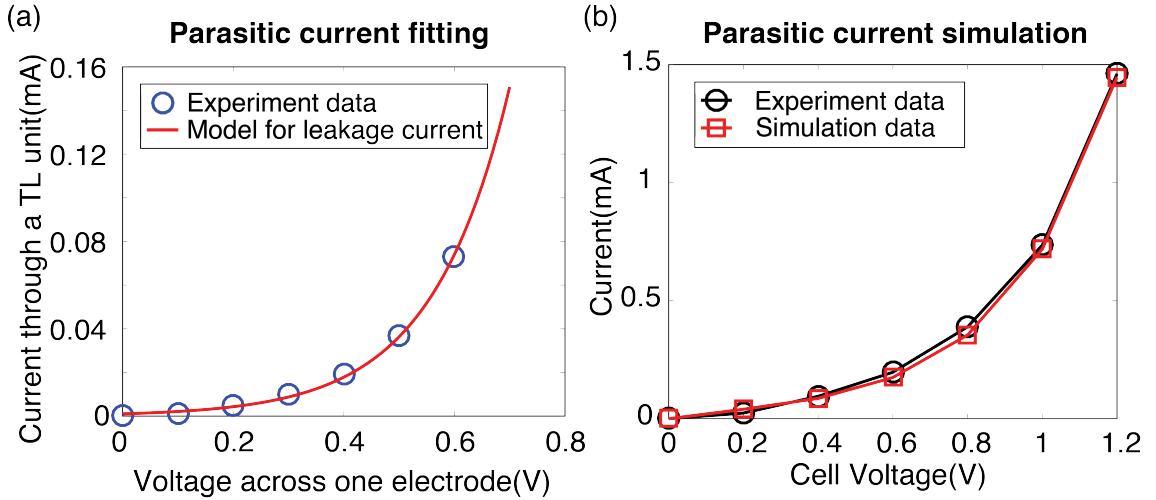
Figure C.1: Fitting experiment data with Bulter-Volmer equation to characterize parasitic current through each leakage resistor element. Blue circles are experimental data and the red line represents the model for leakage current. b) Parasitic currents of the whole CDI cell simulated by LTspice model after implementing non-linear leakage resistors. The simulation data agree well with experimental data.

Appendix D

Additional measurements of CDI cells and HCAM materials

Cyclic voltammetry to evaluate charging capacitances

As mentioned in Chapter 3, apparent capacitances of porous electrodes depend on charging rates [84–86]. In order to accurately assess equilibrium EDL capacitance, we performed cyclic voltammetry experiments at a slow scan rate of 1.67 mV/s. Figure D.1 shows measured differential capacitances of our ftCDI cell within a voltage window from -0.2 to 1.3 V. We averaged capacitance values from 0 to 1 V in positive sweeping phases as the capacitance inputs for LTspice models.
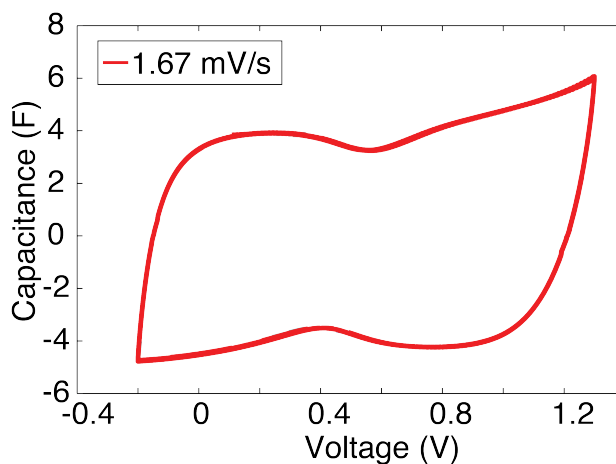
Figure D.1: Cyclic voltammetry of ftCDI cell at scan rate of 1.67 mV/s. The measurement voltage window is from -0.2 to 1.3 V.

Electrochemical impedance spectroscopy to measure resistances

We characterized resistances of our (entire assembled) ftCDI cell (described in Chapter 3) using electrochemical impedance spectroscopy (EIS) using a potentiostat. EIS was performed in a two-terminal configuration without a reference electrode since the electrodes of the cell were symmetric. We applied a 10 mV amplitude sinusoidal potential perturbation and scanned over a frequency range from 700 kHz to 10 mHz at 0V bias. During electrochemical tests, the cell was filled with 100mM NaCl. Figure D.2 shows Nyquist plot of EIS response of our ftCDI cell. We extract the values of R_s, R_{ct}, and R_i from the plot as shown in Figure D.2 [53, 70].
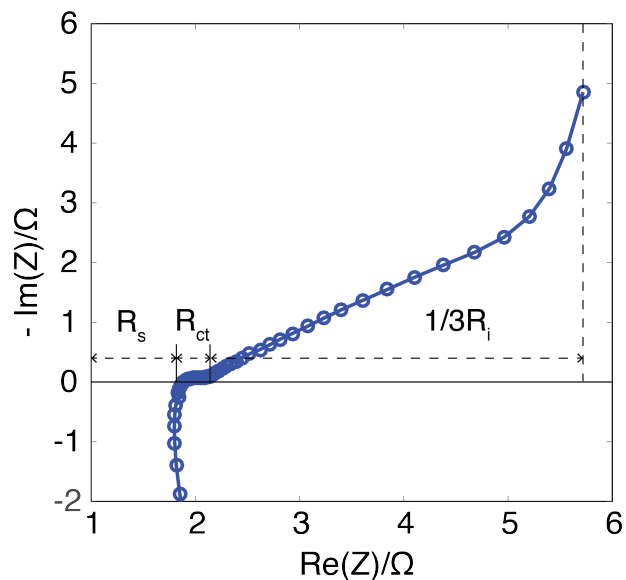
Figure D.2: Nyquist plot of ftCDI cell measured using electrochemical impedance spectroscopy for frequencies within 700 kHz to 10 mHz. The values of R_s, R_{ct}, and R_i are distances along the real axis and are denoted as the labeled line segments flanked by asterisks.

Comparison of input charge from experiments and simulations

Figure D.3 shows the comparison of input charge of CV and CC modes from experimental data and simulation results, as described in Chapter 3. Simulations consistently predict higher input charges than experiments because the model does not capture the dynamic changes of ionic resistances during desalination (particularly important for constant voltage operation for short duration times). Note that CC simulations use input current from experiments and so charge transferred matches exactly with experiments.
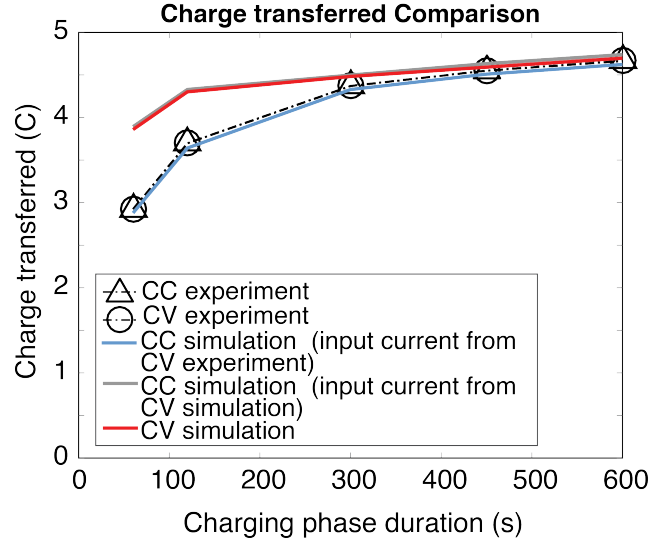
Figure D.3: Charge transfer comparison of experimental and simulation results of a ftCDI cell in CV or CC mode with charging times of 1, 2, 5, 7.5 and 10 min. CV and CC modes were operated under the conditions of the same input charges and identical charging phase timespans.

Compression test of HCAM samples

We performed nanoindentation of HCAM material to evaluate its elastic modulus. HCAM samples were tested in a homebuilt machine that was designed specially for ultralow-stiffness materials [102, 103]. The indentation was performed with a steel sphere indenter with the radius of 1 mm at displacement speed of 50 μm/min. Figure D.4 shows the typical loading and unloading curves of HCAM samples. The inset figure shows the unloading Youngs modulus obtained from analyzing load-unload data. The loading might include inelastic deformation, whereas unloading is purely elastic bouncing. Consequently, we here use the unloading Youngs modulus as our estimate of the elastic modulus of HCAM material. The measured elastic modulus of the HCAM samples is within the range from 110 to 137 MPa. These data further support our conclusion that our compression experiments described in the main paper are within the elastic response region for the HCAM.
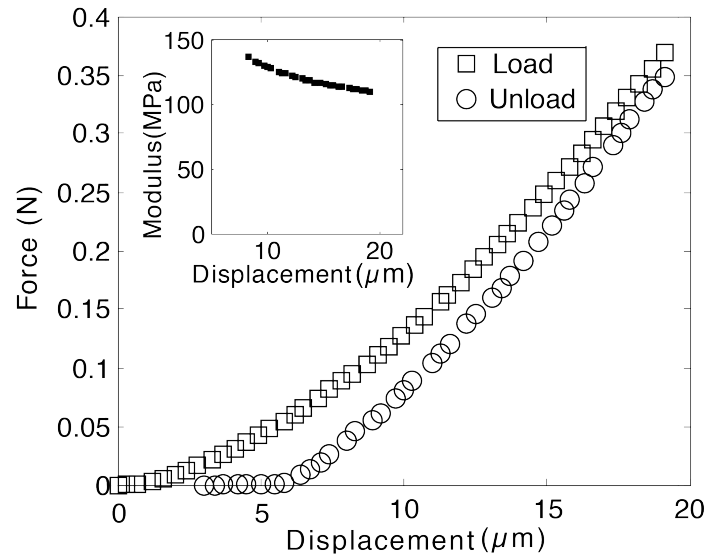
Figure D.4: Typical continuous load-unload curves for a HCAM sample indented with steel sphere indenter. Inset shows the unloading Youngs modulus obtained from load-unload data analysis.

Bibliography

[1] Mesfin M. Mekonnen and Arjen Y. Hoekstra. Four billion people facing severe water scarcity. *Science Advances*, 2(2), 2016.

[2] Arjen Y. Hoekstra and Thomas O. Wiedmann. Humanitys unsustainable environmental footprint. *Science*, 344(6188), 2014.

[3] United Nations Environment Programme. VITAL WATER GRAPHICS. An Overview of the State of the Worlds Fresh and Marine Waters. Technical report, United Nations Environment Programme, 2008. URL `http://www.secheresse.info/spip.php?article12063`.

[4] WHO — What is the minimum quantity of water needed? *WHO*, 2016.

[5] Peter H Gleick. Basic water requirements for human activities: Meeting basic needs. *Water international*, 21(2):83–92, 1996.

[6] Asieh Namdar. US has worlds highest water consumption rate per capita. URL `http://www.cctv-america.com/2015/03/25/46423`.

[7] Amber Brown and Marty D Matlock. A Review of Water Scarcity Indices and Methodologies. Technical report, University of Arkansas The Sustainability Consortium, 2011.

[8] Simon N. Gosling and Nigel W. Arnell. A global assessment of the impact of climate change on water scarcity. *Climatic Change*, 134(3):371–385, 2 2016. doi: 10.1007/s10584-013-0853-x. URL `http://link.springer.com/10.1007/s10584-013-0853-x`.

[9] NATIONAL BRACKISH GROUNDWATER ASSESSMENT. Technical report, U.S. Geological Survey.

[10] Mike Mickley. Inland desalinationCurrent status and challenges. In *Annual WateReuse Symposium, 25th*, Washington, D.C., 2010.

[11] A.L. Shea. Status and challenges for desalination in the United States, in Reuse & Desalination. In *Water Scarcity Solu- tions for the 21st Century Conference*, Sydney, Australia, 2010. URL `http://www.watereuse.org/information-resources/about-desalination/presentations`.

[12] Noreddine Ghaffour, Thomas M. Missimer, and Gary L. Amy. Technical review and evaluation of the economics of water desalination: Current and future challenges for better water supply sustainability. *Desalination*, 2013. ISSN 00119164. doi: 10.1016/j.desal.2012.10.015.

[13] International Desalination Association. Desalination by the Numbers. URL `http://idadesal.org/desalination-101/desalination-by-the-numbers/`.

[14] M.A. Alghoul, P. Poovanaesvaran, K. Sopian, and M.Y. Sulaiman. Review of brackish water reverse osmosis (BWRO) system designs. *Renewable and Sustainable Energy Reviews*, 13(9): 2661–2667, 2009. doi: 10.1016/j.rser.2009.03.013.

[15] James E Miller. Review of water resources and desalination technologies. Technical report, Albuquerque, New Mexico, 2003.

[16] M Elimelech and W A Phillip. The future of seawater desalination: energy, technology, and the environment. *Science*, 333(6043):712–717, 2011. ISSN 1095-9203 (Electronic) 0036-8075 (Linking). doi: 10.1126/science.1200488. URL `http://www.ncbi.nlm.nih.gov/pubmed/21817042`.

[17] Asam Almullaa, Mohamed Eidb, Pierre C&f, and John Coburn. Developments in high recovery brackish water desalination plants as part of the solution to water quantity problems. *DESALINA˜ON Desalination*, 153:237–243, 2002. URL `www.elsevier.com/locateJdesal`.

[18] O.K. Buros. The ABCs of Desalting. Technical report, International Desalination Association, 2000.

[19] Anditya Rahardianto, Junbo Gao, Christopher J. Gabelich, Mark D. Williams, and Yoram

Cohen. High recovery membrane desalting of low-salinity brackish water: Integration of accelerated precipitation softening with membrane RO. *Journal of Membrane Science*, 289(1): 123–137, 2007. doi: 10.1016/j.memsci.2006.11.043.

[20] Arun Subramani and Joseph G Jacangelo. Emerging desalination technologies for water treatment: a critical review. *Water research*, 75:164–187, 2015.

[21] Tamim Younos and Kimberly E Tulou. Energy Needs, Consumption and Sources. doi: 10.1111/j.1936-704X.2005.mp132001005.x.

[22] M E Suss, S Porada, X Sun, P M Biesheuvel, J Yoon, and V Presser. Water desalination via capacitive deionization: what is it and what can we expect from it? *Energy Environ. Sci.*, 8 (8):2296–2319, 2015. ISSN 1754-5692 1754-5706. doi: 10.1039/c5ee00519a.

[23] S Porada, R Zhao, A van der Wal, V Presser, and P M Biesheuvel. Review on the science and technology of water desalination by capacitive deionization. *Progress in Materials Science*, 58 (8):1388–1442, 2013. ISSN 00796425. doi: 10.1016/j.pmatsci.2013.03.005.

[24] S Garrido, M Aviles, A Ramirez, C Calderon, and A Ramirez-Orozco. Arsenic removal from water of Huautla, Morelos, Mexico using capacitive deionization. *Natural Arsenic in Groundwaters of Latin America. CRC Press*, pages 655–676, 2008.

[25] R. Zhao, M. van Soestbergen, H. H M Rijnaarts, A. van der Wal, M. Z. Bazant, and P. M. Biesheuvel. Time-dependent ion selectivity in capacitive charging of porous electrodes. *Journal of Colloid and Interface Science*, 2012. ISSN 00219797. doi: 10.1016/j.jcis.2012.06.022.

[26] Eran Avraham, Malachi Noked, Abraham Soffer, and Doron Aurbach. The feasibility of boron removal from water by capacitive deionization. *Electrochimica Acta*, 2011. ISSN 00134686. doi: 10.1016/j.electacta.2011.05.037.

[27] Jin-Hee Yeo and Jae-Hwan Choi. Enhancement of nitrate removal from a solution of mixed nitrate, chloride and sulfate ions using a nitrate-selective carbon electrode. *Desalination*, 320: 10–16, 2013. ISSN 00119164. doi: 10.1016/j.desal.2013.04.013.

[28] Xin Gao, Ayokunle Omosebi, James Landon, and Kunlei Liu. Surface charge enhanced carbon electrodes for stable and efficient capacitive deionization using inverted adsorptiondesorption behavior. *Energy Environ. Sci.*, 8(3):897–909, 2015. ISSN 1754-5692 1754-5706. doi: 10.1039/c4ee03172e.

[29] Ali Hemmatifar, James W Palko, Michael Stadermann, and Juan G Santiago. Energy Breakdown in Capacitive Desalination. *submitted to Water Research*, 2016.

[30] Matthew E Suss, Theodore F Baumann, William L Bourcier, Christopher M Spadaccini, Klint A Rose, Juan G Santiago, and Michael Stadermann. Capacitive desalination with flowthrough electrodes. *Energy & Environmental Science*, 5(11):9511–9519, 2012. ISSN 1754-5692 1754-5706. doi: 10.1039/c2ee21498a.

[31] R Zhao, P M Biesheuvel, and A van der Wal. Energy consumption and constant current operation in membrane capacitive deionization. *Energy & Environmental Science*, 5(11):9520, 2012. ISSN 1754-5692 1754-5706. doi: 10.1039/c2ee21737f.

[32] Joseph C Farmer, David V Fix, Gregory V Mack, Richard W Pekala, and John F Poco. Capacitive deionization of NaCI and NaNO3 solutions with carbon aerogel electrodes. *J. Electrochem. Soc.*, 143(1):159–169, 1996.

[33] R Zhao, S Porada, P M Biesheuvel, and A van der Wal. Energy consumption in membrane capacitive deionization for different water recoveries and flow rates, and comparison with reverse osmosis. *Desalination*, 330:35–41, 2013. ISSN 00119164. doi: 10.1016/j.desal.2013.08.017.

[34] P Dlugolecki and A van der Wal. Energy recovery in membrane capacitive deionization. *Environ Sci Technol*, 47(9):4904–4910, 2013. ISSN 1520-5851 (Electronic) 0013-936X (Linking). doi: 10.1021/es3053202. URL `http://www.ncbi.nlm.nih.gov/pubmed/23477563`.

[35] Onur N Demirer, Rachel M Naylor, Carlos A Rios Perez, Ellen Wilkes, and Carlos Hidrovo. Energetic performance optimization of a capacitive deionization system operating with transient cycles and brackish water. *Desalination*, 314:130–138, 2013. ISSN 00119164. doi: 10.1016/j.desal.2013.01.014.

[36] E Garcia-Quismondo, C Santos, J Lado, J Palma, and M A Anderson. Optimizing the energy efficiency of capacitive deionization reactors working under real-world conditions. *Environ Sci Technol*, 47(20):11866–11872, 2013. ISSN 1520-5851 (Electronic) 0013-936X (Linking). doi: 10.1021/es4021603. URL http://www.ncbi.nlm.nih.gov/pubmed/24015835.

[37] E Garcia-Quismondo, R Gomez, F Vaquero, A L Cudero, J Palma, and M Anderson. New testing procedures of a capacitive deionization reactor. *Phys Chem Chem Phys*, 15(20):7648–7656, 2013. ISSN 1463-9084 (Electronic) 1463-9076 (Linking). doi: 10.1039/c3cp50514f. URL http://www.ncbi.nlm.nih.gov/pubmed/23591701.

[38] R Zhao, O Satpradit, H H Rijnaarts, P M Biesheuvel, and A van der Wal. Optimization of salt adsorption rate in membrane capacitive deionization. *Water Res*, 47(5):1941–1952, 2013. ISSN 1879-2448 (Electronic) 0043-1354 (Linking). doi: 10.1016/j.watres.2013.01.025. URL http://www.ncbi.nlm.nih.gov/pubmed/23395310.

[39] Junil Kang, Taeyoung Kim, Kyusik Jo, and Jeyong Yoon. Comparison of salt adsorption capacity and energy consumption between constant current and constant voltage operation in capacitive deionization. *Desalination*, 352:52–57, 2014. ISSN 00119164. doi: 10.1016/j.desal.2014.08.009.

[40] A G Pandolfo, G J Wilson, T D Huynh, and A F Hollenkamp. The influence of conductive additives and inter-particle voids in carbon EDLC electrodes. *Fuel Cells*, 10(5):856–864, 2010. ISSN 16156846. doi: 10.1002/fuce.201000027.

[41] W G Pell, B E Conway, and N Marincic. Analysis of non-uniform charge/discharge and rate effects in porous carbon capacitors containing sub-optimal electrolyte concentrations. *Journal of Electroanalytical Chemistry*, 491(1-2):9–21, 2000.

[42] Chunhong Lei, Foivos Markoulidis, Zenya Ashitaka, and Constantina Lekakou. Reduction of porous carbon/Al contact resistance for an electric double-layer capacitor (EDLC). *Electrochimica Acta*, 92:183–187, 2013. ISSN 00134686. doi: 10.1016/j.electacta.2012.12.092.

[43] Sonia Dsoke, Xu Tian, Corina Täubert, Steffen Schlüter, and Margret Wohlfahrt-Mehrens.

Strategies to reduce the resistance sources on Electrochemical Double Layer Capacitor electrodes. *Journal of Power Sources*, 238:422–429, 2013. ISSN 03787753. doi: 10.1016/j.jpowsour.2013.04.031.

[44] Hsien-Chang Wu, Yen-Po Lin, Eric Lee, Wen-Ting Lin, Jui-Kai Hu, Hung-Chang Chen, and Nae-Lih Wu. High-performance carbon-based supercapacitors using Al current-collector with conformal carbon coating. *Materials Chemistry and Physics*, 117(1):294–300, 2009. ISSN 02540584. doi: 10.1016/j.matchemphys.2009.06.001.

[45] Aurelien Du Pasquier, Irene Plitz, John Gural, Serafin Menocal, and Glenn Amatucci. Characteristics and performance of 500 F asymmetric hybrid advanced supercapacitor prototypes. *Journal of Power Sources*, 113:62–71, 2003.

[46] P L Taberna, P Simon, and J F Fauvarque. Electrochemical characteristics and impedance spectroscopy studies of carbon-carbon supercapacitors. *Journal of The Electrochemical Society*, 150(3):A292–A300, 2003. ISSN 00134651. doi: 10.1149/1.1543948.

[47] C Portet, P L Taberna, P Simon, and C Laberty-Robert. Modification of Al current collector surface by solgel deposit for carboncarbon supercapacitor applications. *Electrochimica Acta*, 49(6):905–912, 2004. ISSN 00134686. doi: 10.1016/j.electacta.2003.09.043.

[48] Toshiyuki Momma, Xingjiang Liu, Tetsuya Osaka, Yousuke Ushio, and Yoshimitsu Sawada. Electrochemical modification of active carbon fiber electrode and its application to double-layer capacitor. *Journal of Power Sources*, 60(2):249–253, 1996.

[49] T Horiba, K Hironaka, T Matsumura, T Kai, M Koseki, and Y Muranaka. Manganese-based lithium batteries for hybrid electric vehicle applications. *Journal of Power Sources*, 119-121: 893–896, 2003. ISSN 03787753. doi: 10.1016/s0378-7753(03)00202-7.

[50] Ayu Tyas Utami Nugrahenny, Jiyoung Kim, Seongyop Lim, and Doo-Hwan Jung. Development of high performance cell structor for capacitive deionization using membrane polymer-coated electrode.

[51] Bart van Limpt and Prof. dr. ir. W H Rulkens. *Performance relations in capacitive deionization systems*. PhD thesis, 2010.

[52] Theodore F Baumann, Marcus A Worsley, T Yong-Jin Han, and Joe H Satcher. High surface area carbon aerogel monoliths with hierarchical porosity. *Journal of Non-Crystalline Solids*, 354(29):3513–3515, 2008. ISSN 00223093. doi: 10.1016/j.jnoncrysol.2008.03.006.

[53] Matthew E Suss, Theodore F Baumann, Marcus A Worsley, Klint A Rose, Thomas F Jaramillo, Michael Stadermann, and Juan G Santiago. Impedance-based study of capacitive porous carbon electrodes with hierarchical and bimodal porosity. *Journal of Power Sources*, 241: 266–273, 2013. ISSN 03787753. doi: 10.1016/j.jpowsour.2013.03.178.

[54] G J Brug, A L G van den Eeden, M Sluyters-rehbach, and J H Sluyters. The analysis of electrode impedance complicated by the presence of a constant phase element. *Journal of Electroanalytical Chemistry*, 176:275–295, 1984.

[55] R de Levie. On porous electrodes in electrolyte solutions IV. *Electrochimica Acta*, 9(9): 1231–1245, 1964.

[56] Evgenij Barsoukov and J Ross Macdonald. *Impedance Spectroscopy: Theory, Experiment, And Applications*. Wiley, Hoboken, New Jersey, 2nd edition, 2005.

[57] C H Hsu and F Mansfeld. Technical note: concerning the conversion of the constant phase element parameter Y0 into a capacitance. *Corrosion*, 57(9):747–748, 2001.

[58] Miran Gaberscek, Joze Moskon, Bostjan Erjavec, Robert Dominko, and Janez Jamnik. The Importance of Interphase Contacts in Li Ion Electrodes: The Meaning of the High-Frequency Impedance Arc. *Electrochemical and Solid-State Letters*, 11(10):A170, 2008. ISSN 10990062. doi: 10.1149/1.2964220.

[59] Shuhuai Yao and Juan G Santiago. Porous glass electroosmotic pumps: theory. *Journal of Colloid and Interface Science*, 268:133–142, 2003. doi: 10.1016/S0021-9797(03)00731-8.

[60] A Norlin, J Pan, and C Leygraf. Investigation of interfacial capacitance of Pt, Ti and TiN coated electrodes by electrochemical impedance spectroscopy. *Biomolecular Engineering*, 19: 67–71, 2002.

[61] Jin-Ha Hwang, K S Kirkpatrick, T O Mason, and E J Garboczi. Experimental limitation in impedance spectroscopy: Part IV. Electrode contact effects. *Solid State Ionics*, 98:93–104, 1997.

[62] H H Al-Kayiem, C A Brebbia, and S S Zubir. *Energy and Sustainability V*. WIT Press, Southampton, UK, 2015.

[63] Philip N Bartlett, Magdalena Perdjon-Abel, David Cook, Gillian Reid, William Levason, Fei Cheng, Wenjian Zhang, Michael W George, Jie Ke, Richard Beanland, and Jeremy Sloan. The Electrodeposition of Silver from Supercritical Carbon Dioxide/Acetonitrile. *ChemElectroChem*, 1(1):187–194, 2014. ISSN 21960216. doi: 10.1002/celc.201300131.

[64] Subho Dasgupta, Di Wang, Christian Kübel, Horst Hahn, Theodore F Baumann, and Jrgen Biener. Dynamic control over electronic transport in 3D bulk nanographene via interfacial charging. *Advanced Functional Materials*, 24(23):3494–3500, 2014. ISSN 1616301X. doi: 10.1002/adfm.201303534.

[65] X Z Wang, M G Li, Y W Chen, R M Cheng, S M Huang, L K Pan, and Z Sun. Electrosorption of NaCl solutions with carbon nanotubes and nanofibers composite film electrodes. *Electrochemical and Solid-State Letters*, 9(9):E23–E26, 2006. ISSN 10990062. doi: 10.1149/1.2213354.

[66] Yu-Jin Kim and Jae-Hwan Choi. Enhanced desalination efficiency in capacitive deionization with an ion-selective membrane. *Separation and Purification Technology*, 71(1):70–75, 2010. ISSN 13835866. doi: 10.1016/j.seppur.2009.10.026.

[67] S Porada, L Weinstein, R Dash, A van der Wal, M Bryjak, Y Gogotsi, and P M Biesheuvel. Water desalination using capacitive deionization with microporous carbon electrodes. *ACS Appl Mater Interfaces*, 4(3):1194–1199, 2012. ISSN 1944-8252 (Electronic) 1944-8244 (Linking). doi: 10.1021/am201683j. URL http://www.ncbi.nlm.nih.gov/pubmed/22329838.

[68] David Jayne, Ying Zhang, Shaker Haji, and Can Erkey. Dynamics of removal of organosulfur compounds from diesel by adsorption on carbon aerogels for fuel cell applications. *International Journal of Hydrogen Energy*, 30:1287–1293, 2005. doi: 10.1016/j.ijhydene.2005.03.014.

[69] R Leyva-Ramos and C J Geankoplis. Diffusion in liquid-filled pores of activated carbon. I. Pore volume diffusion. *Canadian Journal of Chemical Engineering*, 72:262–271, 1994.

[70] Y Qu, T F Baumann, J G Santiago, and M Stadermann. Characterization of Resistances of a Capacitive Deionization System. *Environ Sci Technol*, 49(16):9699–9706, 2015. ISSN 1520-5851 (Electronic) 0013-936X (Linking). doi: 10.1021/acs.est.5b02542. URL http://www.ncbi.nlm.nih.gov/pubmed/26214554.

[71] Ali Hemmatifar, Michael Stadermann, and Juan G Santiago. Two-Dimensional porous electrode model for capacitive deionization. 2015. doi: 10.1021/acs.jpcc.5b05847.

[72] Yanhong Bian, Peng Liang, Xufei Yang, Yong Jiang, Changyong Zhang, and Xia Huang. Using activated carbon fiber separators to enhance the desalination rate of membrane capacitive deionization. *Desalination*, 381:95–99, 2016. ISSN 00119164. doi: 10.1016/j.desal.2015.11.016.

[73] T Kim, J E Dykstra, S Porada, A van der Wal, J Yoon, and P M Biesheuvel. Enhanced charge efficiency and reduced energy use in capacitive deionization by increasing the discharge voltage. *J Colloid Interface Sci*, 446:317–326, 2015. ISSN 1095-7103 (Electronic) 0021-9797 (Linking). doi: 10.1016/j.jcis.2014.08.041. URL http://www.ncbi.nlm.nih.gov/pubmed/25278271.

[74] Taeyoung Kim and Jeyong Yoon. CDI ragone plot as a functional tool to evaluate desalination performance in capacitive deionization. *RSC Adv.*, 5(2):1456–1461, 2015. ISSN 2046-2069. doi: 10.1039/c4ra11257a.

[75] Linchen Han, K G Karthikeyan, and Kelvin B Gregory. Energy Consumption and Recovery in Capacitive Deionization Using Nanoporous Activated Carbon Electrodes. *Journal of The Electrochemical Society*, 162(12):E282–E288, 2015. ISSN 0013-4651 1945-7111. doi: 10.1149/2.0431512jes.

[76] Y A C Jande and W S Kim. Desalination using capacitive deionization at constant current. *Desalination*, 329:29–34, 2013. doi: 10.1016/j.desal.2013.08.023.

[77] Jae-Hwan Choi. Comparison of constant voltage (CV) and constant current (CC) operation in the membrane capacitive deionisation process. *Desalination and Water Treatment*, 56(4): 921–928, 2014. ISSN 1944-3994 1944-3986. doi: 10.1080/19443994.2014.942379.

[78] Alicia M Oickle and Heather A Andreas. Examination of Water Electrolysis and Oxygen Reduction As Self-Discharge Mechanisms for Carbon-Based, Aqueous Electrolyte Electrochemical Capacitors. *The Journal of Physical Chemistry C*, 115(10):4283–4288, 2011. ISSN 1932-7447 1932-7455. doi: 10.1021/jp1067439.

[79] Y Diab, P Venet, H Gualous, and G Rojat. Self-Discharge Characterization and Modeling of Electrochemical Capacitor Used for Power Electronics Applications. *IEEE Transactions on Power Electronics*, 24(2):510–517, 2009. ISSN 0885-8993 1941-0107. doi: 10.1109/tpel.2008.2007116.

[80] Maximilian Kaus, Julia Kowal, and Dirk Uwe Sauer. Modelling the effects of charge redistribution during self-discharge of supercapacitors. *Electrochimica Acta*, 55(25):7516–7523, 2010. ISSN 00134686. doi: 10.1016/j.electacta.2010.01.002.

[81] David B Robinson. Optimization of power and energy densities in supercapacitors. *Journal of Power Sources*, 195(11):3748–3756, 2010. ISSN 03787753. doi: 10.1016/j.jpowsour.2009.12.004.

[82] Juergen Biener, Michael Stadermann, Matthew Suss, Marcus A Worsley, Monika M Biener, Klint A Rose, and Theodore F Baumann. Advanced carbon aerogels for energy applications. *Energy & Environmental Science*, 4(3):656, 2011. ISSN 1754-5692 1754-5706. doi: 10.1039/c0ee00627k.

[83] M E Suss, P M Biesheuvel, T F Baumann, M Stadermann, and J G Santiago. In situ spatially and temporally resolved measurements of salt concentration between charging porous electrodes for desalination by capacitive deionization. *Environ Sci Technol*, 48(3):2008–2015, 2014. ISSN 1520-5851 (Electronic) 0013-936X (Linking). doi: 10.1021/es403682n. URL `http://www.ncbi.nlm.nih.gov/pubmed/24433022`.

[84] Hainan Wang, Alexander Thiele, and Laurent Pilon. Simulations of Cyclic Voltammetry for Electric Double Layers in Asymmetric Electrolytes: A Generalized Modified PoissonNernstPlanck Model. *The Journal of Physical Chemistry C*, 117(36):18286–18297, 2013. ISSN 1932-7447 1932-7455. doi: 10.1021/jp402181e.

[85] Hainan Wang and Laurent Pilon. Physical interpretation of cyclic voltammetry for measuring electric double layer capacitances. *Electrochimica Acta*, 64:130–139, 2012. ISSN 00134686. doi: 10.1016/j.electacta.2011.12.118.

[86] Meryl D Stoller and Rodney S Ruoff. Best practice methods for determining an electrode material's performance for ultracapacitors. *Energy & Environmental Science*, 3(9):1294, 2010. ISSN 1754-5692 1754-5706. doi: 10.1039/c0ee00074d.

[87] Muhammad Wajid Saleem, Y A C Jande, Muhammad Asif, and Woo-Seung Kim. Hybrid CV-CC operation of capacitive deionization in comparison with constant current and constant voltage. *Separation Science and Technology*, 51(6):1063–1069, 2016. ISSN 0149-6395 1520-5754. doi: 10.1080/01496395.2015.1127258.

[88] Seonghwan Kim, Jaehan Lee, Choonsoo Kim, and Jeyong Yoon. Na2FeP2O7 as a Novel Material for Hybrid Capacitive Deionization. *Electrochimica Acta*, 203:265–271, 2016. ISSN 00134686. doi: 10.1016/j.electacta.2016.04.056.

[89] P M Biesheuvel and A van der Wal. Membrane capacitive deionization. *Journal of Membrane Science*, 346(2):256–262, 2010. ISSN 03767388. doi: 10.1016/j.memsci.2009.09.043.

[90] Y Bian, X Yang, P Liang, Y Jiang, C Zhang, and X Huang. Enhanced desalination performance of membrane capacitive deionization cells by packing the flow chamber with granular activated carbon. *Water Res*, 85:371–376, 2015. ISSN 1879-2448 (Electronic) 0043-1354 (Linking). doi: 10.1016/j.watres.2015.08.058. URL https://www.ncbi.nlm.nih.gov/pubmed/26360230.

[91] B van Limpt P. M. Biesheuvel A. van der Wal. Dynamic Adsorption/Desorption Process Model for Capacitive Deionization. *The Journal of Physical Chemistry C*, 113(14):5636 – 5640, 2009.

[92] Y A C Jande and W S Kim. Predicting the lowest effluent concentration in capacitive deionization. *Separation and Purification Technology*, 115:224–230, 2013. ISSN 13835866. doi: 10.1016/j.seppur.2013.05.022.

[93] Yatian Qu, Patrick G Campbell, Lei Gu, Jennifer M Knipe, Ella Dzenitis, Juan G Santiago, and Michael Stadermann. Energy consumption analysis of constant voltage and constant

current operations in capacitive deionization. *Desalination*, 400:18–24, 2016. ISSN 00119164. doi: 10.1016/j.desal.2016.09.014.

[94] P M Biesheuvel, Y Fu, and M Z Bazant. Diffuse charge and Faradaic reactions in porous electrodes. *Phys Rev E Stat Nonlin Soft Matter Phys*, 83(6 Pt 1):61507, 2011. ISSN 1550-2376 (Electronic) 1539-3755 (Linking). doi: 10.1103/PhysRevE.83.061507. URL https://www.ncbi.nlm.nih.gov/pubmed/21797372.

[95] P M Biesheuvel, R Zhao, S Porada, and A van der Wal. Theory of membrane capacitive deionization including the effect of the electrode pore space. *J Colloid Interface Sci*, 360(1):239–248, 2011. ISSN 1095-7103 (Electronic) 0021-9797 (Linking). doi: 10.1016/j.jcis.2011.04.049. URL https://www.ncbi.nlm.nih.gov/pubmed/21592485.

[96] W Tang, P Kovalsky, B Cao, and T D Waite. Investigation of fluoride removal from low-salinity groundwater by single-pass constant-voltage capacitive deionization. *Water Res*, 99:112–121, 2016. ISSN 1879-2448 (Electronic) 0043-1354 (Linking). doi: 10.1016/j.watres.2016.04.047. URL https://www.ncbi.nlm.nih.gov/pubmed/27151285.

[97] P M Biesheuvel, H V M Hamelers, and M E Suss. Theory of Water Desalination by Porous Electrodes with Immobile Chemical Charge. *Colloids and Interface Science Communications*, 9:1–5, 2015. ISSN 22150382. doi: 10.1016/j.colcom.2015.12.001.

[98] X Gao, S Porada, A Omosebi, K L Liu, P M Biesheuvel, and J Landon. Complementary surface charge for enhanced capacitive deionization. *Water Res*, 92:275–282, 2016. ISSN 1879-2448 (Electronic) 0043-1354 (Linking). doi: 10.1016/j.watres.2016.01.048. URL https://www.ncbi.nlm.nih.gov/pubmed/26878361.

[99] John Newman and William Tiedemann. Desalting by Means of Porous Carbon Electrodes. *AIChE Journal*, (21):25–41, 1975.

[100] F Foerster. The electrolysis of hypochlorite solutions. *Trans. Am. Electrochem. Soc*, 46:23–50, 1924.

[101] Ali Hemmatifar, Michael Stadermann, and Juan G Santiago. Two-Dimensional Porous Electrode Model for Capacitive Deionization. *under review*, 2015.

[102] S O Kucheyev, A V Hamza, J H Satcher Jr, and M A Worsley. Depth-sensing indentation of low-density brittle nanoporous solids. *Acta Materialia*, 57(12):3472–3480, 2009. ISSN 13596454. doi: 10.1016/j.actamat.2009.04.003.

[103] S O Kucheyev, M Stadermann, S J Shin, J H Satcher Jr., S A Gammon, S A Letts, T van Buuren, and A V Hamza. Super-compressibility of ultralow-density nanoporous silica. *Adv Mater*, 24(6):776–780, 2012. ISSN 1521-4095 (Electronic) 0935-9648 (Linking). doi: 10.1002/adma.201103561. URL http://www.ncbi.nlm.nih.gov/pubmed/22228389.